Unconventional Tuning Parameters of Low Temperature Transport at Strontium Titanate Interfaces

Zur Erlangung des akademischen Grades eines

DOKTORS DER NATURWISSENSCHAFTEN (Dr. rer. nat.)

von der KIT-Fakultät für Physik des
Karlsruher Instituts für Technologie (KIT)

genehmigte

DISSERTATION

von

M. Sc. Daniel Arnold

Tag der mündlichen Prüfung: 22.01.2021

Referent: Prof. Dr. M. Le Tacon
Korreferent: Priv.-Doz. Dr. R. Eder

Contents

Chapter 1

Introduction

Many experiments in physics are realized by controlling the properties of a system. In order to extend the view on the underlying physical mechanisms responsible for the resulting behavior of a system, experimentalists often manipulate external parameters. With various external tuning parameters like pressure, temperature or magnetic field many materials can be tuned to different phases and the underlying mechanisms can be probed by crossing phase transitions. These traditional tuning parameters are in many cases insufficient to fully uncover the true nature of apparent physical phenomena. Many researchers are looking for new tuning parameters to manipulate a system which yields further insights and give valuable information not accessible by other means.

One system studied for several decades is strontium titanate ($SrTiO_3$). Despite its rather simple perovskite structure, it shows a huge variety of different physical phenomena induced by all kinds of control parameter like – to mention a few – temperature, magnetic and electrical field, pressure, doping, ion bombardment, strain and light. $SrTiO_3$ can be doped to superconductivity, is close to ferro-electricity and structural instabilities. It has been used to generate heterostructures with a variety of epitaxial materials extending the play ground for functionality.

In this thesis $SrTiO_3$-based two-dimensional interfaces are investigated via electrical transport measurements at low temperatures. Hereby two unconventional control parameters will be the main subject: On the one hand illumination at low temperatures and on the other hand the vicinal substrate tilt.

To literally enlighten the relevant mechanism dominating electrical transport in this temperature regime, exposure of samples to light at temperatures below 1 K is introduced. Persistent photo-conductance was found almost seven years ago in $SrTiO_3$. To avoid this effect at low temperature measurements, experimentalists normally keep their samples in the dark at least 24 hours prior to cool-down. In this thesis we choose another approach and make use of the persistent photo-conductance by illuminating the samples at low temperatures. It enables to tune the sheet resistance – not only by using temperature or applied magnetic field, but also in a persistent manner – with increasing irradiation dose. Additionally it is shown

here that illumination also leads to alterations of different transport characteristics at various $SrTiO_3$-based interfaces.

Furthermore, vicinal substrate tilts are used to control the resulting step terrace structure and thus to influence anisotropic resistance properties. $SrTiO_3$ is often used as a substrate for a large number of materials building different types of heterostructures. Superconductivity was found at the interface of $LaAlO_3/SrTiO_3$ and more recently at the boundary between $Al_2O_3/SrTiO_3$, which in this thesis will be used to study the influence of the terrace width on the transport properties. By a slight misalignment of the substrate surface with respect to the crystallographic axis, a vicinal substrate with step terraces is produced. Varying the tilt γ lead to a different density and height of the resulting terraces. Ideally at large γ filamentary transport can be studied when the terrace width gets comparable or even smaller than characteristic length scales of transport.

To investigate the proposed tuning parameters, in this thesis a $LaAlO_3/SrTiO_3$ sample and three different specimen of $Al_2O_3/SrTiO_3$ with various γ are characterized. Electrical transport measurements are carried out at temperatures between $12\,mK \leq T \leq 12\,K$ and in magnetic fields B up to $14\,T$. We discuss the sheet resistance as function of temperature $R_\square(T)$, the longitudinal resistance $R_{xx}(T, B)$ and transversal resistance $R_{xy}(T, B)$[1] probed with B and the I/U characteristics for different temperatures.

Following this first remarks a short introduction on $SrTiO_3$-based interfaces is given in Chapter 2. An overview of existing tuning parameters will be presented as well as a summary of the relevant concepts. Finally the sample preparation, the experimental setup and the measurement methods are explained.

Chapter 3 presents a new route to manipulate the electrical transport characteristics of the $LaAlO_3/SrTiO_3$ interface with light at low temperature. A light emitting diode, which can be operated at dilution fridge temperatures, will be characterized and used to manipulate sheet resistance, the superconducting transition temperature and the structural fingerprint of inhomogeneities visible in I/U characteristics.

In Chapter 4 the influence of vicinal substrate tilt γ on the transport of $Al_2O_3/SrTiO_3$ interfaces and simultaneously the influence of light is investigated. We focus on the superconducting transport properties altered with varying γ. An analysis will be given with respect to various current directions compared to alignment of the resulting terraces.

Chapter 5 finally contains a short summary of the results together with a conclusion.

---

[1]to extract the Hall coefficient

Chapter 2

Background

SrTiO$_3$ (STO) is one candidate to replace silicon in future semi-conducting technologies (The News Staff 2007). For instance Woltmann *et al.* 2015 shows promising results for the fabrication of field-effect transistors in a mass production fashion with electron-beam lithography. This thesis is concerned with the underlying physics in this system and this chapter will focus on fundamental research on STO and STO-based heterostructures. Many reviews on this subject can be found in the literature (Zubko *et al.* 2011; Sulpizio *et al.* 2014; Gariglio *et al.* 2018).

2.1 SrTiO$_3$-based interfaces

A frequently used substrate for thin film growth is SrTiO$_3$, a perovskite material of cubic symmetry at room temperature. In the center of an oxygen octahedra a titanium ion is located and strontium ions are arranged at the corners of the cubic cell. Many physical properties can be understood best if STO is consider as a stack of alternating SrO and TiO$_2$ layers. STO is a band insulator with an indirect band gap of around 3.2 eV (Weakliem *et al.* 1975). It undergoes an anti-ferrodistortive (AFD) transition to a tetragonal phase at $T_{\mathrm{AFD}} = 105$ K as a result of a tiny rotation of the oxygen octahedra (Hayward *et al.* 1999). This rearrangement leads to twinning and the formation of domain boundaries, which are attracting oxygen vacancies and play an import role in the doping mechanism (Yazdi-Rizi *et al.* 2016). In the same way dislocations of STO are important, where vacancies tend to cluster as a result of the enhanced mobility along lattice defects (Szot *et al.* 2002; Menzel *et al.* 2011). STO is a so-called quantum-paraelectric (Müller *et al.* 1979), meaning that ϵ strongly increases from room temperature down to low temperatures before saturating, for STO at around 4 K. Instabilities and a quantum critical point are some key words here, which are discussed in greater detail in the literature (see Zubko *et al.* 2011 and references therein). In the vicinity of this critical behavior superconductivity arises. In this respect STO shares similarities to high-T_c superconductors, although the superconducting transition temperature T_c is much lower.

Schooley *et al.* 1964 showed that STO as a bare material gets superconducting upon doping. Tuned by carrier density, STO shows a superconducting dome at low temperatures with a maximal T_c of 350 mK at rather low carrier densities $n \approx 4.5 \cdot 10^{18}$ cm^{-3} (Collignon *et al.* 2019). T_c goes down on increasing *and* decreasing doping and is in the low density regime the most diluted superconductor known so far (Lin *et al.* 2013; Gastiasoro *et al.* 2020). A seminal publication by Ohtomo *et al.* 2004 reports the discovery of another remarkable feature: at the interface of the two band gap insulators LaAlO$_3$ (LAO) with a band gap of 5.6 eV (Lim *et al.* 2002) and STO a high mobility electron gas forms with carrier mobilities exceeding $\mu = 10000$ cm^{2}V^{-1}s^{-1}. The authors proofed that the charge carrier density is located in the vicinity of the interface and can be viewed as two-dimensional (2D) in nature. In this thesis, it will be referred to as a two-dimensional electron system (2DES). As sketched in Figure 2.1, the similar lattice constants of LAO and STO, 3.791 Å (Geller *et al.* 1956) and 3.905 Å (Bednorz *et al.* 1977) respectively, allows an epitaxial growth of a LAO layer on top of TiO$_2$-terminated STO in the [001]-direction.
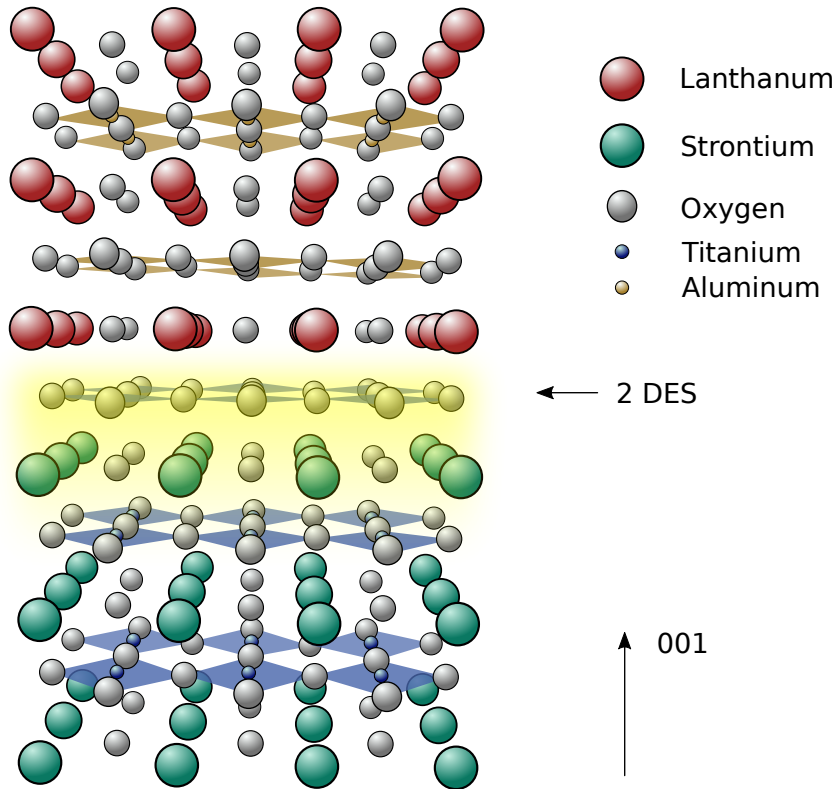

Figure 2.1: Interface between the TiO$_2$-terminated SrTiO$_3$ substrate and an epitaxial layer of LaAlO$_3$ in [001]-direction. At the top TiO$_2$ layer (blue) a two-dimensional electron system evolves indicated in yellow.

The work of Ohtomo *et al.* 2004 motivated many investigations and led to the discovery of superconductivity at this interface by Reyren *et al.* 2007. Caviglia *et al.* 2008 also discovered that the transport properties can be tuned via an external electric field using a back gate shown in Fig. 2.2. The superconducting transition parametrized in Fig. 2.2 by the Berezinskiĭ–Kosterlitz–Thouless transition temperature T_{BKT} ($T_{\mathrm{BKT}} \lesssim T_c$; blue circles) as well as the sheet resistance at $T = 400\,\mathrm{mK}$ (R_{sheet}, red symbols) can be manipulated by applying a gate voltage V_G. A dome-shaped behavior of the superconducting phase (blue area) as function of V_G is visible, while R_{sheet} is monotonically decreasing with increasing V_G. The quantum critical point (QCP) mark the quantum phase transition from insulator to superconductor showing that the ground state at low temperatures depends on the carrier concentration. The fact that the transition obeys the characteristics of BKT is evidence of the 2D nature of superconductivity. The right, over-doped side of the dome-like structure in Fig. 2.2 must viewed with caution. Gariglio *et al.* 2016 showed that in this regime the superconducting thickness is considerably enhanced with a further increase of the gate voltage, leading to an overall reduction of the 3D charge carrier concentration. Thus, what appears to be over-doping is actually associated with a reduction in charge carrier concentration.
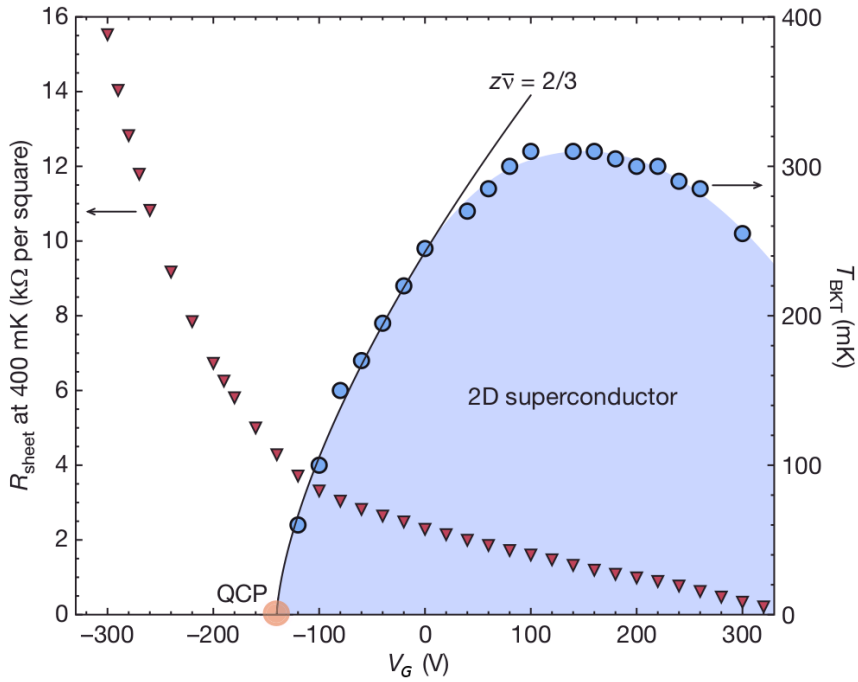
Figure 2.2: Field-effect tuning of the sheet resistance R_{sheet} at $T = 400\,\mathrm{mK}$ (red symbols) and T_{BKT} (blue symbols) using a gate voltage V_G. Blue area marks the dome-shaped behavior of the superconducting phase with a quantum critical point (QCP) on the low doping side. Figure adapted from Caviglia *et al.* 2008.

By analysis of the anisotropy of the in-plane and out-of-plane critical magnetic fields, it was possible to determine the thickness of superconductivity, which is indeed of 2D nature as already stated in Fig. 2.2. The thickness of superconducting layer is about 10 nm, while the superconducting coherence length ξ is of the order of $\xi \approx 70$ nm (Reyren *et al.* 2009).

The question where the charge carriers that populate the interface originate, is much debated and no consensus is found yet. Three different ways of charge transfer to the interface are discussed now:

i) One proposed mechanism derives from the polar discontinuity at the interface and the avoidance of the so-called polar catastrophe. The alternating SrO and TiO$_2$ layers of STO are charge neutral. The epitaxial grown LaAlO$_3$ consists of a stack of (LaO)$^+$ and (AlO$_2$)$^-$ layers charged with alternating polarity. Without further measures this would lead to a divergence of the electric potential. The divergence however is easily avoided by an electronic reconstruction in which half an electron per unit cell is transfered from the surface layer of LAO to the interface. The reconstruction is energetically favorable as soon as the LAO stack is thicker than at least 4 unit cells. Reinle-Schmitt *et al.* 2012 presented a comprehensive study on this effect, where they used a doped layer with only half the electric potential build-up and therefore needed exactly a twice as thick layer to get a conductive interface. The polar catastrophe model is strict concerning the amount of charge carriers which has to be transfered to the surface. On the other hand, Hall measurements do not see the expected value of carrier density (Trier *et al.* 2017). Furthermore in non-polar [110] direction conductivity was also found by Herranz *et al.* 2012. An comprehensive discussion concerning different experiments on this idea is published by Salluzzo 2015.

ii) More conventional charge carrier generation result from chemical doping. Firstly intermixing of Lanthanum and Strontium can occur at the interface, which is fabricated at elevated temperatures. This mechanism is studied by Qiao *et al.* 2011.

iii) Last but not least, oxygen vacancies in the perovskite structure might act as charge donors. This third mechanism is well known to be the main source of conductivity in high quality bulk STO. Kalabukhov *et al.* 2007 presented the doping via oxygen vacancies using different oxygen pressure conditions during the deposition of LAO on top of STO substrates. Tuning of the LAO/STO interface with oxygen deficiency was monitored with angle-resolved photoemission spectroscopy (ARPES) by Strocov *et al.* 2019. They also discussed the results in a framework of a composition of three-dimensional puddles embedded in an insulating phase.

Obviously various doping mechanisms might work in parallel and must be considered during experiments. Metal oxides with a perovskite structure are a versatile starting point for a variety of physical phenomenons (see Zubko *et al.* 2011). In the case of STO as substrate, the epitaxial grow of different materials on top lead to conductive systems (Seo *et al.* 2007;

Wang *et al.* 2012). In this thesis, we investigate the aforementioned LAO/STO interfaces, as well as the Al_2O_3/$SrTiO_3$ interface (AO/STO). AO/STO is shown to be superconductive at temperatures around 300 mK (Fuchs *et al.* 2014). The γ-spinel/perovskite interface is in contrast to LAO/STO non-polar and therefore the polar catastrophe model is not applicable for this interface (Chen *et al.* 2013). Since the AO/STO heterostructure can be grown at room temperature, it is not vulnerable for undesired effects like material intermixing, because of an increased temperature during epitaxial growth (for LAO we need a heated substrate of a few hundreds degrees Celsius). Infrared ellipsometry studies revealed a stronger carrier confinement as a result of a reduced depth profile of the charge carriers in comparison to LAO/STO (Yazdi-Rizi *et al.* 2016).

2.2 Electronic transport at STO-based interfaces

In this section an introduction to electronic transport properties of STO-based interfaces and to the corresponding physical concepts is given. We will mainly discuss the physical phenomena in this system using simple assumptions.

The band structure of bulk STO is well studied by experimental methods (*e.g.* ARPES) and verified by band structure calculations, *e.g.* Kahn *et al.* 1964; Piskunov *et al.* 2004. Bands close to the Fermi edge which have to be considered for transport properties derive mainly from Ti $3d$ orbitals. In a cubic crystal field, the Ti $3d$ orbitals degeneracy is lifted and split into a triplet of t_{2g} orbitals (d_{xy}, d_{xz} and d_{yz}) and a doublet of e_g orbitals (d_{z^2} and $d_{x^2-y^2}$). The lowest unoccupied band possess mostly t_{2g} character and properties of electron doped STO has been successfully modeled by tight-binding methods taking into account titanium orbitals only, *e.g.* Stengel 2011. Zhong *et al.* 2013 extended the tight-binding model successfully to the description of LAO/STO interface in accord to experimental data recorded via ARPES (Walker *et al.* 2015). Modeling of transport data of 2DES in (110) STO heterostructures were carried out in Wolff 2018. The tight-binding band structure was used to calculate the in-plane anisotropic magneto-resistance in the framework of a relaxation time approximation.

2.2.1 Brief introduction to magneto-transport phenomena

Field-effect experiments with control of the charge carrier density n are able to shift the Fermi level using a gate voltage V_G, *e. g* (Joshua *et al.* 2012). A part of the associated magneto-transport measurements are presented in Fig. 2.3, where the Hall resistance R_{xy} for different V_G is plotted as function of applied magnetic field B. At the low side of a critical density $n < n_c$, the Hall resistance R_{xy} show a linear dependency with respect to magnetic field, which is expected for a simple one-band model with a parabolic band. A linear dependence of R_{xy} as seen in Fig. 2.3 b), directly relates the Hall constant R_H to the

carrier density n by the relation

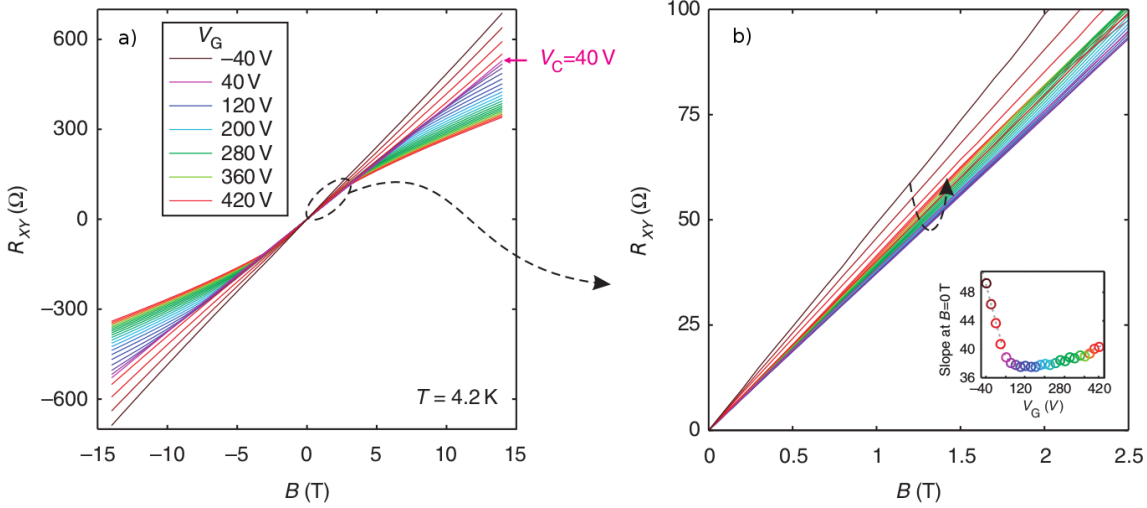$$\frac{R_{xy}}{B} \equiv R_H = \frac{1}{ne}.$$ (2.1)

Figure 2.3: Field-effect tuning of Hall resistance $R_{xy}(B)$ at $T = 4.2$ K for different gate voltages V_G. a) shows measurements up to $B = 15$ T where non-linearities are visible at higher magnetic fields when $V_G > V_c$. The linear behavior of R_{xy} up to $B = 2.5$ T is shown in b). The inset presents the slope of R_{xy} at zero magnetic field as function of V_G. Figure adapted from (Joshua *et al.* 2012)

Above a critical gate voltage V_c, R_{xy} display non-linearities (see Fig. 2.3 a)), which are interpreted as evidence for a Lifshitz transition, *i. e.* the population of an empty band upon pushing the carrier concentration n over a threshold n_c by the increasing gate voltage. Such a scenario is in line with simple considerations on the band structure derived from t_{2g} titanium orbitals which give the largest contribution to the lowest unoccupied band of bulk STO. Surface effects will lift the degeneracy of d_{xy}, d_{yz}, and d_{zx} symmetry and move d_{yz} and d_{zy} derived bands up in energy with respect to the band with mainly d_{xy} character. The Fermi energy reaches upon doping the bottom of the former band at the Lifshitz transition. Notably, the maximum of T_c as a function of charge carrier density, coincides with the thus defined critical n_c. Within this scenario the effective masses of quasi particles in the two bands vary naturally due to a significantly different dispersion at the Γ Point. It is thus reasonable to approximate magneto-transport using a two-band model with two types of charge carriers of different concentration and mobility. Such a model, celebrated in many textbooks (see *e. g.* Gross *et al.* 2014) for its simplicity and power to display many features of real systems, depends on a sufficient number of parameter, to fit non-linearities. One has to keep in mind, though, that it makes predictions on the transversal magneto-resistance $R_{xx}(B)$ at the same time. Not shown here, Joshua *et al.* 2012 presented a scaling of R_H and R_{xx} which shows that both quantities share a common field scale B_w.

The simple considerations of Joshua *et al.* 2012 are jeopardized by refined band structure calculation (*e. g.* Zhong *et al.* 2013) which display a much more complex band structure (and Fermi surface) and make the identification of exactly two quasi-free carrier types questionable.

Further lifting of degeneracies of the bands at the interface is caused by a Rashba-type of spin-orbit interaction. Magneto-resistance data in LAO/STO interfaces often show features which can be understood in the framework of localization. In particular Caviglia *et al.* 2010; Ben Shalom *et al.* 2010; Cheng *et al.* 2017 could tune the sign of the localization peak at small magnetic fields from positive to negative by using a gate voltage, shown exemplary in Fig. 2.4 a).
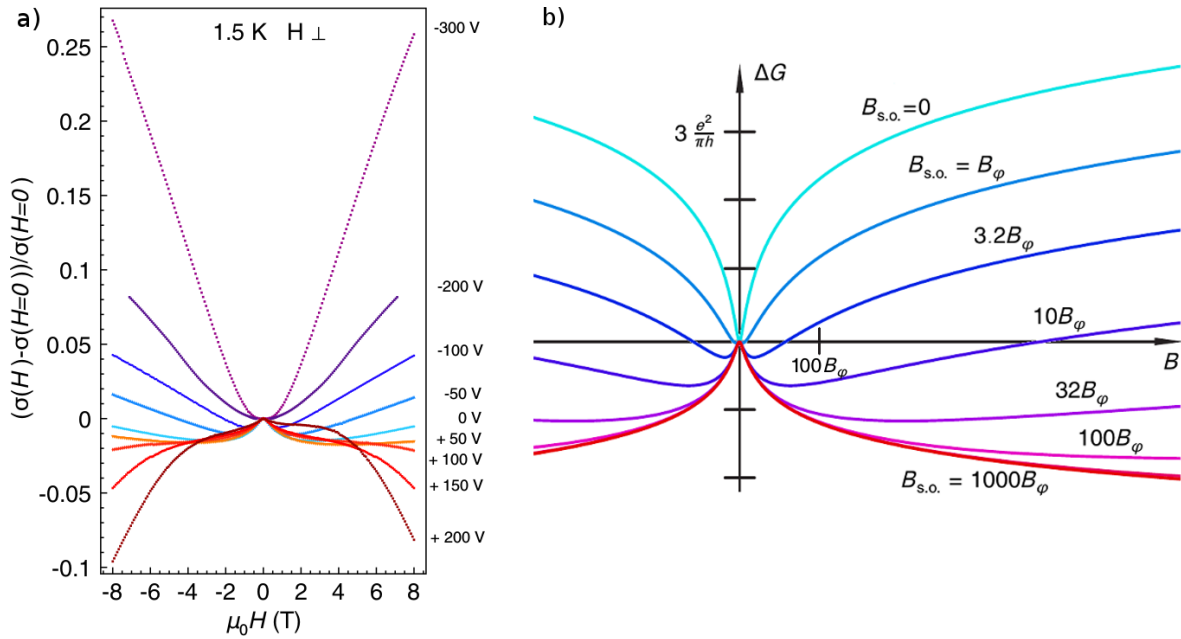

Figure 2.4: Magneto-conductance as function of applied magnetic field. a) A gate voltage V_G is used to go from of weak localization to weak anti-localization at low magnetic fields. Measurements taken at $T = 1.5\,\text{K}$ for different V_G indicated on right panel. b) Calculated change of magneto-conductance according to Eq 2.2 to 2.4 with $B_{s.f.} = 0$. a) is reproduced from Caviglia *et al.* 2010

Compared to the calculated values plotted in Fig. 2.4 b) a transition from weak to strong spin-orbit coupling leading to weak localization and weak anti-localization, respectively[1]. According to Bergmann 1984 and discussed in Schäfer 1993 the correction of the sheet

---

[1]A similar behavior has been demonstrated by Bergmann 1984 for thin films of magnesium covered with sub-monolayers of gold.

conductance $\delta G_\square$ can be described with the help of the Digamma function Ψ:

$$\begin{aligned}
\delta G_\square(B) &= \delta G_\square(B) - \delta G_\square(0) \\
&= \frac{3}{2} f(B, B_{tr}) - \frac{1}{2} f(B, B_{si})
\end{aligned} \tag{2.2}$$

where

$$f(B, B_x) = \frac{e^2}{\pi h} \left(\Psi \left(\frac{1}{2} + \frac{B_x}{B} \right) - \ln \left(\frac{B_x}{B} \right) \right) \tag{2.3}$$

and

$$\begin{aligned}
B_{tr} &= \frac{4}{3} B_{s.o.} + B_{s.f.} + B_\varphi \\
B_{si} &= 2 B_{s.f.} + B_\varphi
\end{aligned} \tag{2.4}$$

The magnetic fields B_x can be related to the respective scattering times τ_x with use of the diffusion constant D as $B_x \cdot D \tau_x = h/8\pi e$. If the spin-orbit scattering time $\tau_{s.o.}$ is significantly larger than the phase relaxation time τ_φ and the scattering at magnetic defects represented by $\tau_{s.f.}$ is neglected, Eq. 2.2 can be simplified to: $\delta G_\square = -0.5 \cdot f(B, B_\varphi)$. Since $\delta G_\square$ for the discussed case has an opposite sign as the case of neglectable SOC, the terminus weak anti-localization is appropriate.

2.2.2 Superconductivity and the Berezinskiĭ–Kosterlitz–Thouless transition

Superconductivity was found in a variety of STO-based interfaces (Reyren *et al.* 2007; Biscaras *et al.* 2010; Fuchs *et al.* 2014). An elementary introduction to relevant theories is found in numerous textbooks, *e.g.* Tinkham 2004. Only a limited numbers of parameters is important here, most notably the superconducting transition temperature T_c related to the energy gap by

$$\Delta = 1.764 \cdot k_B T_c, \tag{2.5}$$

according to Bardeen *et al.* 1957. The upper critical magnetic field B_{c2} above which superconductivity is completely suppressed, can be used to calculate the Ginzburg-Landau coherence length ξ:

$$B_{c2} = \frac{\Phi_0}{2\pi\xi^2}, \tag{2.6}$$

where the magnetic flux quantum $\Phi_0 = h/2e$.

Many publications use the critical field to estimate the thickness of the superconducting layer (Herranz *et al.* 2015; Kozuka *et al.* 2009; Reyren *et al.* 2009). Fig. 2.5 show the critical field extracted from sheet resistance measurements in dependence of magnetic field applied perpendicular (blue symbols) and parallel (red symbols) to the LAO/STO interface

for different temperatures. An anisotropic behavior of the critical field values for different directions of magnetic field is visible. Using the relation of critical field and coherence length evaluated in the Ginzburg-Landau theory, the thickness of superconducting layer can be estimated to about 10 nm, while the superconducting coherence length ξ is of the order of $\xi \approx 70$ nm in the directions parallel to the interface (Reyren *et al.* 2009).
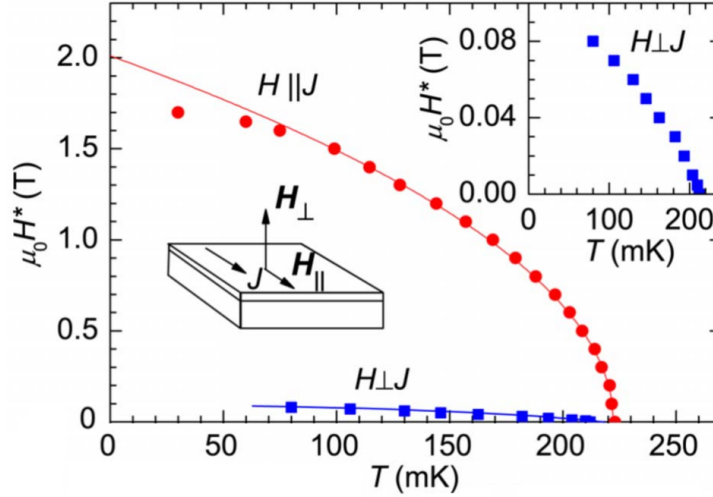

Figure 2.5: Critical magnetic field as function of temperature at the LAO/STO interface. The current is running along the interface like sketched in the Figure. Applied magnetic field parallel to the interface is indicated red. Measurements with magnetic field applied perpendicular are represented in blue symbols, where the inset shows the data on a smaller scale. Figure adapted from (Reyren *et al.* 2009)

The transition in 2D superconductors is governed by models first described by Berezinskiǐ 1970, (Berezinskiǐ 1972) and Kosterlitz *et al.* 1973. This so-called Berezinskiǐ–Kosterlitz–Thouless (BKT) transition is associated with a characteristic temperature scale $T_{\text{BKT}} < T_c$ at which vortex anti-vortex pairs tightly bound at low temperatures gets mobile and lead to a finite resistance. This is most clearly seen in I/U characteristics which display a power law behavior $V = I^3$ at T_{BKT}. The observation of such a power law at $T < T_c$ is usually seen as evidence for 2D superconductivity and does not occur in bulk superconductors.

2.3   Tuning parameters for the transport at the STO-based interfaces

There are many methods to manipulate the transport characteristics of STO-based interfaces. A comprehensive review article is available recently (Christensen *et al.* 2019).
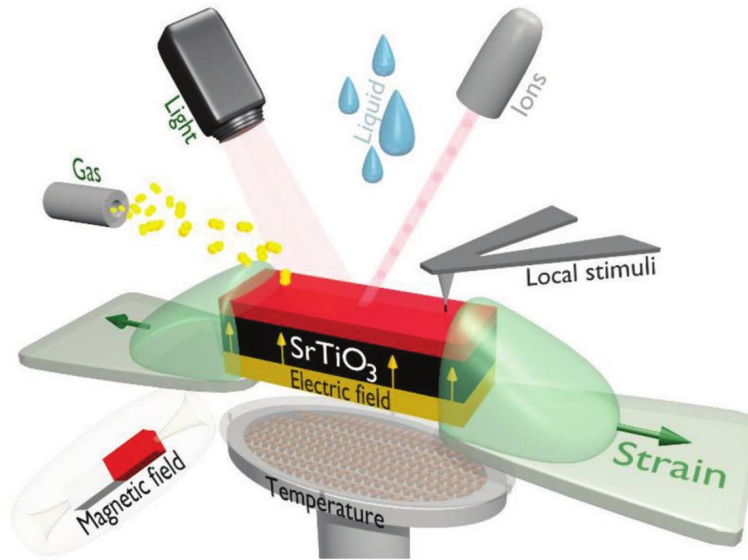

Figure 2.6: Various mechanism to manipulate the physical properties of STO-based interfaces. Figure reproduced from Christensen *et al.* 2019

Figure 2.6 shows an overview of external stimuli at STO-based interfaces. Besides many exotic tuning parameters like gas, liquid, ions, local stimuli via an AFM tip and strain, the use of a dielectric gate to manipulate the transport properties with an electric field. With the induced charge carriers like gate tuning in semiconductors, many researcher showed a dome like behavior of the superconducting state and also an insulator to metallic transition in the LAO/STO system.

2.3.1   Photo-induced changes in transport

Transport in STO is sensitive to photo induced charge carriers with a extremely long lifetime even at room temperature, discovered first by Tarun *et al.* 2013. Guduru *et al.* 2013 performed transport measurements under the influence of light at liquid helium temperatures $T = 4.2$ K. While no photo-induced changes of transport could be detected at bare STO, the LAO/STO interface resistance is decreased under the influence of light, see Fig. 2.7. With increasing photon energy, the change of resistance is increased. When the photon energy is exceeding the band gap of STO, a dramatic change in resistance was measured and after

illumination the resistive state is changed in a persistent manner. Taking into account Hall resistance data taken for different illumination state, the authors proposed the influence of a high-mobility band which can be excited as the photon energy exceeds the band gap of STO. By heating the sample to room temperature the pristine resistance value before illumination can be restored.
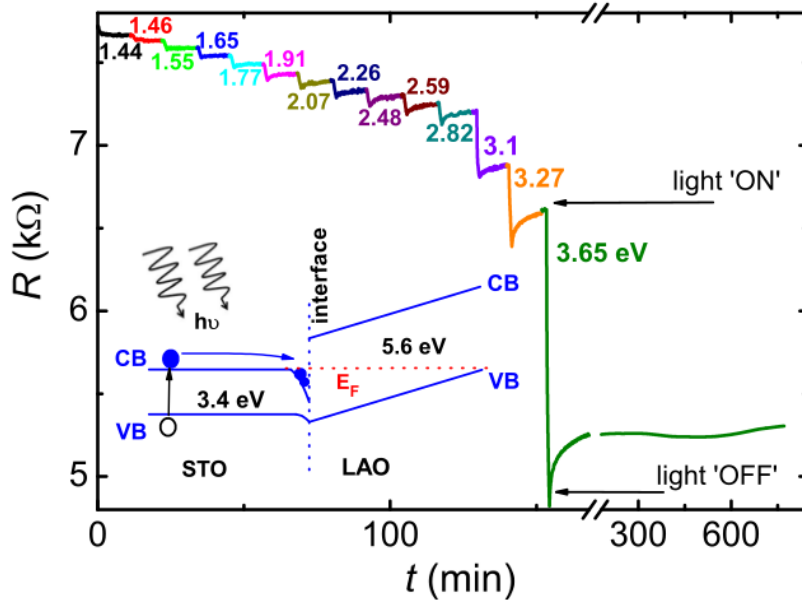

Figure 2.7: Resistance as function of time under the influence of light on LAO/STO at 4.2 K. Different photon energies are indicated with various colors. Exceeding the band gap of STO (indicated in the blue sketch), the resistance change is significantly increased (green curve). Figure adapted from Guduru *et al.* 2013

Yazdi-Rizi *et al.* 2017 performed a tuning of the electrical transport properties via influence of UV-light at low temperatures for bare STO as well as for LAO/STO shown in Fig. 2.8. After illumination a persistence resistance change was detected for STO. To reverse this effect, it was necessary to increases temperature above the AFD transition at $T_{AFD} = 105\,\text{K}$ (see Fig. 2.8 a). The effect was thus attributed to domain boundaries at which oxygen vacancies tend to cluster. This was further supported by the observation that a weak uniaxial strain at STO in [110] direction, which untwins the tetragonal phase, can suppress the persistent photo-conductance. Fig. 2.8 b) shows the measurements of the so-called Berreman mode measured with infrared ellipsometry at the LAO/STO interface. By analyzing this measurement the authors can estimate not only the charge carrier density, but also the thickness of the conducting layer, in this case at $T = 30\,\text{K}$. After illumination with UV-light the carrier density was doubled and the thickness was nearly unaffected within the measurement limits ($d_{\text{before UV}} = 12 \pm 2\,\text{nm}$ and $d_{\text{after UV}} = 13 \pm 2\,\text{nm}$).
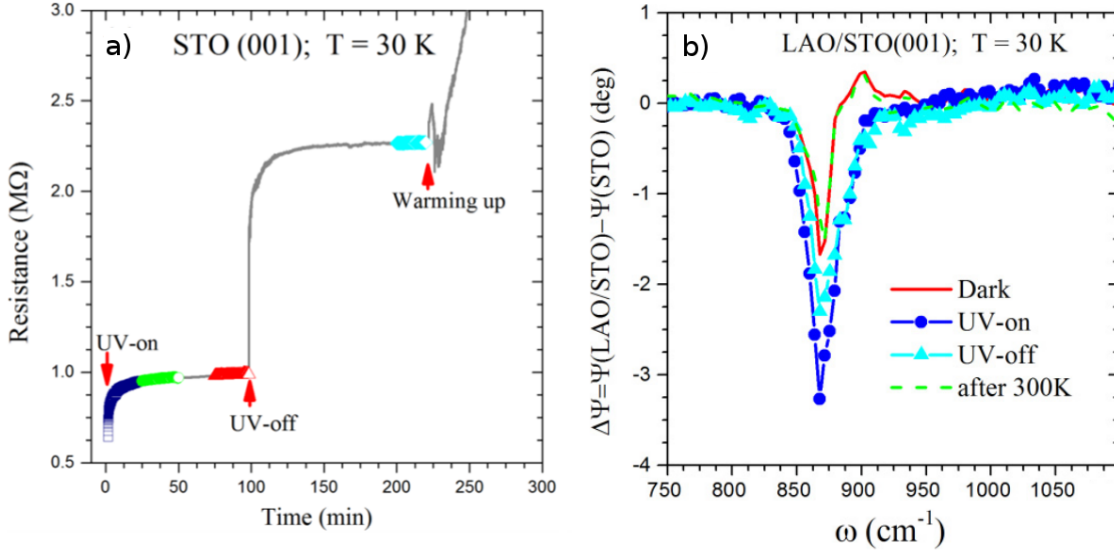
Figure 2.8: a) Resistance as function of time for STO. UV-light at $T = 30\,\mathrm{K}$ leads to conductivity, which is present even after illumination is turned of. The change in resistance can be reversed by thermal treatment above $T_{\mathrm{AFD}} = 105\,\mathrm{K}$. b) Representation of the Berreman mode measured with infrared ellipsometry at the LAO/STO (001) interface at $T = 30\,\mathrm{K}$. With UV-light the visible dip change, even after illumination. The effect again can be reversed by heating the interface to temperatures above $T_{\mathrm{AFD}} = 105\,\mathrm{K}$. Adapted from Yazdi-Rizi *et al.* 2017

The question addressed in this PhD work is whether illumination has an influence on the superconducting properties of the STO-based interfaces. Can light a low temperatures be used to replicate the dome-like structure of T_c while presumably keep the thickness of the conducting layer fixed?

2.3.2   Vicinal substrate tilt

Another possibility of manipulating the electrical transport characteristics is pursued here. On vicinal STO-substrates a terrace structure can be created on purpose and in principle makes the tuning of the step edge density possible. To get an atomically flat surface, the STO substrates are cut perpendicular to the [001] direction and polished. Next it is treated with a buffered ammonium fluoride solution selectively etching SrO to retrieve a TiO_2 terminated surface. Annealing leads to the desired result (Koster *et al.* 1998). Due to technical limitations the surface treatment is not ideal and step terraces with a width w of typically $w \approx 220\,\mathrm{nm}$ will be generated. This can be directly linked to a vicinal substrate tilt of $\gamma = 0.1\,°$ using

$$w = \frac{a}{\tan \gamma} \tag{2.7}$$

where $a = 3.905$ Å is the unit-cell height of STO.

Therefore it is not possible to create an atomically flat surface over long distances in the µm-range with commercial available substrates. However an increasing vicinal substrate tilt γ can be utilized to reduce the step terraces width in a controlled manner. Sketched in Figure 2.9 with reasonable high vicinal substrate tilt γ filamentary like terraces are theoretically possible, displaying a quasi one-dimensional (1D) system by comparing the width of the step terraces to the mean free path of charge carriers or in the case of superconducting structures to the Ginzburg-Landau coherence length ξ.
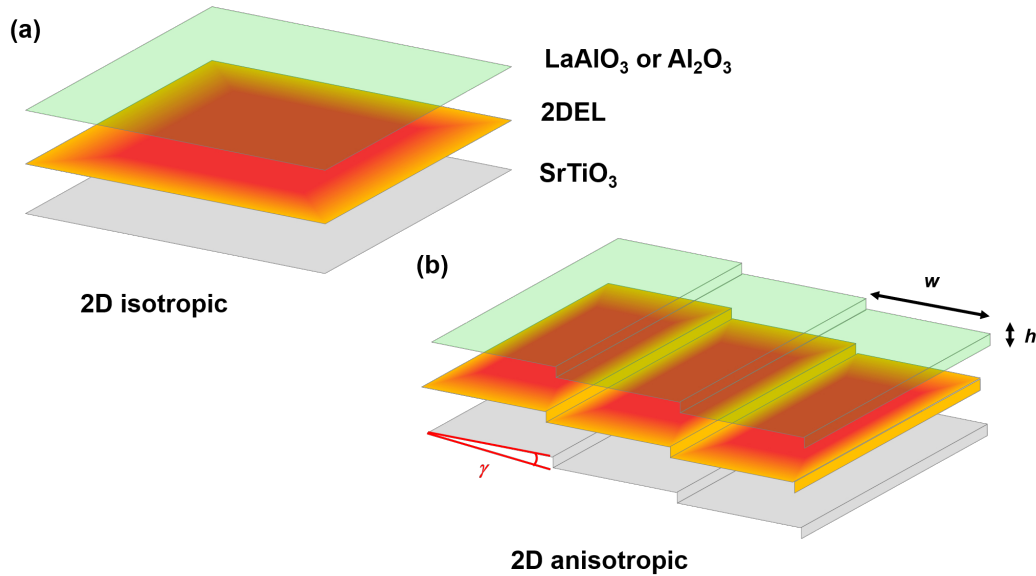

Figure 2.9: Schematic of the vicinal substrate tilt γ at $SrTiO_3$-interfaces. $SrTiO_3$ single crystals are used as substrates (grey) to be covered with either $LaAlO_3$ or Al_2O_3 (green), forming a conducting layer (orange). Isotropic interface without γ (a). A finite γ leads to step-terraces with a width w and a height h (b). Figure reproduced from (Wolff *et al.* 2020)

2.4 Measurement setup and methods

2.4.1 Sample preparation and contacting

The samples characterized in this thesis were prepared by Dr. Dirk Fuchs. SrTiO$_3$ single crystals ($5 \times 5 \times 1$ mm^3) provided by CrysTec GmbH Kristalltechnologie (Germany) were used as substrates, which have a electrochemically polished surface to start with. Following the recipe of Koster *et al.* 1998 leads to a high quality TiO$_2$ termination of the STO surface in [001] direction. With pulsed laser deposition a thin film of LaAlO$_3$ or Al$_2$O$_3$ was grown on top of STO. Details of the patterning of the microstructures by a hard-mask technique is described elsewhere (Fuchs *et al.* 2017; Wolff 2018). In essence, the TiO$_2$ terminated STO surface is covered by an amorphous CeO$_3$ inhibit layer. A photolitographic lift off process is used to prevent the layout of the final structure from being covered by the inhibiting agent. The active interface is created by pulsed laser ablation of either LaAlO$_3$ or Al$_2$O$_3$ in a low pressure (*e. g.* 10^{-4} Pa) oxygen atmosphere, which gets into direct contact with the STO in [001] direction at the designed layout only. In the case of Al$_2$O$_3$ this might lead to a slight oxygen deficiency in the top most layers of the STO surface, which in turn is responsible for the formation of a 2DES at the interface. Two different measurement layouts were used for various samples and will be presented with the transport characterization later on. The flame fusion (Verneuil method) grown STO single crystals are known for dislocation lines with preferred directions along $\langle 110 \rangle$ (Guguschev *et al.* 2014). For electrical currents applied perpendicular to the slip planes, this increases the charge carrier scattering (Wolff 2018).

To release charge carriers photo-induced during the mounting of the STO-based heterostructures, the samples are kept in the dark for at least 24 hours prior to cooldown. The specimen were fixated with GE Varnish on a sample holder and contacted via ultrasound bonding (HB05 manual wire bonder by TPT, Germany) using a 25 μm aluminum wire with 1% Si (Heraeus Holding GmbH, Germany) to copper pads of the sample holder shown in Figure 2.10. The sample holder was further thermally coupled with an electrically conductive adhesive Silberleitlack 200 (Demetron GmbH, Germany) on the thermal reservoir and connected to the cold finger of the mixing chamber of the dilution refrigerator. Finally the copper pads were electrically soldered to the wire loom of the dilution refrigerator setup.
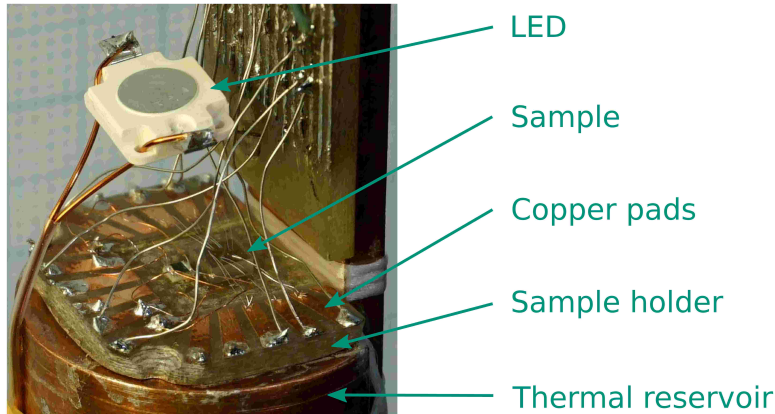
Figure 2.10: Picture of the light source above Hall bar structured LAO/STO sample mounted on a sample holder and coupled to the thermal reservoir for measurements at low temperatures.

2.4.2 Low temperature measurements and methods

To measure the transport properties of STO-based samples at low temperatures, a home-build setup in a Kelvinox MX250 (Oxford Instruments, UK) ^{3}He-^{4}He dilution refrigerator (DR) was used. To thermalize samples electrically connected to room temperature measurement units at the base temperature of the DR a careful filtering is required (Cui 2010). The DR is hence equipped with low temperature metal powder filters which are efficient up to ultra-high frequency noise at $f > 300$ MHz mainly due to the reducing skin depth. Additionally a resistor-capacitor circuit is used as a low pass filter with the cutoff frequency $f_{RC} = \frac{1}{2\pi RC}$. A resistor $R = 1$ kΩ and a capacitance $C = 150$ pF leads to 3 dB damping at 10 kHz covering the mid frequency range. Filtered in this way 15 lines of a wire loom lead from room temperature down to the sample stage, where 12 are carried out as twisted pair lines. Other lines of the 24 wire loom are reserved for thermometry purposes.

The sample stage represented in Figure 2.10 is located in the center of an superconducting magnet which is about 350 mm below the cold plate (of the dilution fridge). The supporting structure of the sample stage is made from sterling silver and has a moderate thermal resistance, so as to allow the sample temperature to be elevated with respect to the temperature of the mixing chamber. The sample temperature is regulated by a software controlled proportional-integral-derivative (PID) loop with the help of a ruthenium oxide resistor R_h, glued to the sample stage; the thermal resistance has been adjusted to give a temperature rise of the mixing chamber of about 100 mK for a sample temperature of 500 mK; any desired temperature between $T \approx 12$ mK to $T \approx 1$ K can be controlled. With the help of a Model

370 AC resistance bridge (Lake Shore Cryotronics, USA) the temperature is evaluated by the measurement of R_h, where with a calibration files the temperature of our sample stage can be extracted. The resistor is calibrated in the whole temperature range against a noise thermometer. The regime of elevated temperatures in the sense of low temperature measurements up to 12 K can be excessed if the ^{3}He-^{4}He mixture is removed, while keeping the temperature of the so-called 1K Pot regulated[2].

The magnetic field can be ramped between $B = -8\,$T to $B = +8\,$T quasi continuously with a step-width of the order of 0.1 mT using a superconducting magnet controlled by an IPS 120-10 Power Supply (Oxford Instruments, UK).

The low level signals on the measuring lines end in a shielded metal box at the head of the cryostat. Here amplification by differential amplifiers are performed before signals are distributed to the data acquisition system. The current bias is provided by a home-build voltage controlled current source driven by the data acquisition system. If required, a voltage divider is used to precondition the driver voltage. Amplification of potential differences from voltage terminals of the sample was done by instrumentation amplifiers INA 110 (Burr-Brown and Texas Instruments, USA) in a 500× mode. The field-effect transistor inputs of the INA 110 have exceptional low input bias currents and an adequate noise performance.

Wherever possible Lock-in technique is used to perform the measurements. The sheet resistance $R_\square(T)$, as well as for the magneto-conductance $R_{xx}(B)$ and $R_{xy}(B)$ are measured with a frequency of typically $f = 31.4\,$Hz, chosen in a window of minimal external interference. The bias current was chosen as small as possible to achieve the required signal to noise ratio and simultaneously to minimize self-heating.

I/U characteristics were recorded in four wire configuration. The current bias was ramped up to $I = \pm 10\,$µA and simultaneously the potential drop U over the voltage terminals of the sample were monitored. The current was ramped with a positive and negative slope in a typical measurement time of about 10 s up to roughly 2 min.

For measurements with temperatures up to room temperature and magnetic fields up to $B = 14\,$T the Physical Property Measurement System (PPMS) from Quantum Design (Quantum Design GmbH, Germany) was used. The software provided by the PPMS system directly control the temperature and the magnetic field. The actual measurements in lock-in technique were performed with the data acquisition system also used at the DR.

2.4.3   Improvements of measuring system

During the experiments presented in Ch. 3 only one lock-in channel was required at a time to record the material information. Between measurements of, *e. g.*, resistance as function of temperature and the Hall coefficient as a function of magnetic field the lock-in was physically switched to a different preamplifier output. For the samples investigated

---

[2]The 1K Pot is not allowed to heat up since it operates a charcoal trap collecting the exchange gas used in the cooldown process.

in Ch. 4 with up to 15 voltage terminals and at least 10 relevant potential differences (five times U_{xx} and U_{xy}, in the terminology of Ch. 3) this traditional setup would limit the amount of collectable data in a discomfortable way mainly due to time restrictions. Moreover, in search of correlations of events in different segments a simultaneous recording of potential differences is mandatory. Even during the experiments presented in Ch. 3 it proved tedious to measure magneto-resistance and Hall effect separately and a considerable time gain would have been achieved by the improved setup introduced in this section.

As exemplified in the previous subsection, the DR is equipped with 12 twisted pairs of well filtered electrical lines running all the way from room temperature to the mixing chamber. Some of them are required to perform thermometry, power the sample stage heater and provide grounding connections for sample stage and *RC* filters. The remaining lines are sufficient to provide current leads and connections to three Hall bar terminals. Utilizing this wiring setup access to three different Hall bar terminal in a single cooling cycle of the dilution stage.

The aim of an upgrade of the room temperature electronics was thus to make the simultaneous recording of six pairs of differential voltage terminals possible. First, the number of home-build differential amplifiers (see subsection before) used to precondition the voltage drops has been increased to six. The output of these amplifiers and the voltage-controlled current source are connected to a new data acquisition system consisting of three PCI Express cards purchased from Spectrum Instrumentation GmbH (Germany) in two separate PCs. The first PC contains a 4-channel digitizer with a sample rate of 130 MS/s (M4i.4411-x4) and a arbitrary wave generator (AWG) generating up to 625 M samples per second on four channels (M4i.6622-x8). The second PC is equipped with a 8-channel digitizer sampling at 5 MS/s (M2p.5913-x4). All cards have a genuine 16 Bit resolution. Further resolution can be gained by a sensible software strategy taking advantage of the excessively large sampling speed as compared to the band width limitations of the experimental setup[3]. This is demonstrated here for the generation of a sinusoidal current. Resistance coefficients are measured with a lock-in technique, which was implemented in software on the PCs handeling the data stream from the digitizer cards as described below. This method requires an AC current source with a minimal level of distortion. The current source used in the experiments is made up of a carefully designed bipolar voltage-controlled current source installed in a shielded box at the head of the cryostat. The current source is controlled by the AWG at a sampling speed between 60 MHz and 600 MHz. A suitable waveform resembling a single period of a sinusoidal signal is generated by software and transferred to the internal memory of the AWG card. The card is run in a repetitive mode generating a continuous stream of

---

[3]Experiments in a DR require careful filtering and only a small bandwith of electrical signals is allowed to enter the mixing chamber. For high frequency experiments it is required to center the bandwith around the frequency of interest. The current investigations are concerned with effect at DC and a finite frequency is essentially only used to stay above the 1/f-noise knee in the operational amplifiers utilized for the purpose of signal conditioning. Filtering is hence always realized by RC low pass elements which limit the genuine bandwidth to around 10 kHz.

output values. The frequency is adjusted to desired values by setting the sampling speed[4]. The goal is to generate a signal as close as possible to a sinusoidal signal after passing a RC-filter with cutoff frequency $f_{RC} = 10\,\text{kHz}$.
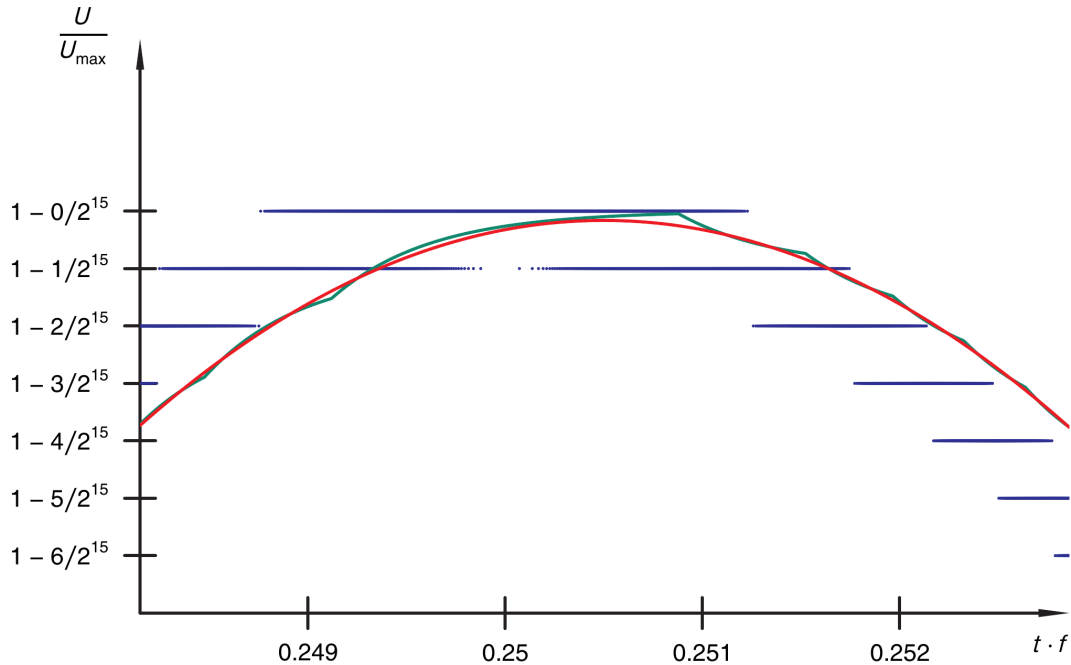

Figure 2.11: Schematical diagram of signal generation. Blue dots represent the output sample of the AWG card, while the red line results from RC bandwidth filtering. The green line demonstrate the improvement of the more sophisticated approach used in the new setup as compared to a deficient strategy (see text).

Rounding $U_{\text{nom}} = A \cdot sin(\omega t)$ directly to the nearest 16-bit quantization level of the AWG is a deficient strategy which leads to annoying artefacts after bandwidth filtering (green line in Fig. 2.11). A superior strategy is exemplified in Fig. 2.11 in which a small portion of the output samples around the maximum of the sine wave (blue dots) is compared to the bandwidth limited signal (red line) after filtering. The blue output levels are calculated with a simple recursive algorithm. For each sample U_{nom} is calculated and added to a summing register $U_{\text{sum}} \leftarrow U_{\text{sum}} + U_{\text{nom}}$. A second register ΣU_{act} holds the sum of all past output levels. The output level of the current sample is than adjusted to the quantized level U_{act} which is as close as possible to the difference $U_{\text{sum}} - \Sigma U_{\text{act}}$. In the last step of the recursive procedure the summing register of actual values is updated: $\Sigma U_{\text{act}} \leftarrow \Sigma U_{\text{act}} + U_{\text{act}}$. This simple algorithm leads to a quickly alternating output encircling the desired value U_{nom}, which—for constant U_{nom}—equals the time average of the actual output. The red line in Fig. 2.11 is the result of an RC-filter. Besides an unimportant shift in phase it approaches the intended sine wave

---

[4]Typically a frequency of $f = 31.4\,\text{Hz}$ is used and the memory of the AWG card is filled with an array of 2M samples. In this case the AWG card has to sample at 62.8M values each second.

with high fidelity. The procedure explained here leads to an improvement amounting to about additional 8 Bit of resolution.

The two digitizer cards of the data acquisition system are synchronized to the AWG card by a phase locked loop using the AWG clock signal. The handling of the data stream from this cards is quite demanding even for state of the art personal computers. Actually, the stream of 520M 16 Bit integers per second collected by the 4-channel digitizer cannot be transferred by the data bus in real time. For very fast measurements the values can be stored in the internal memory of the digitizer card and analyzed at a later time. For the purpose of this work, however, a continuous measurement is essential. To facilitate the data transfer to internal memory the number of digitized samples is reduced by a field programmable gate array (FPGA) directly on the digitizer card. The FPGA takes a box car average usually over 256 consecutive 16 Bit samples. This is demonstrated here for the generation of a sinusoidal current. The resulting amount of 24 Bit integers can safely be streamed over the data bus into PC memory as can be the 40M sample, 16 Bit stream of the 8-channel card. Once the stream arrives in PC memory, it is analyzed by application dependent software usually resulting in a further reduction of data. The simplest algorithm implemented for collecting I/U characteristics applies a digital RC-filter with user selectable time constant T_{RC}, which should not be inferior to the reciprocal bandwidth of the electrical wiring. It is sufficient to store a few data samples during a time span of T_{RC} without loss of information. The filtering process leads to considerable gain of resolution, which is not limited to the 16 Bit of the digitizer cards, and a tremendous reduction of data.

A more sophisticated acquisition mode provides a software implemented lock-in method. The AWG card provides a trigger signal upon start of the repetitive sinusoidal wave form which is used as phase detection by the software lock-ins. Since the sampling rates of all cards of the acquisition system are phase locked, a single trigger signal at start up is sufficient. The data stream of up to 8 channels cannot be handled by a single CPU mainly due to the complexity of the floating point arithmetic needed in the present digital data processing. Hence, each channel is handed over to a separate thread running on different CPUs of an multi-core processor. Besides the phase sensitive detection of the AC response an time averaged representation of input channels $\overline{U}$ is calculated as well (which is needed by the lock-in math anyway). The time constants for calculating $\overline{U}$ can be set independently of the lock-in time constant. $\overline{U}$ can actually be used as a high resolution DC recorder if the AC component of the excitation current is set to zero. The lock-in software running on separate computers for each digitizer card provides a data interface which keeps a programmable amount of past data with time stamps in volatile memory. For each cycle of the sinusoidal excitation a limitable number of data points is handled this way. The final data acquisition software is organized as a separate application which communicates with the lock-in interface via POSIX network sockets. Thus, it is possible to collect the data of the total of twelve lock-in channels provided by the two digitizer cards in a single application in a perfectly synchronized fashion.

2.4.4   Data processing after measurements

The analysis of collected data depends on the specific type of measurement. The filter characteristics of the measurement lines leads to a small phase shift of the pre-amplified voltage response which was visible as a small signal in the quadrature channel of the lock-in during measurements of $R_\square(T)$. This signal was minimized by adjusting a temperature independent phase. The amplifier offset was detected as a small voltage present at low temperatures in the superconducting state and was subtracted. Finally a shift $R_\square(T)$ along temperature axis was applied to handle the temperature drag of 0.5 mK caused by the time constant of filters in thermometry. This shift is not noticeable when $R_\square(T)$ is plotted directly in the temperature range 20 mK $< T < 1$ K but leads to a shift in d$R_\square$/dT peaks at the superconducting transition temperature. The lock-in time constant was chosen to be 1 s and a moving average filter was applied whenever appropriate.

Magneto-transport measurements ($R_{xx}(B)$ and $R_{xy}(B)$) were analyzed similarly. Magnetic fields in the range of $B \pm 8$ T were applied in [001] direction of the sample in the DR. The remanent field of the superconducting magnet (approximately 3 mT) was adjusted by shifting the minimum in $R_{xx}(B)$ to zero. Due to a small misalignment of the Hall voltage terminals a contribution of the longitudinal magneto-resistance is present in U_{xy} and was treated by anti-symmetrization. U_{xx} is symmetric with respect to magnetic field and has been symmetrized merely as simple procedure to reduce noise.

$$R_{\text{sym,asym}} = (R(B) \pm R(-B))/2 \tag{2.8}$$

I/U characteristic have been measured in different ways. In some cases the required resolution was achieved by a slow measurement and noise reduction by RC-filtering. A considerable improvement could be achieved by averaging 20 repetitive measurements. This was only possible with the improved data acquisition system described before. To investigate the step features in the I/U characteristics, the derivative is used to locate resistive jumps. In order to reduce the noise and simultaneously be sensitive to abrupt changes, a convolution with the derivative of a Gaussian filter is used (*GNU Scientific Library*[5]) utilizing the property of a convolution

$$\frac{\mathrm{d}}{\mathrm{d}t}(G * x) = \frac{\mathrm{d}G}{\mathrm{d}t} * x. \tag{2.9}$$

The resistive jumps were detected by looking for positions, where the derivative exceeds a threshold of $4\times$ the root mean square of noise floor.

---

[5]https://www.gnu.org/software/gsl/doc/html/filter.html

Chapter 3

Light as Tuning Knob of the LAO/STO Interface

This chapter is primarily based on results published in Arnold *et al.* 2019 with an additional view on the magneto-transport and I/U characterization. A new route to tune the transport characteristics of the LAO/STO interface making use of photo-conductance is presented. While the sensitivity of transport properties to illumination is well known in principle, it has so far been more regarded as a nuicance which yields to unstable behavior changing over time on extremely long scales. However, here it will be shown, that photo-conductance can be well controlled and persistent tuning of properties can be established by illumination the interface at very low temperature. To this end a light source working at temperatures below $T = 4.2\,\mathrm{K}$ is essential. A careful characterization in a so-called physical property measuring system (PPMS) by Quantum Design reveals that a specific type of light emitting diode (LED) can be utilized for this purpose. Such an LED is installed in the dilution refrigerator (DR) and operated successfully at base temperature. First, I will describe the characterization of the LED before data collected on the LAO/STO system in the DR and the PPMS are presented.

3.1 Low temperature light source

For all irradiation experiments presented in this thesis the same LED, a so-called "Golden Dragon Plus" (type LW W5AM from Osram Licht AG, Germany) has been used. The active layer of this LED emits a narrow line of blue light which is converted by a phosphor layer (Ce^{3+} doped $Y_3Al_5O_{12}$) to a broad spectrum appearing white to the human eye. Figure 3.1 shows the spectrum emitted by the LED at room temperature and displays the narrow primary emission line centered at 460 nm and the broad photoluminescence peak around 565 nm.
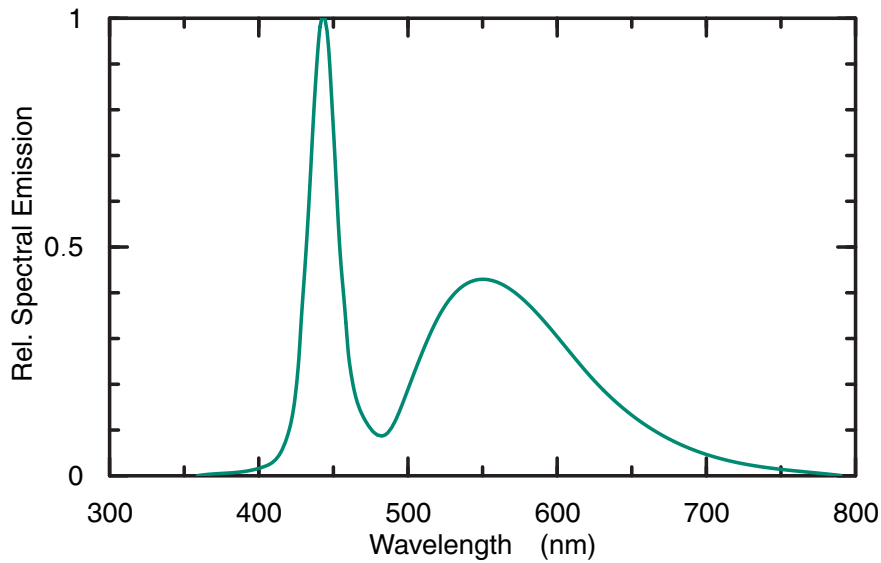
Figure 3.1: Spectrum of a LED (type LW W5AM, "Golden Dragon Plus", Osram Licht AG, Germany) at room temperature as function of wavelength. The spectrum comprises a narrow primary emission peak at 460 nm and a broad photoluminescence peak with a maximum at 565 nm. Adapted from *Golden DRAGON Plus* 2015.

The recommended operating temperature of this LED is in the range $-40\,°C < T < 125\,°C$ (*Golden DRAGON Plus* 2015). In search of a light source able to illuminate the sample below the boiling point of Helium, different LEDs have been tested at cryogenic temperatures. Typically, monochromatic LEDs tend to exhibit a pronounced blue shift with decreasing temperatures and in most cases stop visible light production well above $T > 77\,K$. This fact is reflected in the I/U characteristics by a diverging voltage drop on cool down for a given constant current. However, in rare cases light is emitted even at cryogenic temperatures. Most notably, the LW 5WAM displays a rather moderate shift in its voltage onset (see Fig. 3.2). Even at $T = 77\,K$, as checked visually in an open dewar while immersed in liquid nitrogen, the LED was perceived as a white light source and no change in color temperature could be observed when compared to the room temperature emission. The diode characteristics shown in Fig. 3.2 shifts to higher voltages with decreasing temperature, though. Nevertheless, as a proper I/U characteristic curve is observed even at $T = 4.2\,K$, the LED emits light obviously down to very low temperature. The "Golden Dragon Plus" is according to OSRAM a small size high brightness light source and is in typical applications driven at currents well above $I_{\text{LED}} > 100\,mA$. The limited cooling power of a DR does not permit such high currents. During the illumination experiments in the DR the diode current has to be limited and was chosen in the range $10\,nA < I_{\text{LED}} < 50\,µA$.

The LED is thus operated in a temperature and current regime far outside of the range recommended by the manufacturer and it is not clear at all how efficient electrical energy is converted to radiant energy under this circumstances. Here, a bolometric experiment is described, which directly observes the radiant energy of the LED at temperatures down to $T = 2\,\text{K}$. By using absorbers of two different colors it is established, that photons of various energies in the visible range are emitted. The maximal photon energy, however, cannot be larger than e times the voltage drop across the diode and is thus well below the band gap of bulk STO.
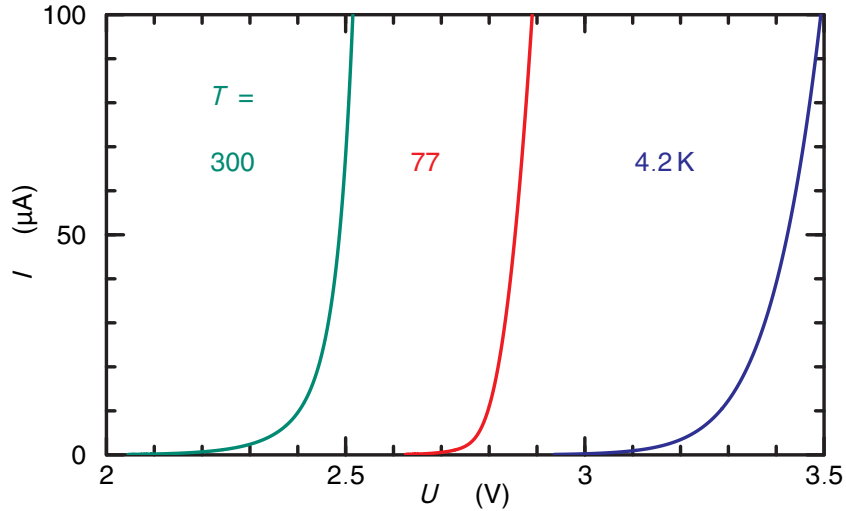

Figure 3.2: I/U characteristic curves with a maximum current of $100\,\mu\text{A}$ of the LED at three different temperatures: room temperature (300 K) in green, boiling temperature of liquid nitrogen (77 K) in red and liquid helium (4.2 K) in blue.

The bolometric experiment is performed in a PPMS. It is used to control the temperature of a general purpose puck shown in Fig. 3.3 onto which the LED is thoroughly thermally anchored. A calibrated Cernox thermometer R_{CX} (Lake Shore Cryotronics, CX-1050-SD-1.4L) is mounted with the help of two thin Nylon fibers (80 μm diameter) at a distance of 10 mm above the diode and illuminated by the LED when the diode current I_{LED} is finite. The electrical connection of R_{CX} is established by two manganin wires with a length of 150 μm (30 μm diameter) and total resistance R_L. The resistance $R_{CX} + R_L$ is determined by a lock-in amplifier which measures the voltage drop across the thermometer arrangement in response to an AC current I_{CX}. This gives the thermometers temperature T_s after subtracting the (slightly temperature dependent) lead resistance R_L which in turn is determined on an additional manganin wire of identical length mounted separately.
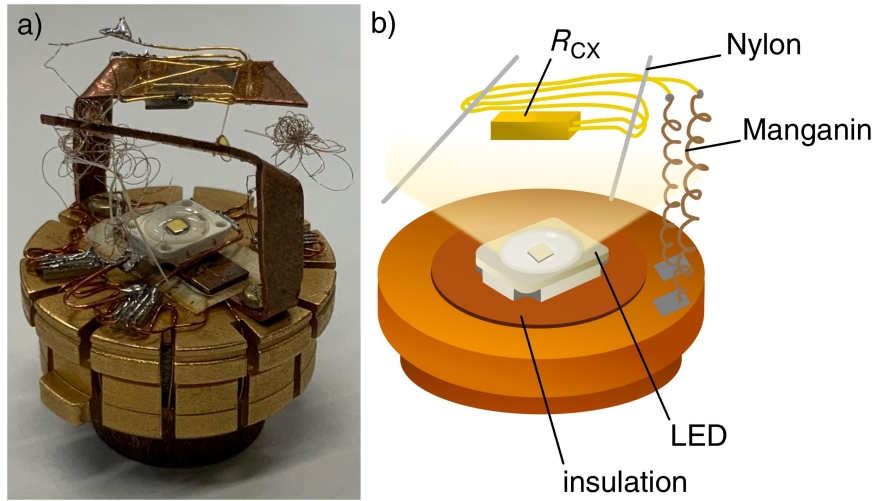
Figure 3.3: Bolometer to characterize the efficiency of the LED at low temperatures. Experiment is build on a general purpose plug for a PPMS. a) shows a picture of the setup and b) a simple sketch with only necessary parts. The LED is thermally anchored at the general purpose plug of a PPMS system. The cernox thermometer is connected via two manganin wires and centered in distance of 10 mm over the LED with two Nylon fibers.

The temperature T_s is monitored as a function of the current through the LED I_{LED} and the thermometer chip I_{CX}. Increasing either currents leads to a rise in T_s due to the intentional low thermal coupling of R_{CX} to the PPMS puck. A steady state T_s is approached after a rather long time constant of about 30 min. While the rise of T_s as response to I_{CX} is due to self heating, the temperature response to I_{LED} is completely caused by the absorption of photons emitted by the LED. Relating currents I_{CX} and I_{LED} which yields light power possible which in turn gives a lower bound to the efficiency of energy conversion by the LED. The smallest LED current at which an increase in T_s could be measured is $I_{\text{LED}} = 100\,\text{nA}$. The forward voltage $U_{\text{LED}}(100\,\text{nA}) = 2.95\,\text{V}$ at $T = 4.2\,\text{K}$ is used to estimate the photon energy of the primary emission line at low temperatures as $E_{\text{prim}} = eU_{\text{LED}}$ (corresponding to a wavelength of $\lambda = hc/(2.95\,\text{eV}) = 420\,\text{nm}$). Under idealized conditions every electron traversing the active layer of the LED is converted to a photon and so the radiant energy—ignoring down conversion by the phosphor—is limited to $P_{\text{LED}} = I_{\text{LED}} \cdot 2.95\,\text{V}$. Figure 3.4 a) shows the relation between T_s and P_{LED} for two different measurements. The first measurement indicated by the black color displays the temperature rise of the thermometer when coated by a black paint consisting of carbon black mixed with varnish (GE 7031). In a second run (gold color) only the short wavelength of the main emission line was absorbed by the thermometer. The black paint was removed, uncovering the bare gold plated thermometer chip absorbing now predominantly at wavelengths below 500 nm (Loebich 1972) and reflecting photons of lower energy. The reduced absorption results in a lower temperature rise. Fig. 3.4 a) includes also the effect of self-heating as a function of P_{CX} (green data). As illustrated for $P_{\text{LED}} = 100\,\mu\text{W}$ by the arrows in Fig. 3.4 a) P_{CX}, which is a measure for the irradiance flux

absorbed by the thermometer, is determined as a function of P_{LED}. Finally, a geometry factor relates the absorbed power P_{CX} on the small thermometer chip and the exposed leads to the total radiant flux P_{rad} emitted by the LED in the solid angle of illumination. P_{rad} is plotted versus P_{LED} in Fig. 3.4 b). The fraction of radiant flux dissipated from the black absorber is shown in black, the gold data represent the gold plated absorber. The theoretical limit it represented as red dashed line. Uncertainties in the deduction of the geometry factor f limits the accuracy of this result by roughly 20 %. The LED has a remarkable high efficiency at 4.2 K with a total radiant intensity of about 500 nW/(μAsr) · I_{LED} in forward direction. For the short wavelength part of the LED spectrum consisting mainly of the primary emission line, the radiant intensity is given by 300 nW/(μAsr) · I_{LED}, as deduced from the absorption by the gold plated thermometer.
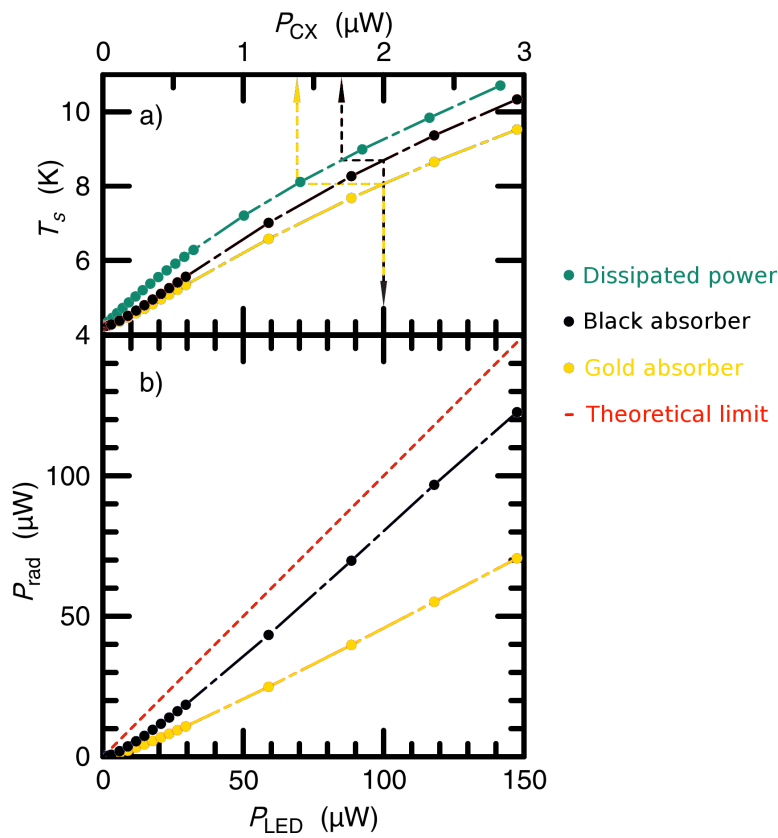

Figure 3.4: a) Temperature rise of cernox thermometer T_s in dependency of $P_{\text{LED}} = I_{\text{LED}} \cdot 2.95 \, \text{V}$ (black and gold, lower scale) or power dissipated by the thermometer P_{CX} (green, upper scale). Black color represents the black, gold color the gold plated absorber, and green corresponds to the temperature rise caused by self-heating. b) P_{rad} as function of P_{LED}, red dashed line represents theoretical limit, black and gold symbols mark the black and gold absorber, respectively. Lines are guide to the eyes.

3.2 Influence of light on the superconducting transition temperature

To monitor the influence of light on the superconducting transition temperature, the LED is mounted about 10 mm above the LAO/STO sample in our dilution fridge as sketched in 3.5 (a photograph of the actual setup is shown in Fig. 2.10). The sample has a Hall bar geometry with two current leads and four voltage terminals to measure the longitudinal R_{xx} and the transversal resistance R_{xy}. The wire between the voltage terminals was designed to have a width of 20 μm and a length of 200 μm, but inspection of the micro structured sample under an optical microscope revealed an actual width of 17 μm and a width to length ratio of about 1 : 12.
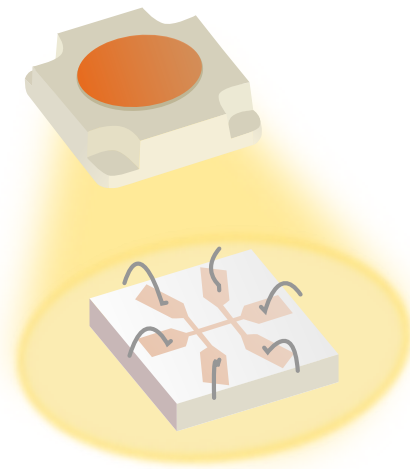

Figure 3.5: Simple sketch of light source above Hall bar structured LAO/STO sample at low temperatures. The LED is mounted at a distance of roughly 10 mm above the sample (see Fig. 2.10 for a photographic image).

For resistance measurements a home-build voltage controlled current source driven by an arbitrary wave function generator (Model AM300, Rhode & Schwarz GmbH & Co. KG, Germany) applies an AC current. The resulting voltage drop (referred to as U_{xx} and U_{xy} below) between applicable terminals is conditioned by an appropriate pre-amplifier (see 2.4.2 for details) and then recorded by a lock-in amplifier (Model 7265 DSP, AMETEK scientific instruments, USA). At very low temperatures the current has to be limited to $I_{AC} = 2$ nA to ensure operation in the linear regime of the I/U characteristics. For measurements at $T = 500$ mK where non-linearities in the I/U characteristics are effectively suppressed, the current burden can be safely increased to $I_{ac} = 9$ nA for the sake of higher resolution. Taking into account the width to length ratio of the Hall bar structure, the sheet resistance is given by $R_\square = U_{xx}/(12I_{AC})$.

The LED is electrically connected by superconducting leads to a source/measure unit (Keithley 2400, Tektronix Inc., USA) which is configured to source currents I_{LED} between $I_{min} = 100\,$nA and $I_{max} = 50\,\mu$A and to measure the resulting voltage drop.

As described in 2.4.2 the temperature of the sample can be regulated by a PID controlled resistor chip R_h. The considerable power dissipation of the LED at finite I_{LED} yields to a thermal burden as well and in principle I_{LED} can also be used as the temperature control parameter by the PID loop. The goal of the experiment described in this section is, however, to study the influence of illumination at *constant* temperature. The idea pursued here is to study the influence of photo-conductance—which will turn out to be persistent at low temperatures—on the superconducting transition of STO based 2DESs at $T_c \approx 150\ldots300\,$mK. Of course, photoconductance can be monitored at $T > T_c$ only [1]. The experiment described now has thus been conducted at $T_s = 500\,$mK as the set point of the PID control which was started while the LED was turned off ($I_{LED} = 0$). I_{LED} could then be increased slowly (on a rate of $\mathrm{d}I/\mathrm{d}t = 5\,\mu$A/min), while the PID control took care of a constant sample temperature within a margin of $\pm5\,$mK by reducing the heater current I_h sourced to R_h. Actually, I_h is completely turned off at $I_{LED} = 50\,\mu$A by the PID control at which point the heating is entirely established by the LED. Thus illumination at $T = 500\,$mK is limited to the intensity of the LED at $I_{LED} = 50\,\mu$A.
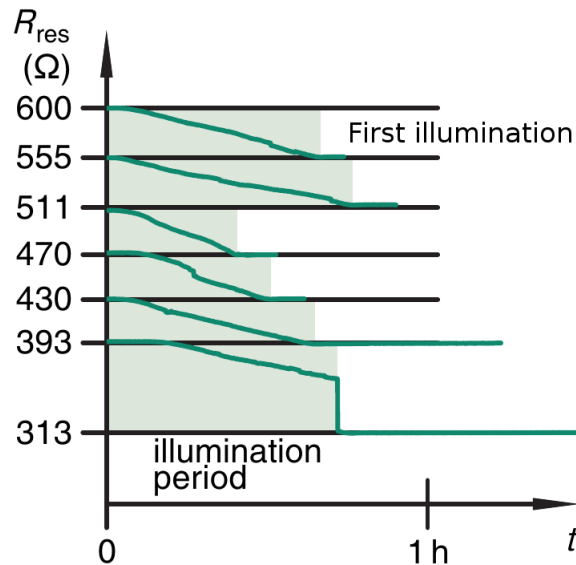

Figure 3.6: Change of residual sheet resistance R_{res} as function of time t for six illumination steps. First illumination step indicated. The time periods during which the LED is turned on, are indicated by a green shading.

Figure 3.6 demonstrates the effect of illuminating a LAO/STO interface at $T = 500\,$mK.

---

[1]The effect of light has been studied in zero magnetic field only. Suppression of superconductivity with a magnetic field while illuminating the sample, is the subject of an investigation planed for the future

The pristine sample happens to have a residual sheet resistance of $R_{\text{res}} \equiv R_\square(500\,\text{mK}) = 600\,\Omega$. During the time periods marked by the green shaded areas in the figure, the LED is turned on. As described above, the PID controlled temperature of the sample stage is held constant within a margin of $\pm 5\,\text{mK}$. This does not necessarily mean that the interface itself is kept at a constant temperature; an excess heating and a temperature gradient between the conductive interface and the temperature reservoir of the stage due to the absorbed radiant flux cannot be excluded a priori. However, an increase of the interface temperature would result in an increase of resistance since the temperature coefficient of the 2DES is positive (see *e. g.* Fig. 3.8). The observation, on the contrary, points in the opposite direction: As long as the interface is illuminated, its resistance continuously decreases. At any time in this process the LED can be turned off and the result is a state of constant residual resistance as indicated by the horizontal green lines outside of the shaded regions in Fig. 3.6. During the partial experiment[2] summarized in this figure, the LED is turned off six times, at which point extended experiments at residual resistances indicated by the values at the R_{res} scale has been performed. These experiments are presented in the following sections of this chapter. Some of them where recorded over time periods of several days and include I/U characterizations up to elevated current levels. The resistance has been measured in all of the resistance states as a function of temperature (*i. e.* in the range $12\,\text{mK} < T < 500\,\text{mK}$; the behavior at higher temperature is discussed further below) and as a function of magnetic field. None of these measurements do alter the state of the sample in any way. Only by turning on the LED again it was possible to alter the state and further reduce R_{res} which is thus under full control by the experimentalist. This is one of the major findings presented in this thesis. The tunability presented here for the LAO/STO interface is demonstrated for the 2DES between STO and aluminum oxide (see Ch. 4) as well and is presumably a general feature of STO based 2DES.

As a slight drawback visible in Fig. 3.6 most clearly for the illumination period between $R_{\text{res}} = 393\,\Omega$ and $R_{\text{res}} = 313\,\Omega$, resistance reduction is not always smooth. Sudden resistive jumps downwards can occur under the influence of illumination. The pronounced jump to $R_{\text{res}} = 313\,\Omega$ in Fig. 3.6 is actually the largest sudden decrease in resistance we have recorded so far. The limited band width of the electrical setup does not allow to study the dynamics of such a process which appears to be instantaneous to the lock-in amplifier. A possible origin of the jumps will be discussed further in Sec. 3.3 where an analysis of I/U characteristics indicate that rearrangements of inhomogeneities on a mesoscopic scale take place during the light-induced resistance changes.

By illumination, the resistance of the LAO/STO interface has been adjusted to twelve different states ranging from $R_{\text{res}} = 600\,\Omega$ down by a factor of 5 to $R_{\text{res}} = 120\,\Omega$. Figure 3.7 presents the residual resistance R_{res} as a function of the illumination dose (red dots). The dose has been calculated from the integral current $\int I \mathrm{d}t$ with the aid of the LED calibration presented in Sec. 3.1.

---

[2]The resistance has been further reduced by additional illumination. The minimal resistance which could be achieved is $R_{\text{res}} \approx 120\,\Omega$
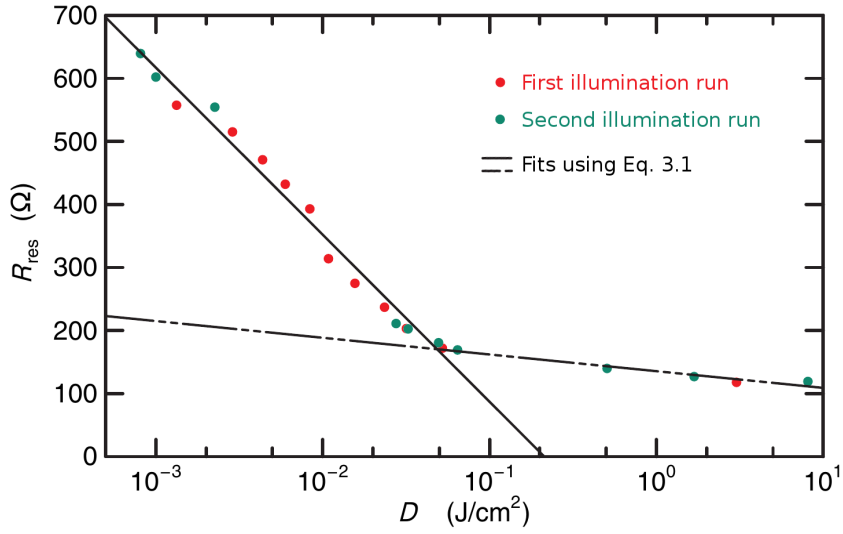
Figure 3.7: R_{res} as function of D. First illumination run indicated red, second run represented in green. Fit of different illumination areas in black solid and dashed line using equation 3.1. Parameters in text.

The tunability presented so far would be incomplete without the possibility of *increasing* the residual resistance and reverting the effect of illumination. This goal is achieved by elevating the temperature of the sample stage to $T > 1$ K which leads to a slow recovery of resistance lost during illumination. The process is quite smooth as well and in principle it should be possible to tune the resistance upwards to any desired value by a well controlled temperature profile in which a maximal temperature is held for a given time before the sample is cooled down again to $T \leq 500$ mK. However, it is considerable more demanding to reach a predefined R_{res} due to the temperature dependence of $R_\square(T)$ and the fact that the change of state is not conducted at the temperature $T = 500$ mK used to define R_{res}. The *rate* of resistance change clearly depends on the temperature to which the sample stage is heated up. At constant $T > 1$ K the rate of resistance change slowly goes down and the resistance tends to saturate at logarithmic time scales. The change can be stopped at any time by rapidly cooling down the sample into the temperature regime $T < 1$ K, where the resistance state is stable. The dilution fridge used for the low temperature experiments described here is not especially well suited for temperature profiles in the range above $T > 1$ K. For a full recovery of the resistance at which the experiment was started before the first illumination step ($R_{res} = 600 \, \Omega$) the sample was kept for several days at the maximal temperature at which the dilution unit can be operated without removal from the liquid helium dewar ($T \approx 12$ K). By doing so, a residual resistance of about $R_{res} \approx 675 \, \Omega$ could be reached, which is even slightly higher than the resistance of the pristine sample. With a reversal of photo-induced changes at temperatures way below the AFD transition temperature $T_{AFD} = 105$ K, the changes reported by Yazdi-Rizi *et al.* 2017 are in a different temperature regime, where the resistance recovery to the original state required heating above T_{AFD}.

To compare states reached by going down in resistance due to illumination with states of similar resistance (see Sec. 3.4) reached by an elevation of temperature several states were approached by controlled heating from below. An example is shown in Figure 3.8. Before heating the sample is in a state with $R_{res} = 136\,\Omega$ (see black symbols in the inset of Fig. 3.8). Upon heating to about $T \sim 1.7\,K$ a clear upturn in resistance can be noted. The heater R_h was turned off as soon as $T = 1.8\,K$ has been reached and the resistance measured on rapid cooling down is displayed by green symbols. In this case a rather moderate change of the residual change by less than $1.4\,\%$ is achieved. Following the temperature down to $20\,mK$ reveals a distinctive shift in the superconducting transition to higher temperatures.
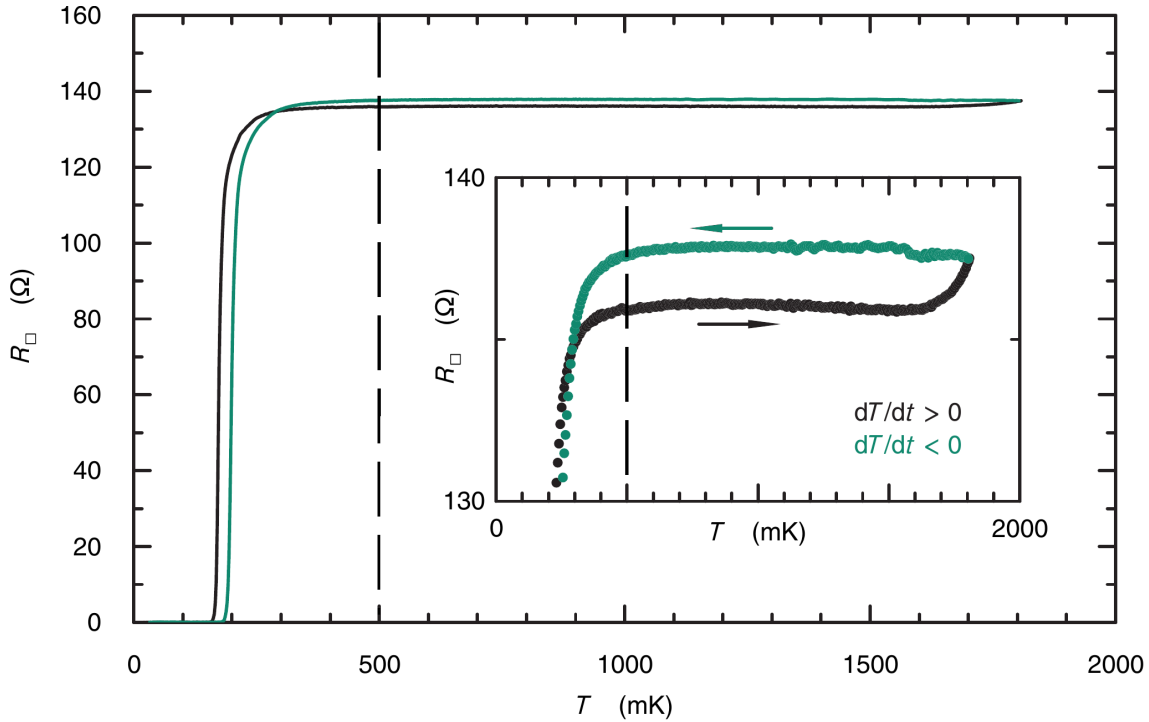

Figure 3.8: Sheet resistance $R_\square$ as function of temperature T during a recovery step at elevated temperatures up to $1.8\,K$. Black dots represents the resistive state after illumination before resistance recovery, the green dots marked the partly recovered resistive state after reaching elevated temperatures. The black dashed line indicate the maximum temperature of the typical transport characterizations. The inset shows a detailed view of the sheet resistance recovery between $1.6\,K$ an $1.8\,K$.

Figure 3.7 includes as green symbols the result of further light induced state changes which are recorded after full recovery of the resistance by heat treating the interface. A comparison between red symbols (reducing the resistance of the pristine sample) and green symbols (reducing the resistance of a heat treated sample) demonstrates the reproducibility of the light-induced state change. The residual resistance R_{res} by which the interface is characterized is uniquely set by the illumination dose D.

The figure displays $R_{res}(D)$ as a function of dose D on a logarithmic scale and indicates two different regimes marked by the two black lines which represent the phenomenological law

$$R_{res}(D) = R_{ini} - \Delta R \cdot L_D, \quad L_D \equiv 10 \log_{10}\left(\frac{D}{1(\text{mJ cm}^{-2})}\right) \text{ dB}. \quad (3.1)$$

depending on two parameters, namely the initial resistance value R_{ini} and exposure sensitivity ΔR. The least square parameter in the two regimes are given by $R_{ini} = 617\,\Omega$, $\Delta R = 26.5\,\Omega$ and $R_{ini} = 215\,\Omega$, $\Delta R = 2.65\,\Omega$, respectively.
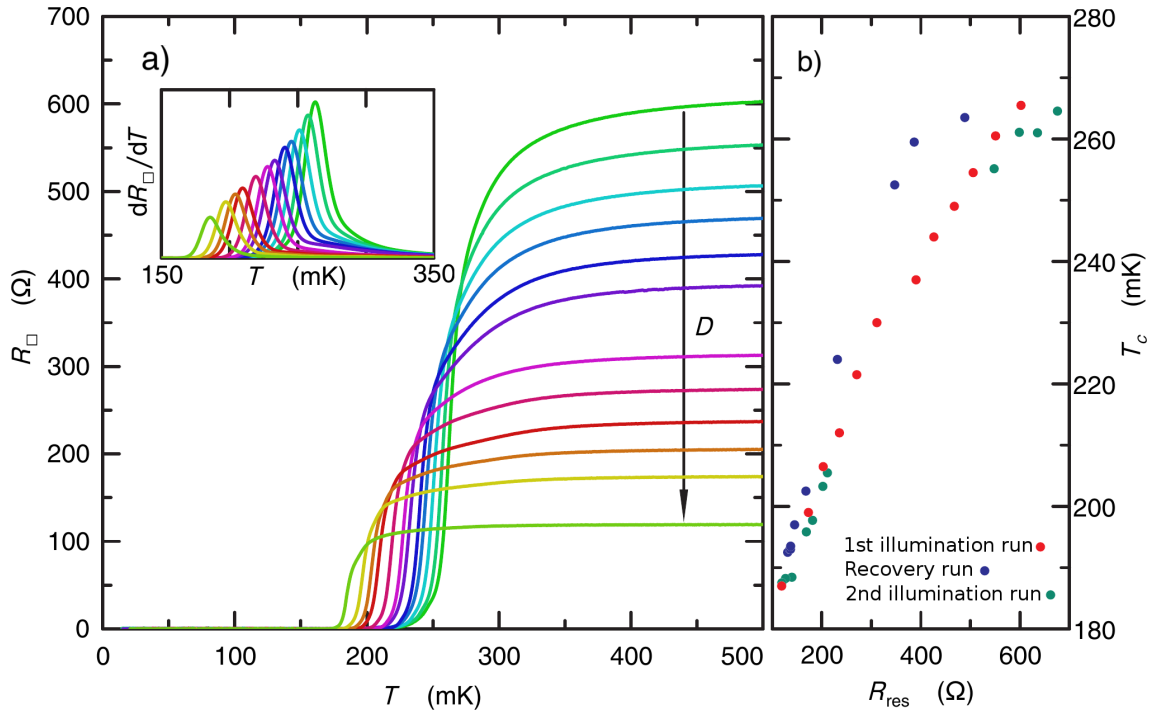

Figure 3.9: a) $R_\square$ vs. T. Curves are recorded in different states induced by increasing illumination dose D. The shown states correspond to the red symbols in Fig. 3.7. b) The superconducting transition temperature T_c (defined as the temperature at which $R_\square(T_c) = 0.5 \cdot R_{res}$) as a function of $R_{res} \equiv R_\square(T = 500\,\text{mK})$. The red symbols correspond to the states presented in a), blue symbols are extracted from states approached during resistance recovery by heat treatment, and green symbols result from the second illumination run (see green symbols in Fig. 3.7).

Figure 3.9 gives an overview of the effect an illumination has on the superconducting transition. Each curve shown in the left panel represents the continuous output of the lock-in amplifier, appropriately scaled and slightly filtered, while the temperature was swept from $T = 500\,\text{mK}$ down to $T \ll 100\,\text{mK}$ within two hours. Thereafter the temperature was ramped back in two hours to $T = 500\,\text{mK}$ and within the resolution of Fig. 3.9 a) as defined by the line width of the curves no difference between $dT/dt < 0$ and $dT/dt > 0$ can be no-

ticed. Only a detailed look at the steepest portion of the curves (not shown) reveals a slight shift in temperature which can be completely attributed to a temperature drag of the thermometry. Different colors in Fig. 3.9 a) correspond to different resistance states approached by increasing illumination dose D. Clearly perceptible is the larger gap between curve six and seven where the capital D has been placed. It is caused by the largest jump visible in Fig. 3.6 which led to a larger change in R_{res} than intended.

In Fig. 3.9 b) the transition temperature, here deduced in the most elementary way by the defining equation

$$R_{\square}(T_c) = 0.5 \cdot R_{\text{res}}, \tag{3.2}$$

as a function of R_{res} is shown. The color of the symbols identify three separate series of resistance states approached in successive order. The first series (represented by the red symbols) is constituted by the twelve states reported in part a) of the figure. The first state of this series is that of the as cooled down pristine sample and is followed by states approached by successive illumination. As obvious from Fig. 3.7, it gets extremely hard to lower the residual resistance further down as soon as it is below $R_{\text{res}} \lesssim 150\,\Omega$ since firstly an ever increasing illumination dose is required and secondly the exposure sensitivity ΔR in Eq. 3.1 is strongly reduced. In a final attempt, where the LED has been operated at $I_{\text{LED}} = 50\,\mu A$ for several hours, a state with $R_{\text{res}} = 120\,\Omega$ could be reached. The series represented by blue symbols comprises states approached by heating as discussed above. Finally a third series of decreasing R_{res} is included as green symbols. The states of this last series are tuned into again by illumination. As already discussed while presenting Fig. 3.7, R_{res} in the first and last series is a unique function of D. Accordingly T_c a function of R_{res} agrees for the red and the green series quite well. For the blue series T_c is baldly larger for a given R_{res} than for the other two. Obviously, T_c is *not* completely determined by the residual resistance. By analyzing the I/U characteristics in Sec. 3.3 it is clear that the current density within the sample, which is supposed to probe the resistance, reflects the inhomogeneous nature of the studied interface and such inhomogeneities seem to be intrinsic to STO based 2DESs (Benfatto *et al.* 2009; Goble *et al.* 2017). The superconducting transition recorded in a four probe setup as used here is mostly sensitive to the high conductive parts of the structure, if inhomogeneities are present. And a single superconducting path between the voltage terminals can falsely be interpreted as perfect conductance of the whole structure. When the temperature is lowered continuously and superconductivity sets in gradually in different mesoscopic regions at various instants, a complicated and changing current density pattern results. It is probed by the voltage terminals as a single potential difference giving some kind of averaged conductance value. This procedure is in principle not sufficient to fully characterize an inhomogeneous situation. Nevertheless, it has the advantage of being conceptually simple and highly sensitive to changes even in minor regions between the voltage probes.

In general, R_{res} positively correlates with T_c. This is true for the three series presented in this section and also for all samples studied in the course of this thesis. In Fig. 3.9 b) T_c varies between $T_c = 187\,mK$ for $R_{\text{res}} = 120\,\Omega$ and $T_c = 265\,mK$ for $R_{\text{res}} = 600\,\Omega$.

An increase of T_c with resistance is reported by many authors in the so called "over-doped regime" (see *e.g.* Gariglio *et al.* 2016). In these experiments the field effect is used to tune the charge carrier density of a STO based 2DES by applying a voltage V_g to a gate electrode. The change of charge carrier density n is reflected strongly in the sheet resistance $R_\square$ and as function of V_g one observes in many cases the celebrated superconducting dome marked by (as a function of electron density) an increase of T_c in the so called "under-doped regime" followed by the decrease of T_c above some optimally doped situation.
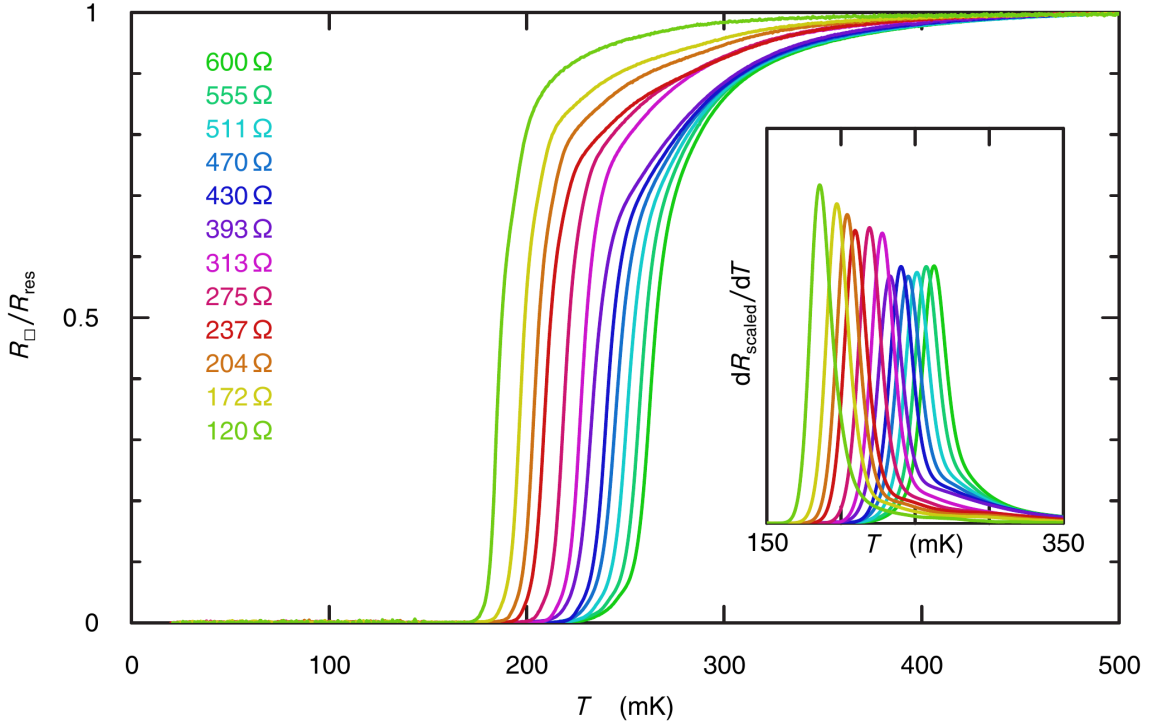
Figure 3.10: Scaled sheet resistance $R_\square/R_{res}$ as function of temperature T for different illumination steps indicated by various colors. Derivative shown in inset.

It is instructive to view the data of Fig. 3.9 a) scaled by R_{res}. Indeed, in Fig. 3.10, where $R_\square/R_{res}$ is shown as a function of temperature, the changes of the fine structure of the superconducting transition are readily apparent besides the shift in transition temperature. Again the first six curves with the highest T_c (*i. e.* those recorded before the pronounced jump in Fig. 3.6) possess a different signature than the rest. These curves scale nicely on top of each other for $T \gtrsim 290$ mK and a shift of the transition is seen most clearly for $R_\square/R_{res} < 0.7$. It is not possible to describe the curves as a, *e. g.*, usual BKT transition, which would be the natural choice for a two dimensional superconductor. Actually, the superconducting transition in STO based 2DESs has been identified as being of the BKT type (see Sec. 2.2) and this fact established the proof of the two dimensional nature of the electron system at the interface. In Ch. 4 a careful analysis of I/U characteristics at small currents close to T_c sig-

nals how well the samples investigated here fit the BKT picture. Nonetheless, the complete transition as displayed in Fig. 3.10 is too strongly structured to be caused by an ordinary two-dimensional superconductor. On the contrary, it gives evidence of the inhomogeneous nature of the interface under investigation. Most probable the sample consists of regions with different superconducting gap energies and correspondingly varying T_c. Within this scenario, the turn down below $T \lesssim 400\,\text{mK}$ of the first six curves in Fig. 3.10 would correspond to a minor portion of the sample going superconducting (signaled by fluctuations) at a higher T_c than the majority part, whose T_c is actually more sensitive to illumination. This would also allow a simple explanation for the apparent change between curve number six and seven in Fig. 3.10: The pronounced jump in R_{res}, which occurred between these measurements (see Fig. 3.6) results from a reordering of mesoscopic regions, which are coupled to a yet hypothetical defect structure related to grain boundaries, dislocation lines, or the like. The spacial arrangement of mesoscopic regions reached after the jumps seems to be stable for the next three states, before further jumps during illumination signal further discontinuous reordering processes. The last state has obviously the smallest transition width, representing thus—in the line of this arguments—the most pure arrangement one can get to by the illumination process.

The speculative reasoning of the last paragraph gets further support from an analysis of I/U characteristics pursued in the next section.

3.3 I/U characteristics at low temperatures altered with light

To support the interpretation given at the end of the last section, I/U characteristic will be presented now. The current source for I/U characterization is build by an arbitrary wave function generator (Model AM300, Rhode & Schwarz GmbH & Co. KG, Germany) in series with a $1.37\,\text{M}\Omega$ resistor network which drives a linearly ramped up current through the leads of the Hall bar structure. The voltage drop U_{xx} is recorded by a multimeter HP 3458A (HP Inc., USA). In this section only measurements deep in the superconducting regime are presented. No temperature dependence could be detected in the I/U characteristics below a sample stage temperature $T_{ss} < 100\,\text{mK}$. For the sake of definiteness T_{ss} was PID stabilized at $T_{ss} = 50 \pm 2\,\text{mK}$. The inset of Figure 3.11 shows exemplary the behavior for a homogeneous system. Beginning with a small applied current in the superconducting state, the system has no resistance when the current is increased (zero voltage measured). Exceeding the critical current I_c leads to a jump in I/U characteristic to the resistive state (green curve). The slope of the I/U characteristic follows an ohmic behavior with a joule heating in this resistive state. Therefore by lowering the current indicated by blue broken lines, the magnitude of the retrapping current I_r is smaller than I_c. The effective temperature is unknown due to dissipation effects.
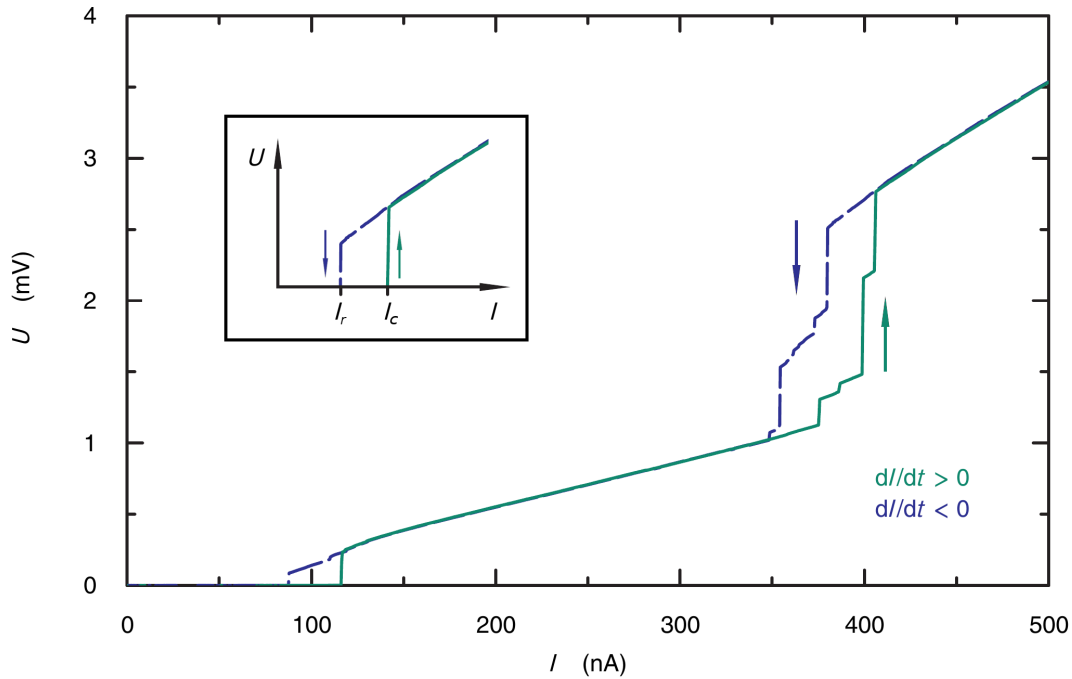
Figure 3.11: Voltage U as function of current I at 50 mK in zero magnetic field measured for pristine state. Green solid line indicate an increasing current, dashed blue line represents characterization with lowering the current magnitude. Inset contains a sketch of an ideal I/U characterization for a homogeneous system.

Figure 3.11 gives a typical example of a I/U characteristic curve (before illumination with $R = 600\,\Omega$), where the green solid line was recorded during an increasing current and the blue broken line for decreasing currents. Up to the apparent hysteresis the I/U characteristic curve happen to be completely symmetric. Perfect conductance, *i. e.* vanishing voltage drop, is found below $I = 89\,\text{nA}$. On increasing the current its critical value is found to be $I_c = 116\,\text{nA}$ at which point the characteristics switches to a final voltage state. The slope above $I = 116\,\text{nA}$, however, does not correspond to the normal state resistance but is considerable lower. In the range of $375\,\text{nA} < I < 405\,\text{nA}$ a cascade of further jumps in voltage drop is found resulting in the expected normal state behavior for $I \gg I_c$. This can be understood in a stepwise transition from a superconducting to a resistive state, where different parts of the conducting interface in a continuing series going dissipative with increased applied current. Thus the I/U characteristics display in addition to the superconducting regime at low current and the normal state at high current an intermediate range of pronounced subgap features. While subgap features can have a variety of origins (see *e. g.* Barone *et al.* 1982), the most probable source in the present case are inhomogeneities along the current path. Further experiments presented in Ch. 4 have been performed on samples with a more complex layout which allows to monitor different locations on the interface. There, further evidence for the inhomogeneous nature of STO based 2DES is found.
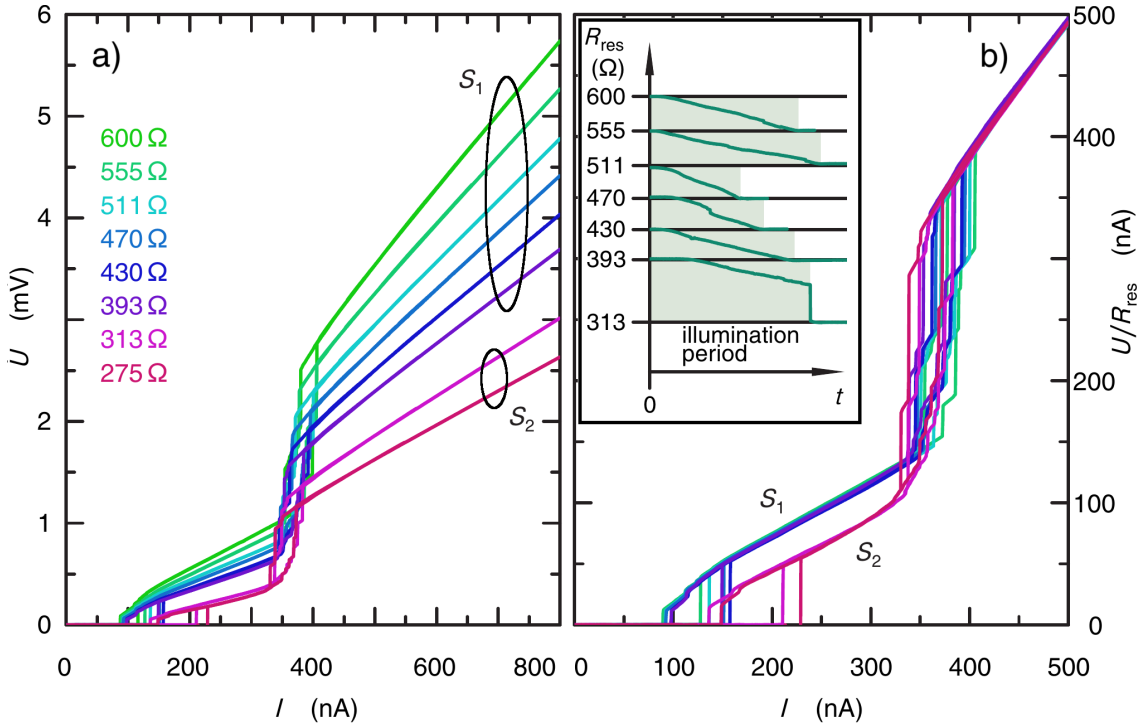
Figure 3.12: a) Voltage U as function of current I at $50\,\text{mK}$ in zero magnetic field for six successive states in S_1 and S_2. b) Same data scaled by R_{res}. Inset adapted from Fig. 3.6.

Here the assumption that subgap features result from a specific current density pattern imprinted by the spacial inhomogeneous distribution of the gap energy is explored in the light of illumination induced changes. As shown in the previous section the pronounced jump visible in Fig. 3.6 (reduced representation in inset of Fig. 3.12 b)) naturally splits the first series of illumination induced states into two sets before and after the jump between the $393\,\Omega$ resistive state (labeled state S_1 as of now) and the $313\,\Omega$ state (S_2). In Fig. 3.12 a) the last six I/U characteristic curves in S_1 are compared to the first two curves in S_2. For this purpose the characteristics have been scaled as U/R_{res} in the right panel so as to collapse the normal state behavior at high current to the identity function $U(I)/R_{\text{res}} = I$ (see Fig. 3.12 b)). In doing so, it is disclosed for the curves from S_1 that the characteristics in the subgap region scale exactly like the normal state resistance upon illumination (collapse of subgap regime like resistive regime). This is strong evidence for the hypothesis of a correspondence between subgap features and a geometrically defined subdivision on a mesocopic scale into regions of varying critical currents. It can be assumed, that the mesoscopic fine structure remains fixed during illumination in state S_1. Only a slight scatter in the switching and retrapping behavior is visible which can easily be caused by the statistical nature of these processes. However, a remarkable change in the subgap region arise from the light-induced jump separating S_1 and S_2. Moreover, the change is more related to the relative height of the subgap voltage than to the slope, which happens to be quite similar before and after the

sudden change of R_{res} in the inset of Fig. 3.12 b). Again, this strongly supports the hypothesis of a relation between subgap features and mesoscopic structure, which eventually changes discontinuously upon light-induced resistance reduction.

Figure 3.13 summarize the findings for the curves in S_2. Upon further illumination the subgap features in the scaled I/U characteristics get more and more unstable. In S_2 only the first two states collapse ($R_{\text{res}} = 313\,\Omega$ and $R_{\text{res}} = 274\,\Omega$ indicated magenta) to a well comparable behavior upon scaling, while the remaining states display much more variation, which refuse to be read as a clear trend (starting with $R_{\text{res}} = 237\,\Omega$ represented in red color). Only the final state with $R_{\text{res}} = 120\,\Omega$ indicated in bright green is remarkably different from all other states. It does *not* show a reduced resistance upon an initial switching event followed by a cascading number of smaller jumps before the normal state is approached. It features a much higher critical current of $I_c = 770\,\text{nA}$ and switches directly to the normal state branch. In this state the sample retrappes into superconductivity in an almost textbook like manner. Within the proposed underlying mechanism devised here, long exposure of the interface forced it into a low resistive state which is characterized by a more homogeneous appearance of superconductivity, caused most probably by an increased size of the mesoscopic subdivisions.
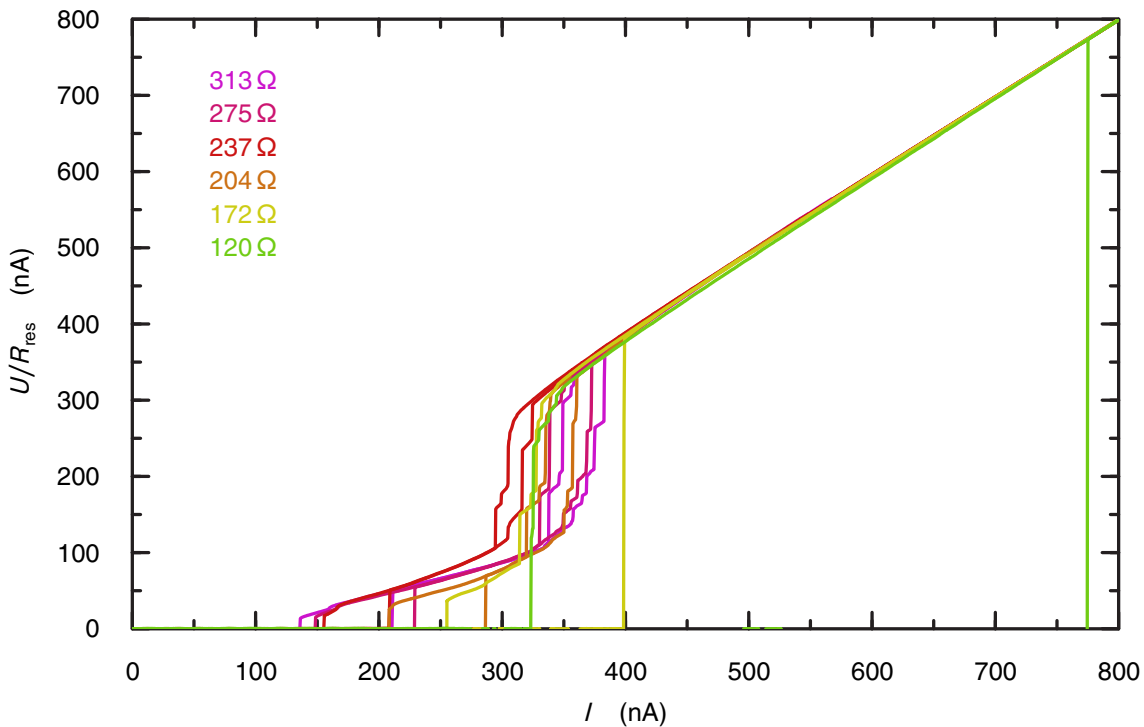

Figure 3.13: Normalized Voltage U/R as a function of the applied current I at $50\,\text{mK}$ without applied magnetic field for different illumination steps represented with various colors.

Figure 3.14 display scaled I/U characteristics for states approached by heat treatment of the interface. The states shown correspond to the blue dots in Fig. 3.9 b). Adopting the interpretation of developed in this section, the pure state reached after long exposure is maintained during a considerable number of states marked by increasing R_{res}. This changes abruptly for $R_{res} = 490\,\Omega$, where subgap features signal the reappearance of a finer mesoscopic subdivision. In Fig. 3.9 b) T_c is considerable higher for the states approached during a rising R_{res} (blue dots) compared to states approached by illumination (red and green dots). This has a natural explanation when taking into account the findings on the I/U characteristics presented in this section.
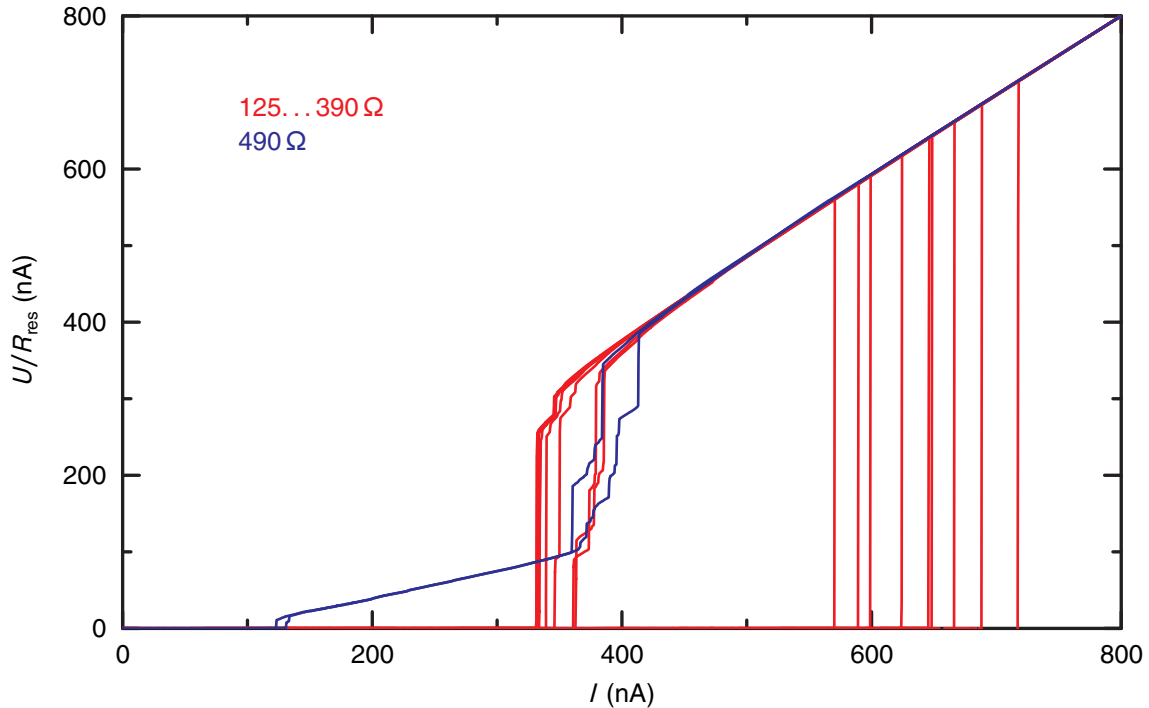
Figure 3.14: Normalized Voltage U/R as a function of the applied current I at $50\,mK$ for different relaxation steps after illumination without applied magnetic field. Red color indicates residual sheet resistance values between $125\,\Omega$ and $390\,\Omega$. Blue I/U characteristic has a residual sheet resistance of $R_{res} = 480\,\Omega$.

3.4   Influence of light to magneto-transport

Electrical transport at the LAO/STO interface in the various resistive states induced by exposure to light is studied also as a function of magnetic field B.

An analysis of magneto-transport gives further insight in normal and superconducting properties, which cannot be probed at $B = 0$. As already discussed in Sec. 2.2.1, a variety of transport parameters are sensitive to a magnetic field. For instance, the spin-orbit scattering time $\tau_{s.o.}$ and phase relaxation time τ_φ can be probed by weak localization at small to moderate magnetic fields. This phenomenon is superimposed on the more classical magneto-resistance, which is observed in materials of non-trivial band structure (*e.g.* Ziman 1972). In general, the latter contribution to magneto-transport derives from details of the Fermi surface and can, in principle, derived from the band structure on the basis of a semi-classical treatment. This is an elaborated task and in most cases the analysis of magneto-transport relies on simplifying models. This does, however, lead only to a qualitative description, focusing on features like the quadratic curvature at small fields and saturation at large fields of $R_{xx}(B)$ or the change of slopes at small and large fields of $R_{xy}(B)$. In many cases it is difficult or even impossible to relate changes in parameters deduced by simple models to actual changes of the Fermi surface, which are to take responsible for variations in magneto-transport in the first place. Thus, simplifying models, though capable to parameterize the generic appearance of magneto-transport, are of limited use in many cases.

We will discuss magneto-transport measurements collected at 500 mK in the course of the first illumination series and include for comparison an additional resistive state approached during the recovery procedure.
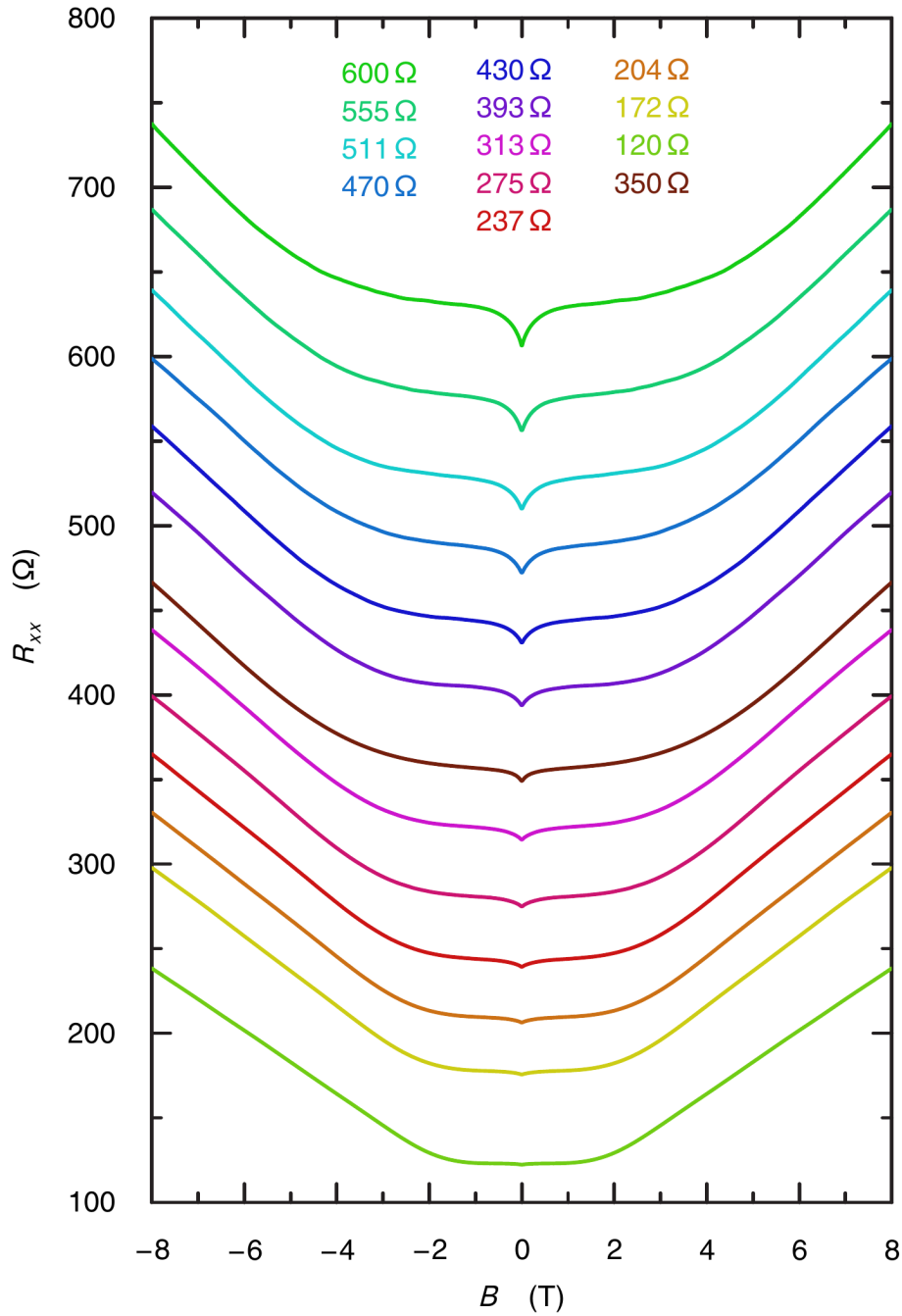
Figure 3.15: Magneto-resistance R_{xx} for different resistive states as function of magnetic field B at 500 mK. Sample without illumination (dark green) shows quadratic behavior of the magneto-resistance at high magnetic fields and a weak anti-localization dip at low fields. With increased illumination the resistance is going down. Simultaneously the high field magneto-resistance develops into a more linear behavior. The presented measurements corresponds to the resistive states of Figure 3.9 a), except for data displayed in brown with $R_{xx}(0\,\text{T}) \approx 350\,\Omega$, which are taken from the set of states approached during resistance recovery.

Figure 3.15 displays the magneto-resistance R_{xx} in dependence of B at $T = 500\,\text{mK}$. B was ramped in positive and negative orientation with respect to the [001]-direction of the sample. The pristine state of the LAO/STO interface (dark green) shows a nearly quadratic behavior of the resistance at high magnetic fields with a superposition of a dip at low magnetic fields attributed to weak *anti*-localization (WAL), which will be discussed in further detail below. Weak localization leads to a peak in magneto-resistance with a maximum at $B = 0\,\text{T}$ which flips sign if spin-orbit coupling is increased. Strong spin-orbit coupling is expected in LAO/STO, especially at the so-called over-doped side of the superconducting dome.

With increasing illumination dose D and decreasing residual sheet resistance R_{res}, the curvature of $R_{xx}(B)$ at higher fields is reduced and $R_{xx}(B)$ tends to approach a straight line, most apparently for the final resistive state (bottom most curve). Moreover, $R_{xx}(B)$ in the final state is almost constant at small fields and the change to a nearly constant slope at higher fields yield to a rather sharp knee in the data. In literature, the deviation from a quadratic dependency with a non-saturating behavior of magneto-resistance at high fields is discussed as indicator for an inhomogeneous resistor network, *e.g.* by Parish *et al.* 2003, which is not in line with the behavior of I/U characteristics under influence of light described earlier.

We take a closer inspection of the measurement displayed in brown shown in Fig. 3.15, which possess a zero field resistance of $R_{xx}(B = 0) \approx 350\,\Omega$. It is recorded in a resistive state approached by heating during resistance recovery as described above. Fig. 3.14 indicated that this state belongs to a marked set of states with an increased size of mesoscopic subdivisions. The measurements adjacent to the brown curve, on the other hand, display a much richer structure in I/U characteristics. Apparently, this is reflected in the $R_{xx}(B)$ measurements as well; the detailed functional dependence of R_{xx} on B is not completely determined by R_{res}, but is influenced by particularities of an internal structure. This behavior is further discussed with reference to Fig. 3.20 in terms of Kohler's rule (Kohler 1938).

Since the weak anti-localization dip seems to diminish with increasing D, we will take a closer look at smaller B up to $\pm 2\,\text{T}$. In Figure 3.16 the conductance change $\delta G(B) = R_{xx}^{-1}(B) - R_{xx}^{-1}(0)$ is plotted at magnetic fields $-2\,\text{T} < B < 2,\text{T}$, where it is dominated by WAL contributions. In this way of presenting the data it is apparent that the contribution of WAL to the conductance is essentially unaltered by illumination; a peak in conductance (as opposed to a weak localization dip) around $B = 0$ is clear evidence for a dominating spin-orbit interaction. However, the concrete form of the pronounced peak in Fig. 3.16 cannot be used to evaluate the spin-orbit relaxation time $\tau_{\text{s.o.}}$. The weak localization corrections possess in the crossover regime of $\tau_\varphi \sim \tau_{\text{s.o.}}$ a non monotonic dependence on magnetic field: A narrow positive peak around $B = 0$ is superimposed on a much broader one of opposite sign resulting in a functional dependence with a maximum at a specific field strength, which rapidly grows with $1/\tau_{\text{s.o.}}$ (see Fig. 2.4). As soon as this maximum is outside of the experimentally accessible field range, one is blind to the exact strength of the spin-orbit interaction. This is the case in the present situation. The width of the peak in Fig. 3.16 is solely

determined by the phase relaxation time τ_φ, or equivalently by the inelastic scattering length $L_\varphi = \sqrt{D\tau_\varphi}$, where D is the diffusion constant.
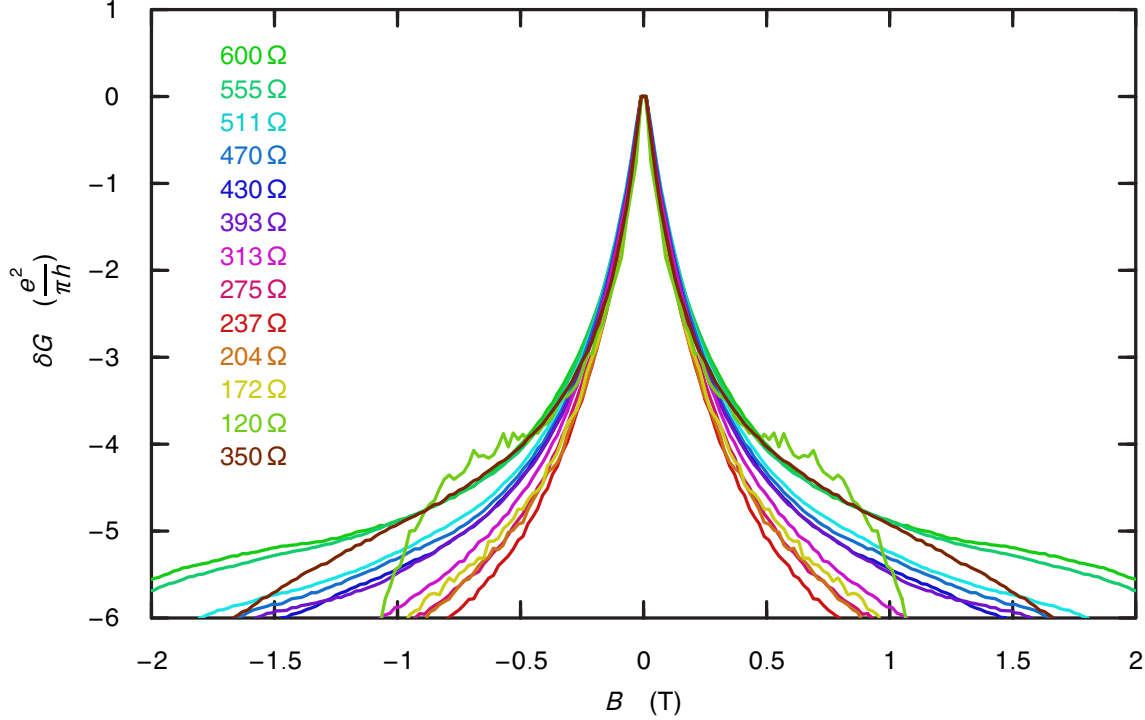

Figure 3.16: Change in conductivity δG normalized by $\frac{e^2}{\pi h}$ for different illumination steps indicated by different colors corresponding to the resistive states of Figure 3.9 a), except for the brown measurement curve at $R_{\text{res}} \approx 350\,\Omega$ from the resistance recovery run after illumination.

It has to be stressed, that WAL theory is a perturbation theory working best at small magnetic field, where the right hand side of Eq. 2.3 approaches a simple parabolic shape [3]. For a 2DES with strong spin-orbit interaction we expect according to Eq. 2.4

$$\delta G = -A \cdot f(B, B_\varphi), \tag{3.3}$$

where the constant A is strictly $1/2$ due to the quantum nature of weak localization, and the function f is defined in Eq. 2.3.

To describe the peak in Fig. 3.16 the parameter $B_\varphi = \hbar/(4eL_\varphi^2)$ in Eq. 2.4 has to be chosen in the range of several mT. It turns out, however, that without adjusting A to a different value no satisfying description of the data by Eq. 3.3 can be achieved. Only by setting $A = 2.8/2$ and allowing B_φ to vary freely it is possible to bring Eq. 3.3 into agreement with the data in Fig. 3.16. The thirteen measurements in Fig. 3.16 have been used to evaluate

---

[3]In the limit of large fields (Eq. 2.3) can be approximated by a logarithm, but the validity of the perturbation ansatz has to be checked with care for large fields.

$L_\varphi = \sqrt{\hbar/4eB_\varphi}$. The mean and standard deviation of this fitting parameter is given by $L_\varphi = 176\,\text{nm} \pm 7\,\%$, which is a rather small but reasonable value for a phase coherence length at $T = 500\,\text{mK}$. In Fig. 3.17 the result of the parameter adjustment is shown in a field range $-100\,\text{mT} < B < 100\,\text{mT}$, where the match between theory and experiment is expected to be best.
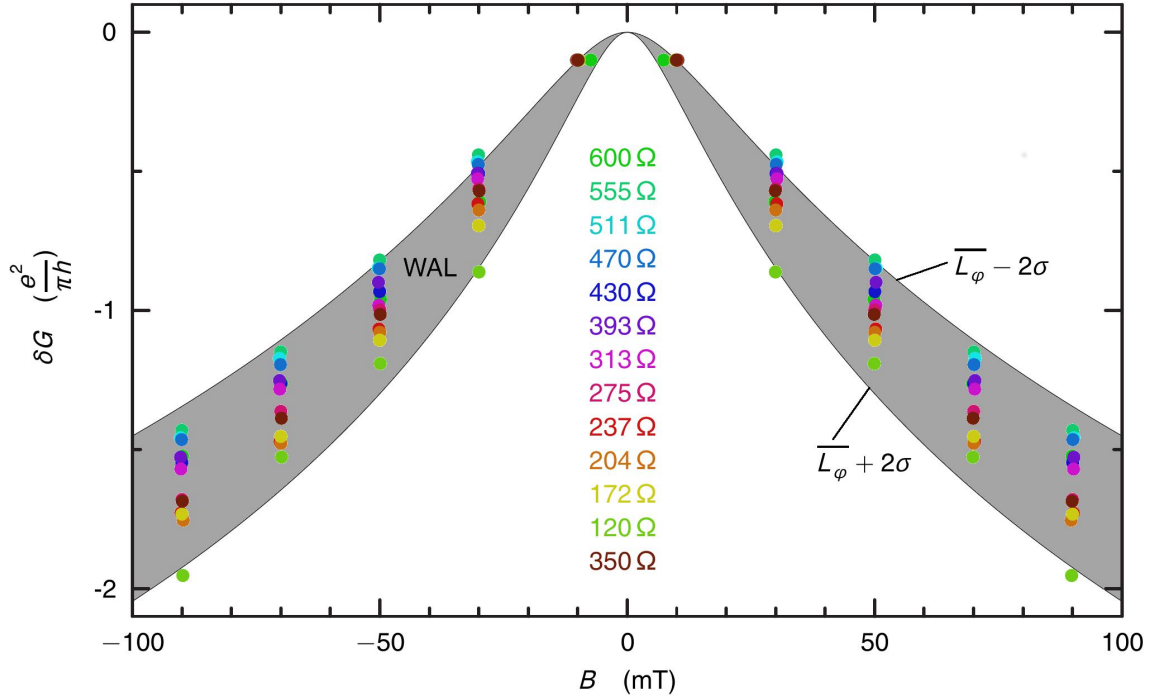

Figure 3.17: Change in conductivity (colored dots) for different illumination steps at $|B| < 100\,\text{mT}$ overlaid by predictions of WAL theory. The theory is fitted by adjusting the inelastic coherence length L_φ for each individual measurement. A statistical analysis of the fitting parameters yield a mean of $\overline{L_\varphi} = 176\,\text{nm}$ and a standard deviation of $\sigma = 7\,\%$. The shaded area corresponds to WAL predictions in the range $L_\varphi = \overline{L_\varphi} \pm 2\sigma$.

As said before, the factor 2.8 is not in line with the quantum nature of the WAL correction. It is thus clear evidence that the 2D WAL theory fails to describe the experimentally observed corrections to conductivity. Such a failure is expected whenever the studied film deviates strongly from the prerequisites used in the derivation of WAL theory. These latter include, *e. g.*, (i) the homogeneity of the studied film whose thickness has to be smaller than L_φ, (ii) the point like nature of scattering centers of sufficient density which leads in a semi-classical picture to a diffusive motion of charge carriers, and (iii) ergodicity which makes it possible to consider an average over the arrangement of scatterers when calculating the response to a magnetic field. As already conjectured previously, the investigated sample does not consist of a homogeneous film. Furthermore, it is believed that scattering centers are clustering at dislocation lines, step edges of surface terraces (see Ch. 4) and/or domain

boundaries of the AFD. In either case the disorder average at the heart of WAL theory is problematic and a more sophisticated model of the weak localization correction might lead to an altered dependence on magnetic field. An detailed analysis of this problem is quite demanding. It is however easy to see, how inhomogeneities can lead to an apparent increase of the weak localization contribution.

Consider the most simple example of an inhomogeneous arrangement consisting of two adjacent squares which differ in resistance: $R - R'$ and $R + R'$. If probed by a current flowing in series through both squares, the arrangement has a total resistance of $2R$ independent of R'. If both square exhibit a universal weak-localization correction δG_{WL} to the respective conductance $1/(R \pm R')$ the total resistance change is approximately given by $\delta G_{\mathrm{WL}}((R - R')^2 + (R + R')^2 = 2\delta G_{\mathrm{WL}}(R^2 + R'^2)$, which has a minimum in the homogeneous case, $R' = 0$, which equals the universal expectation value for the combined squares. An inhomogeneous distribution of resistance leads to an apparent enhancement of weak localization.

In summary, it is found experimentally that the weak localization contribution is larger than the prediction of WAL theory. This finding has a natural explanation if the inhomogeneous nature of the investigated sample is taken into account. The WAL peak of all illumination induced states of different resistances can be described in the small filed range $|B| < 100\,\mathrm{mT}$ by the standard WAL formula for quasi two-dimensional films (of thickness smaller than L_φ) modified by a proper enhancement factor which is constant for the whole series of states. The parameter B_φ describing the width of the WAL peak varies only slightly. This leads to the conclusion that the phase coherence length is constant within the experimental resolution.

Figure 3.18 shows the transversal resistance R_{xy} vs. B at $T = 500\,\mathrm{mK}$ in different resistive states. Again both magnetic field orientations were investigated and used here to gain measurement precision by anti-symmetrization of the data, which are displayed in Fig. 3.18 for $B > 0$. In the pristine state (dark green) a nearly linear behavior of the Hall resistance with a slight upturn at higher magnetic fields is visible. With increasing D derivations from a linear relation between R_{xy} and B becomes more pronounced. A kink marking the onset of non-linearities migrates to smaller fields with increasing illumination dose D. At the same time the small field Hall coefficient $R_H = \mathrm{d}R_{xy}(B = 0)/\mathrm{d}B$ is unaltered.
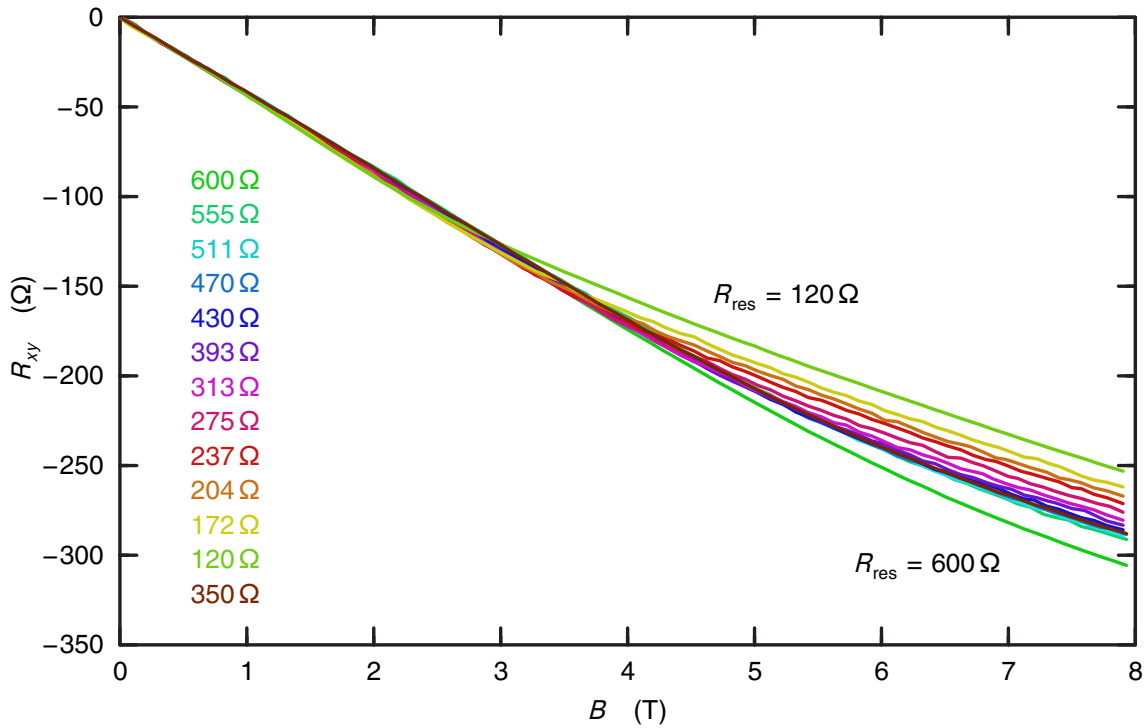
Figure 3.18: Hall resistance R_{xy} at 500 mK versus magnetic field B for different illumination steps indicated by different color corresponding to the resistive states of Figure 3.9 a), except for the brown measurement curve at $R_{res} \approx 350\,\Omega$ from the resistance recovery run after illumination.

The simplest model capable to produce magneto-resistance, $R_{xx} \neq$ const., and a non-linear Hall effect, $dR_{xx}(B)/dB \neq$ const., contains two parabolic bands and four parameters, namely $\mu_{1,2}$ and $\sigma_{1,2}$, where μ and $\sigma = ne\mu$ label mobility and conductivity, respectively, and the subscripts number the band; n is the charge carrier density. It reproduces the generic features of magneto-transport (quadratic magneto-resistance at $B = 0$; a Hall slope relating to the total charge carrier concentration as $n_{tot.} = 1/eR_H$ in the high B limit; and saturation of magneto-resistance in the same limes). A thorough analysis of magneto-transport has to take the quantities $R_{xx}(B)$ and $R_{xy}(B)$ into view on the same footing as both emerge directly from the underlying resistance tensor. A closer look into the analytical formula for the 2-band model[4] reveals that the nearly constant Hall slope observed at $B = 0$ in Fig. 3.18 is incompatible with the changes in $R_{xx}(B)$ as reported by Fig. 3.15. By increasing the number of bands (Arnold *et al.* 2018), matching between experimental data and the model could be improved considerably mainly due to more flexibility provided by additional bands. The model had to assume three bands. Besides an electron like band of constant density and

---

[4] $R_{xx}(B = 0) = 1/(\sigma_1 + \sigma_2)$, $R_H(B = 0) = R_0^2(\sigma_1\mu_1 + \sigma_2\mu_2)$, $R_{xx}(B) = R_0 + CB^2 + \mathcal{O}(B^4)$, $C = R_0^3(\sigma_1\sigma_2(\mu_1 - \mu_2)^2)$

tunable mobility, a hole band of constant mobility and tunable density was postulated. A third band with a cosine tight binding dispersion finally makes it possible to tune the character of charge carriers between hole and electron properties. This model is not well justified by band structure consideration and was merely proposed as toy model to show the ingredients necessary to fit the experimental findings, *i. e.* a considerable change in R_{res} and at the same time a nearly constant Hall slope at small B. Hole type carriers were needed to prevent large changes of the total charge carrier concentration as a response to a changing conductance. The tight binding band, finally, provided the flexibility to adjust the magneto-resistance. However, even this model fails completely to describe the aforementioned peculiar shape of $R_{xx}(B)$ in the final state.

Most probable a more appropriate description of magneto-transport derived directly from the well established band structure of the LAO/STO interface by a semi-classical treatment would lead to the same conclusion; the experimental observed magneto-transport represented by Fig. 3.15 and 3.18 is not observed in a homogeneous film, but emerges as a result of intrinsic inhomogeneities of the LAO/STO interface.
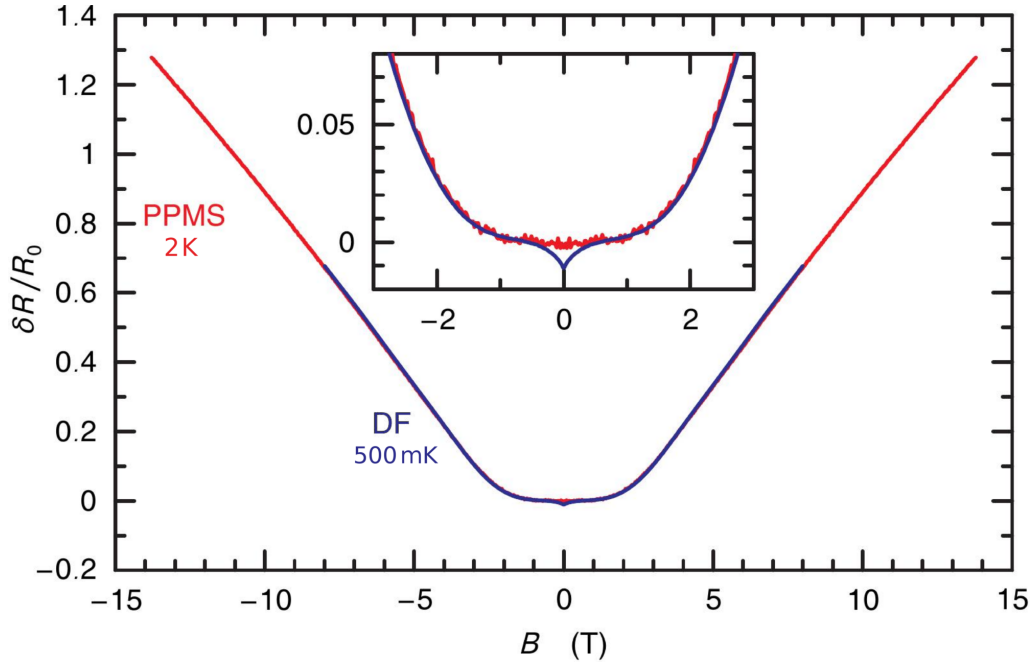

Figure 3.19: Comparison of change of $\delta R/R_0$ in dependency of B in dilution fridge (blue at 500 mK) and PPMS (red at 2 K). Inset shows a zoom to small B with a visible WAL dip at low temperatures.

An important question which requires attention is whether the seemingly linear behavior implied by the measurement of $R_{xx}(B)$ in the final state between $2\,\mathrm{T} \lesssim B < 8\,\mathrm{T}$ signals the onset of saturation which gets apparent only at larger B. To address this question, measurements in the PPMS, equipped with a stronger magnet, have been conducted. The LED

was centered again over the sample allowing to tune the resistance at low temperatures. A new data acquisition system (described in details in Sec. 2.4.3) was transferred from the DR system to the PPMS to record the different voltage terminals simultaneously with a lock-in technique. The PPMS system controlled the temperature and magnetic field, which was recorded using the analog output of the PPMS control unit. To make a comparison with the data already collected in the DR system, the sheet resistance at 2 K was tuned to a value comparable to a resistive state already investigated in the DR system at $T = 500$ mK. Figure 3.19 presents the magneto-resistance measured in the different systems in these states ($R_{xx}(B = 0)$ was equal to 175.5 Ω and 178.5Ω in the DR and the PPMS, respectively) up to the maximal available field. The figure show impressively that the apparent linear behavior seen in the DR system continuous up to at least 14 T. The inset displays the appearance of the WAL at low temperatures ($T = 500$ mK) which is suppressed at an elevated temperature of $T = 2$ K.

To finish the presentation of the measurements done in the PPMS, Fig. 3.20 shows $R_{xx}(B)$ and $R_{xy}(B)$ for two states of similar resistance at $2\,K$ ($R_{xx}(B = 0) = 493\,\Omega$ and $R_{xx}(B = 0) = 495\,\Omega$ in red and blue, respectively) which were approached with two different irradiation doses D. While the Hall resistance almost perfectly agrees, the magneto-resistance curves deviate from each other at fields above $B > 3\,T$. This clearly violate Kohler's rule (Kohler 1938), which states that $R_{xx}(B)/R_{xx}(0)$ is a universal function of $B/R_{xx}(0)$, which depends solely on the band structure. The observed changes in $R_{xx}(B)$ are thus clear evidence that the resistance change is not induced by a simple change of mobility. It either results from changes in the Fermi surface (induced by, *e. g.*, a changing charge carrier concentration) or, a position favored throughout this thesis, a change in the internal structural arrangement of inhomogeneities. Therefore details of the measured magneto-resistance depend on changes of an underlying internal structure.
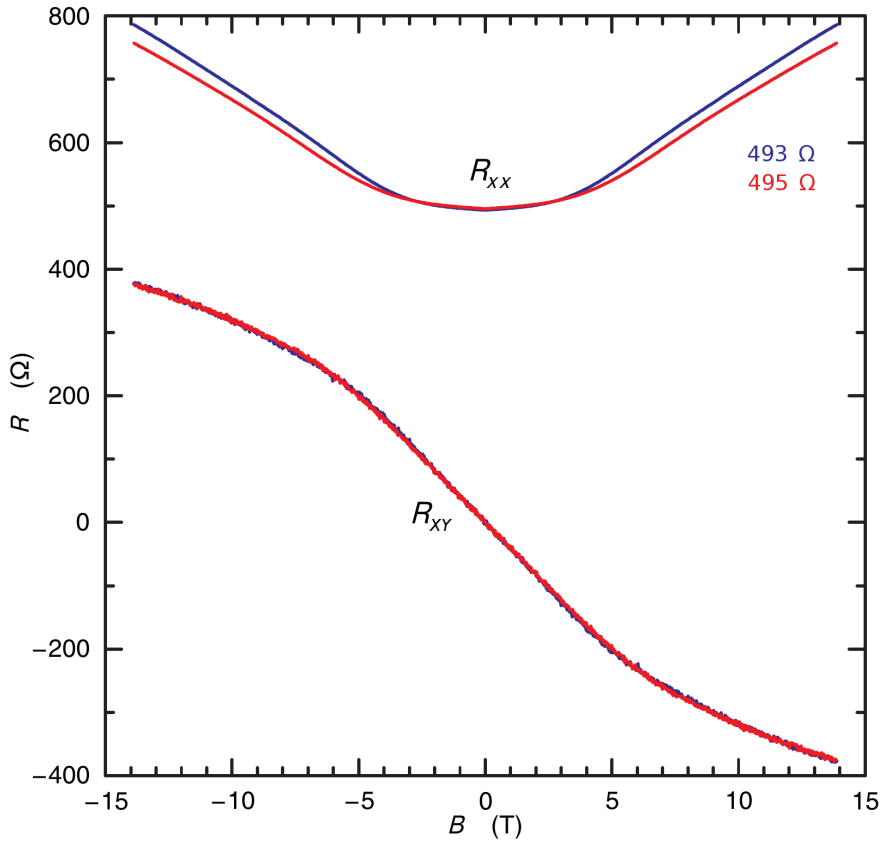
Figure 3.20: R_{xx} and R_{xy} as function of B for comparable R_{res} indicated blue ($R_{xx}(B = 0) = 493\,\Omega$) and red ($R_{xx}(B = 0) = 495\,\Omega$) with a different irradiation dose D. Measurements performed at $T = 2\,K$.

3.5 Summary

In this chapter a new control parameter for the superconducting transition temperature T_c for STO-based interfaces was introduced. A LED capable of illumination at low temperatures down to the base temperature of the DR ($T = 12\,\text{mK}$) was characterized first. A shift in the I/U characteristics of the LED to higher voltages was determined for decreasing temperatures. With an home-build setup the radiant flux of the LED could be linked to the applied electrical power using a maximal current $I_{\text{max}} = 50\,\mu\text{A}$, which is orders of magnitude smaller than the minimal current $I_{\text{min}} = 100\,\text{mA}$ recommended by the manufacturer. Using different coatings of the temperature sensor leading to distinct spectral weight of the absorbed LED light at low temperatures, the radiant intensity at the primary emission line was investigated.

The characterized LED was utilized to illuminate a LAO/STO sample in the DR at $T = 500\,\text{mK}$. The transport properties of the interface did change as a function of the irradiation dose D. With increasing D a reduction of the residual sheet resistance R_{res} and the superconducting transition temperature can be measured and is stable over time when the light is turned off. This allows to tune R_{res} to Ω precision. The maximum photon energy at low temperatures was found to be below the band gap of bulk LAO and STO (Weakliem *et al.* 1975; Lim *et al.* 2002). A logarithmic behavior of R_{res} as function of D can be well described by a phenomenological formula. A reduction of R_{res} and T_c at the same time is found in electric-field gated interfaces above a critical gate voltage at which T_c reaches a maximum (Caviglia *et al.* 2008). This puts the LAO/STO sample investigated here in the so-called over-doped regime. In this chapter persistent photo-conductance at low temperatures as a non-volatile tuning parameter of R_{res} and T_c was introduced. The effect of altering the transport characteristics can be simply reversed by elevating the samples temperature above $T > 1\,\text{K}$. In the DR, R_{res} can be completely reversed with thermal treatment at $T \approx 12\,\text{K}$. This is in contrast to the photo-conductance changes reported by Yazdi-Rizi *et al.* 2017, where the resistance recovery to the pristine state required a heating above the AFD transition temperature $T_{\text{AFD}} = 105\,\text{K}$. The authors exposed the LAO/STO interface using UV-light with much higher energy, while here a careful illumination with photons of energy below the band gap of STO was used at very low temperatures. This shows that the mechanism by which persistence photo-conductance is induced differs in a subtle way. The main effects is probably not the production of further free charge carriers but rather an enhanced screening of inhomogeneities by localized electronic states at low temperatures. The effect investigated in this PhD work concerns changes which are already reversed at the temperatures used in the experiments in Yazdi-Rizi *et al.* 2017. Another aspect worth mentioning here is the influence of illumination on the thickness of the 2DES system. Yazdi-Rizi *et al.* 2017 showed no effect on the thickness within their measurement resolution. Assuming this is the case for the experiments shown in this chapter at even lower temperatures the reduction of the residual sheet resistance is cause by an increased mobility. In contrast to field-effect experiments, where the thickness of the 2DES system increases with rising gate voltage in the over-doped

regime (see *e. g.* Gariglio *et al.* 2016), tuning the the transport properties of the conducting layer could be possible while presumably maintaining the thickness of the latter.

Regarding the I/U characteristics a reduction of inhomogeneity related behavior was found by increasing D. The influence of light at low temperatures on the inhomogeneities could be also seen in magneto-transport measurements. With tuning R_{res} to comparable values with different illumination dose D by thermal treatment, a similar $R_{xy}(B)$ behavior was found in contrast to a different $R_{xx}(B)$ curvature at high magnetic fields. This behavior as well as the simultaneous description of R_{xy} and R_{xx} for different illumination states using simple band models is not possible.

An open question is the influence of light on the thickness of the 2DES system. To address this question an investigation of B_{crit} parallel to the interface is needed (see *e. g.* Kozuka *et al.* 2009; Reyren *et al.* 2009; Herranz *et al.* 2015) to examine a possibility of a correlation of thickness of 2DES to illumination dose D at low temperatures. Also, measurements of LAO/STO samples fabricated under different oxygen pressures would be of interest to tune T_c in a dome-like fashion (going from the under-doped to the over-doped side).

Chapter 4

Influence of Vicinal Substrates on Electrical Transport at the Al_2O_3/SrTiO$_3$ Interface

Two-dimensional superconductivity of STO based 2DES have been discovered in the widly studied LAO/STO system used in the last chapter. In addition, it has been demonstrated for LaTiO$_3$/SrTiO$_3$ heterostructures (Biscaras *et al.* 2010) and, more recently, for the Al_2O_3/SrTiO$_3$ interfaces (AO/STO) (Fuchs *et al.* 2014). The latter is conceptually simpler than their counterparts since Al_2O_3 overgrown on STO does not possess a polar character and the celebrated scenario of a polar catastrophe as origin of the 2DES does not apply in this case (Chen *et al.* 2013). Naturally the question arises in the context of the present work, whether a persistent photo-conductance is found for the AO/STO based 2DES as well. The answer is in the affirmative as will be demonstrated in this chapter. The effect is accordingly a general feature of STO based 2DES and not restricted by specific properties of the material used to induce a finite electron density in the STO surface. Additional experiment on persistent photo-conductance which are are presented in this chapter had firstly been motivated by the prospect of finding a dome like behavior as a function of exposure dose. It was natural to envision a sample of low conductance and low T_c which upon exposure to visible light at low temperature responds with an increasing conductance and increasing critical temperature at the same time. At best it might be possible to find a maximum in T_c at some optimal exposure dose and a turn down of T_c on further illumination. Such a situation, however, has not been found so far. For all samples studied in the course of this work an increase in conductance was correlated with a decrease in T_c so as if all samples belong in the category of over-doped 2DES. As long as the mechanism by which exposure to visible light leads to persistent photo-conductance has not been identified unambiguously on a microscopic level, it is hard to exclude, nonetheless, that an "under-doped" regime exist with respect to illumination and further experiments are tempting.

The mere fact that the AO/STO system exhibits persistent photo-conductance is an im-

portant finding worth to be noted. The focus of this chapter, however, is on a different subject and the sensitivity of conductance to exposure by visible light is merely used as a tuning knob. Experiments reported in Fuchs *et al.* 2014 indicated that the superconducting properties possess a dependence on the current direction with respect to the crystallographic axis. This findings hinted towards filamentary nature of current flow in the superconducting state yielding to an anisotropy in transport coefficients. From scanning force micrographs it was obvious that the unavoidable angular misalignment of the commercial STO substrates with respect to the nominal (001) surface led to a pronounced and regular terrace structure with a step height corresponding to a single unit cell of STO. It was reasonable to associate the anisotropy of filamentary current flow with the terrace structure. To test this hypothesis experiments on Al_2O_3 induced 2DES on vicinal substrates with varying misalignment angles γ are presented here. γ is of course reciprocally related to the mean width w of surface terraces. By increasing γ it is explored whether and how an decreasing w effects the apparent anisotropy of transport. This thesis focus on low temperature properties below $T < 2\,K$ and in particular on the vicinity of the critical temperature of superconductivity T_c. A comprehensive analysis of the transport properties of the identical samples at elevated temperature has been given elsewhere (Wolff 2018; Wolff *et al.* 2020). This work identified apart from the terracing of the surface the dislocation lines in $\langle 110 \rangle$ direction (see Sec. 4.2.1) as a source of anisotropy.

4.1   Vicinal substrate angle as control parameter

Superconductivity of STO-based 2DEG has been demonstrated for different orientation of the substrate surface (Herranz *et al.* 2015; Wolff 2018). The majority of experimental studies have been performed on the (001) surface which was also chosen for the present work.

The interface preparation starts with an electrochemically polished STO substrate of typically $5 \times 5 \times 1\,mm^3$ purchased from CrysTec GmbH Kristalltechnologie (Germany). To get the required TiO_2 termination the standard procedure described in Koster *et al.* 1998 is performed. It yields almost perfect, atomically flat surfaces which are characterized with an atomic force microscope (AFM). Fig. 4.1 a) shows the surface of a nominal (001) surface after the surface preparation. The micrograph covers a $2 \times 2\,\mu m^2$ area and displays a series of flat terraces; in total 17 terraces can be counted alongside the lower edge of the picture. The step height between terraces is determined by the AFM to be $h = 390\,pm$ and coincides nicely with the lattice parameter a of cubic STO. Taking into account the terrace width $w \approx 2000\,nm/17 \approx 120\,nm$ the surface proofs to be vicinal to the (001) direction with a tilt of $\gamma = \arctan(390\,pm/120\,nm) = 0.19°$. This is well within the limits of the technical tolerance in the crystal cutting and polishing procedures of commercial available substrate materials. One of the three samples investigated in this study has been fabricated on the surface displayed in Fig. 4.1. From now on it will be referred to as Sample S_{min}, where the

subscript reminds of the tilt $\gamma_{min} = 0.19°$ the substrate—purchased as (001) STO—happens to possess.
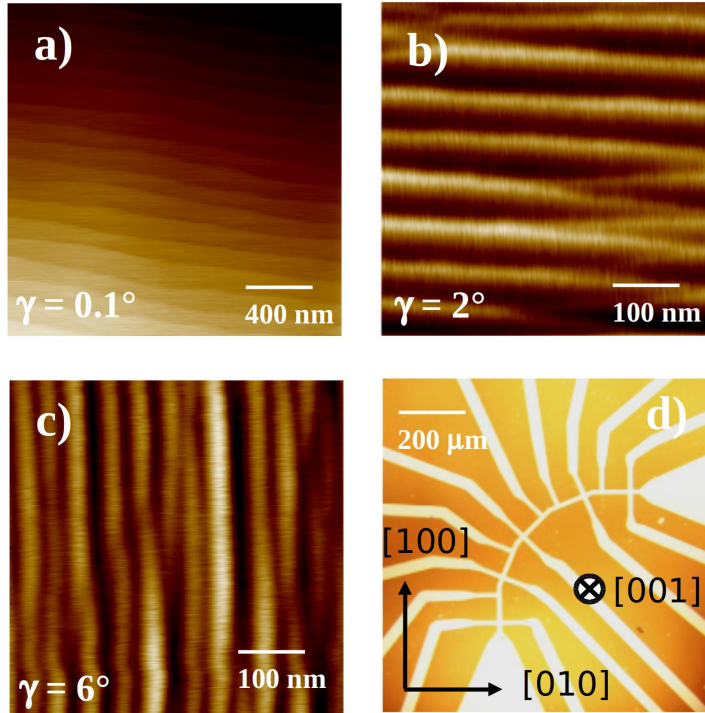

Figure 4.1: AFM measurements of the different samples (a), b) and c)) and transport measurement layout d) adapted from Wolff *et al.* 2020

Investigations on two further samples will be presented later in this chapter. The goal had been to reduce the terrace width on purpose and to learn how such a reduction is reflected in the apparent anisotropy of transport coefficients, which were observed in the past (Fuchs *et al.* 2014). To this end substrates with vicinal surfaces of enhanced tilt $\gamma = 2°$ and $\gamma = 6°$ have been purchased from the same manufacturer (CrysTec GmbH Kristalltechnologie, Germany). AFM pictures of the surfaces of these substrate can be found in Fig. 4.1 b) and c), respectively, which where taken after surface treatment for TiO_2 termination. Both surfaces clearly display atomically flat terraces of reduced width (as compared to $\mathcal{S}_{min}$), although the overall quality with respect to homogeneity has diminished considerably. Still, the intended purpose pursued here, *i. e.* to study the influence of step edge *density*, is fulfilled satisfactorily. Analyzing the height profile of the AFM data reveals that the mean height of the step edges is larger than the lattice constant a of STO on the higher γ samples. Obviously bunching of several unit cells on top of each other is energetically favorable over a shrinking terrace width as soon as the tilt exceeds a threshold. The mean step height is determined as $h = 3.6a$ and $h = 4.3a$ for the 2° and 6° substrate, respectively, and at the same time a mean terrace width of $w = 37\,\text{nm}$ and $w = 17.8\,\text{nm}$ can be extracted from Fig. 4.1 b)

and c) (Fuchs 2020). The corresponding tilts are $\gamma = \arctan(3.6a/37\,\text{nm}) = 2.2°$ and $\gamma = \arctan(4.3a/17.8\,\text{nm}) = 5.4°$ and thus very close to the manufacturer specifications. The samples fabricated on the surface visible in Fig. 4.1 b) and c) are referred to as $S_{2°}$ and $S_{6°}$ below.

Details on the patterning of microstructures by a hard-mask technique are described elsewhere (see Sec. 2.4). An optical microscope picture of a patterned sample can be found in Fig. 4.1 d). The shown layout is used for $S_{\min}$, $S_{2°}$, and $S_{6°}$. The large contacts (white areas) at the bottom and to the right are connected to leads which force a current along the 20 μm wide measurement strip visible in the center. It comprises five segments of approximately 100 μm length running in different directions with respect to the in plane crystal axes starting at the bottom in [100] direction, turning successively by 12.5°, and ending in [010] direction to the right. Each segment has three voltage terminals which are used to monitor longitudinal and transversal resistance coefficients. The terraces of $S_{2°}$ and $S_{6°}$ are forced by the manufacturer to run in [100] and [010] direction respectively, while the terraces of $S_{\min}$ are only coincidentally within 5° of a major axis. Later, the segments are tagged according to the angle φ between the terraces and the direction of current flow: The current through a segment labeled by $\varphi = 0°$ runs along terraces, while $\varphi = 90°$ signals a current crossing the step edges perpendicular. For the sake of simplicity of labels the slight misalignment of the vertical segment of $S_{\min}$ with respect to terraces is ignored. This segment will be tagged by $\varphi = 90°$ and likewise the other segments of $S_{\min}$.

4.2   Sample characterization

Before a detailed discussion in Sec. 4.2.2 a structured overview over all relevant measurements on $S_{\min}$, $S_{2°}$ and $S_{6°}$ is given in the following three subsections. For each sample in order we will consider $R(T)$ at zero field $B = 0$ for a determination of the superconducting transition temperature T_c, at $R(T)$ at increasing B to study the critical field, at the transversal resistance R_{xy} under the influence of B to study the Hall coefficient R_H and at the I/U characteristics both at $T \ll T_c$ where switching and retrapping are the prominent features and at $T \lesssim T_c$ where a Berezinskiĭ-Kosterlitz-Thouless (BKT) like transition is found.

For all samples it was possible to establish states of reduced residual resistance $R_{\text{res}} \equiv R_\square(T = 1000\,mK)$ by illumination and to reestablish the original state by heating. In general, several series of states approached by successive illumination have been investigated. The focus in this section will be on the state with the highest and the lowest R_{res}. Of course, all collected data will be included in the analysis used in the discussion later in this chapter.

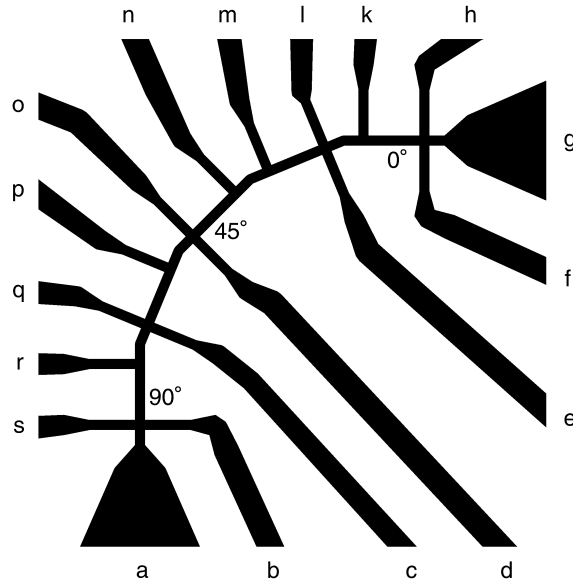### 4.2.1 Sample S_{min}: $\gamma \approx 0.19°$

Figure 4.2: A schematic representation of S_{min}. Measurements are performed on the segments labeled by values in degrees, which actually represent the segment orientation with respect to the step edges of the terrace structure (see Fig. 4.1 a).

For S_{min} a finite tilt γ results from the technical tolerance of the crystal cutting with respect to the (001) surface. $\gamma = 0.19°$ is calculated from the mean terrace width $w = 120\,\mathrm{nm}$ and the step hight corresponding to the lattice parameter of STO ($a = 390\,\mathrm{pm}$). The patterning of the surface with the layout described in Sec. 4.1 and the contacting by ultrasound wire bonding in particular was imperfect. One of the larger contacts supposed to be used as current sink happened to be defective (contact labeled "g" in Fig. 4.2) at low temperatures; a voltage terminal (labeled "f") had to be used to replace the broken contact. Additionally, the contact labeled "s" was out of order. Nevertheless, it possible to measure all relevant resistance coefficients. Straight forward is a determination of U_{xx} and U_{xy} for $\varphi = 45°$ since contacts "d", "n", and "o" are fully operational[1]. For estimating U_{xx} and U_{xy} at $\varphi = 0°$ and $90°$ the voltage differences $U_f - U_k$ and $U_r - U_b$ have been split in their symmetric and antisymmetric parts with respect to the magnetic field. By calculating U_{xx} and U_{xy} from a single differential amplifier output, two amplifier channels of the data acquisition system were spared and could be used for other purposes. They were utilized to amplify $U_n - U_f$ and $U_d - U_r$ containing information on a mixture of current directions

---

[1]Explicitly $U_{xx} = U_n - U_o$, and $U_{xy} = U_o - U_d$. Actually $U_o - U_d$ has a tiny contribution from U_{xx} due to a very small misalignment of the contact positions at opposite sides of the current path and is finite even at $B = 0$. In calculating the Hall coefficient R_H, U_{xy} is calculated from the—with respect to the magnetic field—antisymmetric voltage difference.

ranging from $0° \lesssim \varphi \lesssim 45°$ and $45° \lesssim \varphi \lesssim 90°$, respectively. Again, longitudinal and transversal resistance coefficients can be calculated by symmetrizing and anti-symmetrizing with respect to B.

4.2.1.1   Superconducting transition temperature

The sheet resistance as function of temperature $R_\square(T)$ measured at zero magnetic field for segments with $\varphi = 0°$, $45°$, and $90°$ is shown in the main panel of Fig. 4.3. As explained above, φ refers to the current direction in a given segment with respect to the direction of step edges of the terrace structure. R_res varies significantly with φ. The fact that R_res is largest for $\varphi = 45°$ excludes a simple attribution of the apparent anisotropy to the terrace structure. As pointed out in Wolff 2018; Wolff *et al.* 2020 (see Sec. 2.4 for an introduction) dislocation lines typical for STO grown by the Verneuil method can be hold accountable for an anisotropic contribution to resistance described by a tensor with main axes aligned to the $\langle 110 \rangle$ direction. In Wolff 2018 a simple model is devised in which anisotropy in transport coefficient result from the sum of two anisotropic tensors. The first contribution is described by a tensor with its main axes aligned to the terrace structure while the second tensor is aligned to the dislocation lines. This model is capable to fit the observations of directional transport in all samples with the layout used in this chapter and specifically for S_min. In the latter case the contribution by dislocations dominates over the terraces and yield to a maximum resistance when the current runs in [110] direction. The current is forced exactly in this direction in segment $\varphi = 45°$. However, it should be stressed here, that sample imperfections leading to variations of physical properties at different locations along the measurement strip which is probed by the current could lead to similar effects. An unambiguous attribution of variations in $R_\text{res}(\varphi)$ to anisotropy proves to be difficult.
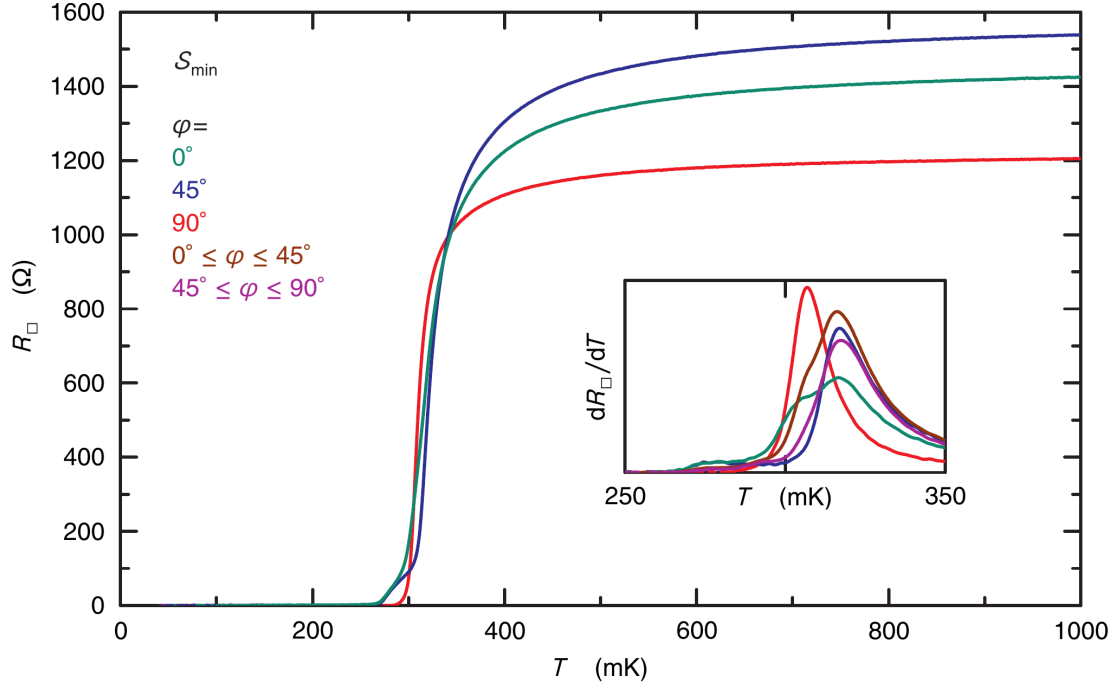
Figure 4.3: Sheet resistance $R_\square$ as function of temperature T at zero magnetic field applied for different current directions φ before illumination. Green color represents $\varphi = 0°$, blue color indicates $\varphi = 45°$ and red color $\varphi = 90°$ respectively. Temperature raised and lowered between $20\,\text{mK}$ and $1\,\text{K}$ during measurement. Inset shows $\mathrm{d}R_\square/\mathrm{d}T$ at the superconducting transition for temperatures between $250\,\text{mK}$ and $350\,\text{mK}$. Brown color indicates $0° \leq \varphi \leq 45°$ and magenta $45° \leq \varphi \leq 90°$ respectively.

$R_\square(T)$ drops to zero at low temperatures for all segments of $\mathcal{S}_{\min}$ clearly signaling superconductivity. It is instructive to plot the derivative $\mathrm{d}R/\mathrm{d}T$ alongside $R_\square(T)$ as demonstrated by the inset of Fig. 4.3. An ordinary superconducting transition would yield a single more or less sharp peak in the derivative. This is the case only for Segment $\varphi = 90°$, while the other two segments display fine structure at the transition. The largest peak for $\varphi = 45°$ is shifted to higher temperatures as compared to $\varphi = 90°$ but a tail of finite conductance stretches out to much lower temperatures. This tail is also visible at $\varphi = 0°$. In the latter measurements the major part of the peak splits in two with maxima at positions matching the peaks of $\varphi = 45°$ and $\varphi = 90°$, which are actually around $10\,\text{mK}$ apart. The inset shows also the derivative of two measurements on longer portions of the measurement strip, which force the current in different directions and probe a mixture of φ. Notably, the intermediate Segments $\varphi = 22.5°$ and $\varphi = 67.5°$ are probed as well. These measurements are in line with the single segment measurements, showing two peak positions at around $307\,\text{mK}$ and $317\,\text{mK}$ in agreement with the ones already observed. In summary, the measurements presented in Fig. 4.3, give evidence of two different superconducting constituents in $\mathcal{S}_{\min}$ with well separated transition temperatures.

Phenomenologically, different definition of the transition temperature are possible, which proves more or less useful depending on details of the measurement. The most elementary way chosen in the last chapter, *i.e.* calculating T_c from the relation $R_\square(T_c) = 0.5 \cdot R_{\text{res}}$ is a good starting point. However, it can easily lead to artifacts when T_c is studied as a function of a control parameter in inhomogeneous situations like the one found here. The relative height of the two peaks observed for most of the segments determines in a subtle way the temperature at which $R_\square$ is reduced by a factor of two. A more appropriate definition derives from the derivative by the relation $dR_\square(T_c)/dT = \max\{dR_\square(T)/dT\}$. It drags the determined value to the position of the higher peak and thus represents the T_c of the dominant constituent of the specific portion of S_{min}. Values derived from the measurement in Fig. 4.3 are given in Tab. 4.1.

Table 4.1: R_{res} and T_c for different φ before illumination for S_{min}.

φ in °	R_{res} in Ω	T_c in mK from $R(T_c) \equiv R_{\text{res}}/2$	T_c in mK from max. in $dR_\square/dT$
0	1422	322	317
45	1553	327	317
90	1202	311	307
$0° \leq \varphi \leq 45°$	-	323	316
$45° \leq \varphi \leq 90°$	-	326	318

Once more, it proves beneficial to display $R_\square(T)$ scaled by the residual resistance (see Fig. 4.4), which reveals that Segment $\varphi = 90°$ is outstanding while the other measurements share more features with one another. The superconducting transition of Segment $\varphi = 90°$ occurs entirely at the critical temperature of the lower constituent. The transition of all other segments is dominated by the constituent of higher T_c; the presence of the other constituent is visible, though, as a careful inspection of the fine structure at the transition reveals. So, Segment $\varphi = 90°$ in which current is forced perpendicular across the step edges of the terrace structure, is special. It is reasonable to assume, that the increased T_c dominating the transition for all other current directions is caused by special properties of the terraces, which are only probed, if current is running along the step edges. This is excatly in line with the motivating premise of this chapter which is addressed further below by $S_{2°}$ and $S_{6°}$ with their increased step edge densities.
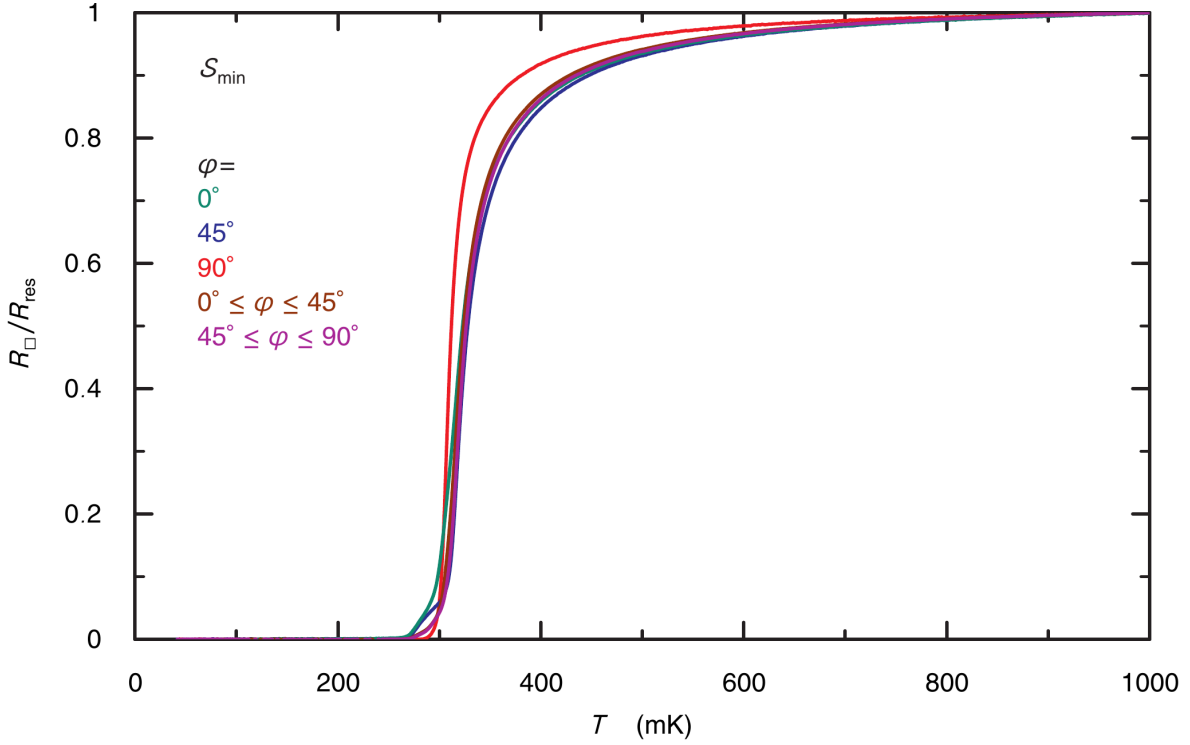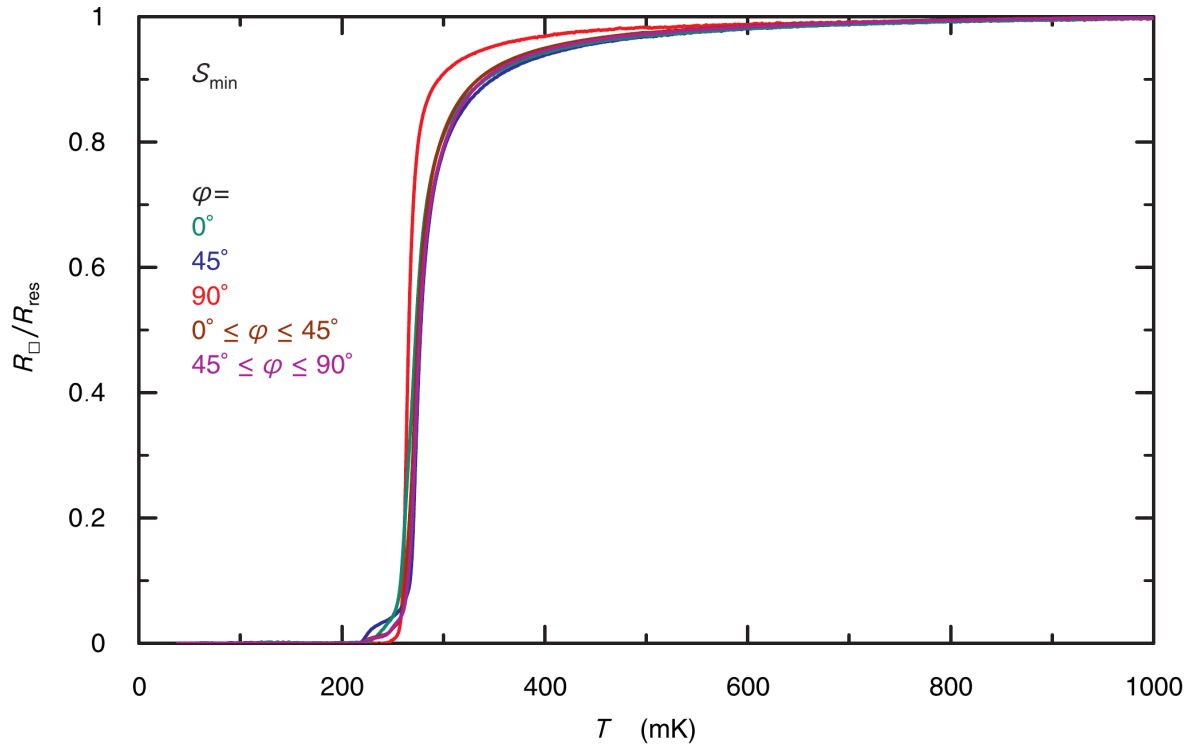
Figure 4.4: Scaled sheet resistance $R_\square/R_{res}$ as function of temperature T for all measured crystallographic directions before illumination. Green color represents $\varphi = 0°$, blue color indicates $\varphi = 45°$ and red color $\varphi = 90°$ respectively. Temperature raised and lowered between 20 mK and 1 K during measurement. Brown color indicates $0° \leq \varphi \leq 45°$ and magenta $45° \leq \varphi \leq 90°$ respectively.

The residual resistance of $\mathcal{S}_{min}$ can be reduced by illumination. Similar to the procedure exhaustively described in Ch. 3 for the LAO/STO sample, the illumination dose was applied in several steps leading to a series of states, which were all extensively characterized before the next state was approached. As in the case of LAO/STO the dose required for a certain resistance change increases with every step and the total change which can be achieved is limited. The AO/STO system seems to be more restricted than LAO/STO heterostructures. For the latter a factor of five reduction of R_{res} is demonstrated in the last chapter. For $\mathcal{S}_{min}$ (and also for $\mathcal{S}_{2°}$, and $\mathcal{S}_{6°}$) no further change could be achieved within a reasonable time of illumination after R_{res} is halved.

Figures 4.5 and 4.6 show $R_\square(T)$ and its derivative with respect to T in the state of minimal resistance. The magnitude of R_{res} is collected in Tab. 4.2. The superconducting transition is shifted to lower temperatures by about 45 mK with respect to the pristine state. The overall behavior, though, is quite similar: Segment $\varphi = 90°$ possesses a rather narrow transition with a maximal slope at around $T_c = 264$ mK and at lower temperature than the rest of the sample; this rest exhibits a fine structure in the transition visible most clearly in the derivative

as a second peak at around 272 mK and a low resistive tail extending about 40 mK below the main transition. T_c values extracted from the Figures are given in Tab. 4.2.

Table 4.2: R_{res} and T_c for different φ after illumination for S_{min}.

φ in °	R_{res} in Ω	T_c in mK from $R(T_c) \equiv R_{\text{res}}/2$	T_c in mK from max. in $dR_\square/dT$
0	774	273	272
45	837	277	273
90	641	266	264
$0° \leq \varphi \leq 45°$	-	275	272
$45° \leq \varphi \leq 90°$	-	277	272
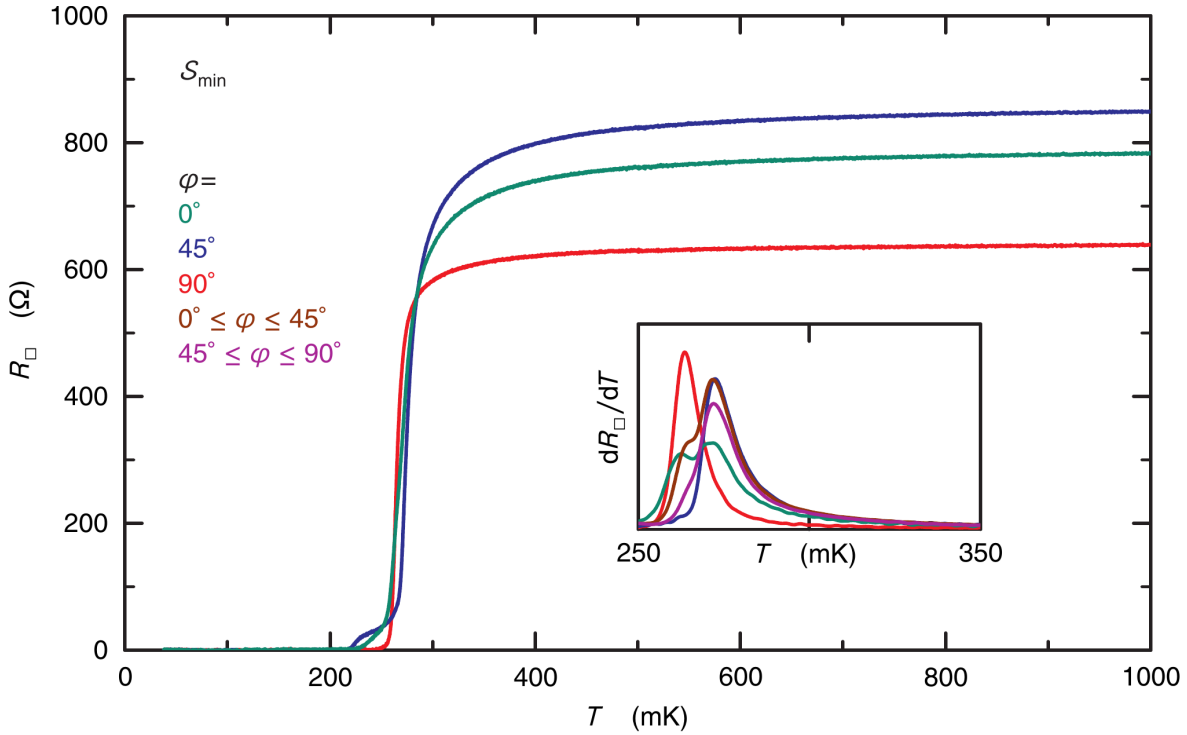
Figure 4.5: Sheet resistance $R_\square$ as function of temperature T at zero magnetic field for different crystallographic directions after illumination. Green color represents $\varphi = 0°$, blue color indicates $\varphi = 45°$ and red color $\varphi = 90°$ respectively. Temperature raised and lowered between 20 mK and 1 K during measurement. Inset display $dR_\square/dT$ for temperatures between 250 mK and 350 mK. Brown indicates $0° \leq \varphi \leq 45°$ and magenta $45° \leq \varphi \leq 90°$ respectively.

Figure 4.6: Scaled sheet resistance $R_\square/R_{res}$ as function of temperature for all measured crystallo-graphic directions after illumination. Green color represents $\varphi = 0°$, blue color indicates $\varphi = 45°$ and red color $\varphi = 90°$ respectively. Temperature raised and lowered between 20 mK and 1 K during measurement. Brown color indicates $0° \leq \varphi \leq 45°$ and magenta $45° \leq \varphi \leq 90°$ respectively.

4.2.1.2 $B_{crit}(T)$ measurements

Resistance is also recorded at constant temperature as a function of magnetic field B. From this measurements the critical field as function of temperature is extracted. Fig. 4.7 displays the sheet resistance $R_\square(B, T = \text{const.})$ of Segment $\varphi = 90°$ for various temperatures in the range $20\,\text{mK} < T < 400\,\text{mK}$ in the resistive state before illumination. Superconductivity is completely suppressed by a field $B > 0.4\,\text{T}$. Data for other segments and in other resistive states look quite similar and are not shown. By relating $R_\square(B_{crit}, T) = 0.5 \cdot R_\square(B = 0.4\,\text{T}, T)$ a critical field measure B_{crit} is given, which is used to characterize the sensitivity of superconductivity to B and to compare the sensitivity of different segments in different resistive states.
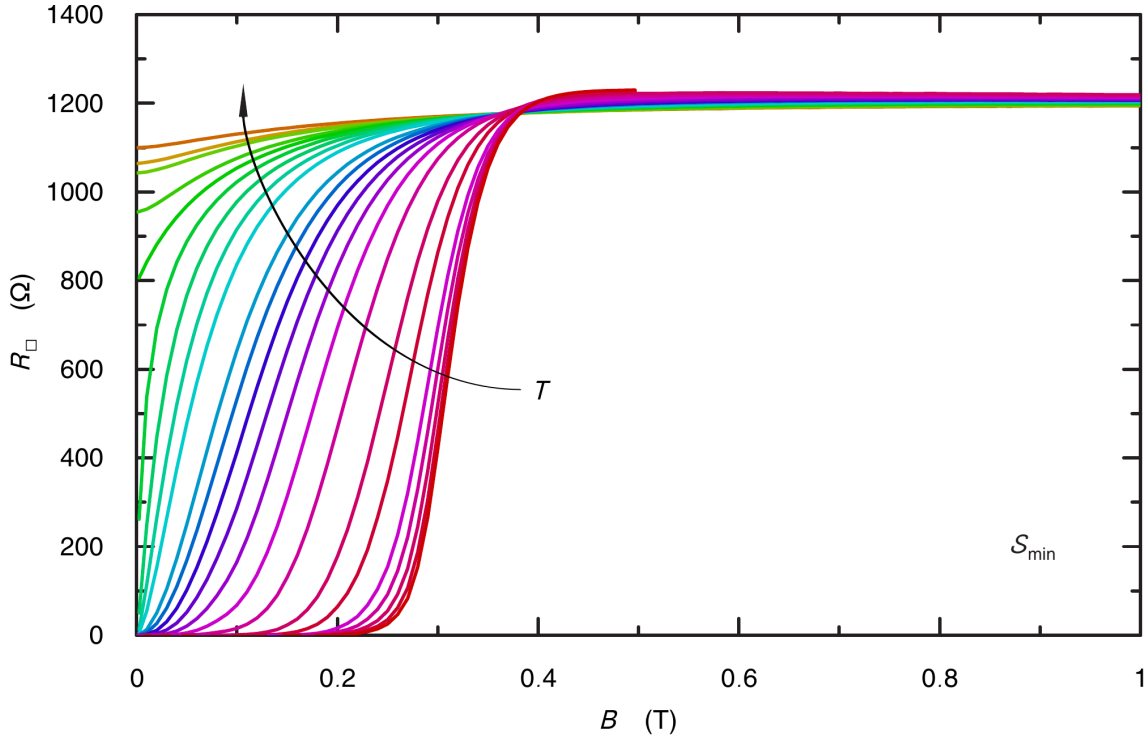
Figure 4.7: Sheet resistance $R_\square$ as function of applied magnetic field B for $\varphi = 90°$ at different temperatures indicated by different colors with a varying step width between $20\,\text{mK}$ and $450\,\text{mK}$ (specific description in text).

The result for S_{min} is summarized in Fig. 4.8, where B_{crit} is displayed as a function of T for various Segments in the pristine state prior to illumination (closed symbols) and after illumination in the final state of minimal residual resistance (open symbols). In all cases, $B_{crit}(T)$ is found to be a monotonically falling function of T which vanishes above a certain temperature threshold and has a tendency of saturation below $T \lesssim 40\,\text{mK}$. The data of Fig. 4.7 are represented by the closed red points. In this case, $i.\,e.$ for Segment $\varphi = 0$, B_{crit} goes to zero at $T \gtrsim 300\,\text{mK}$ and levels off to $B_{crit}(T \to 0) \sim 310\,\text{mT}$. The other two

segments as well as those encompassing $\varphi = 22.5°$ and $\varphi = 67.5°$ possess significant higher B_{crit} values. They collectively level off at $B_{\mathrm{crit}} = 340 \pm 10\,\mathrm{mT}$ for $T \to 0$ and vanish for $T \gtrsim 320\,\mathrm{mK}$. Notably, Segments $\varphi = 0°$ and $\varphi = 45°$, show comparable values over the whole temperature range, while the mixing of different current directions seem to lead to a slight reduction of B_{crit} in an intermediate temperature range. Together with R_{res} (and T_c as shown in Sec. 4.2.1.1) B_{crit} is reduced under the influence of illumination. $B_{\mathrm{crit}}(T)$ is still smallest for Segment $\varphi = 90°$, but the difference—especially for the low temperature saturation value—to other portions of the current path is reduced considerably.
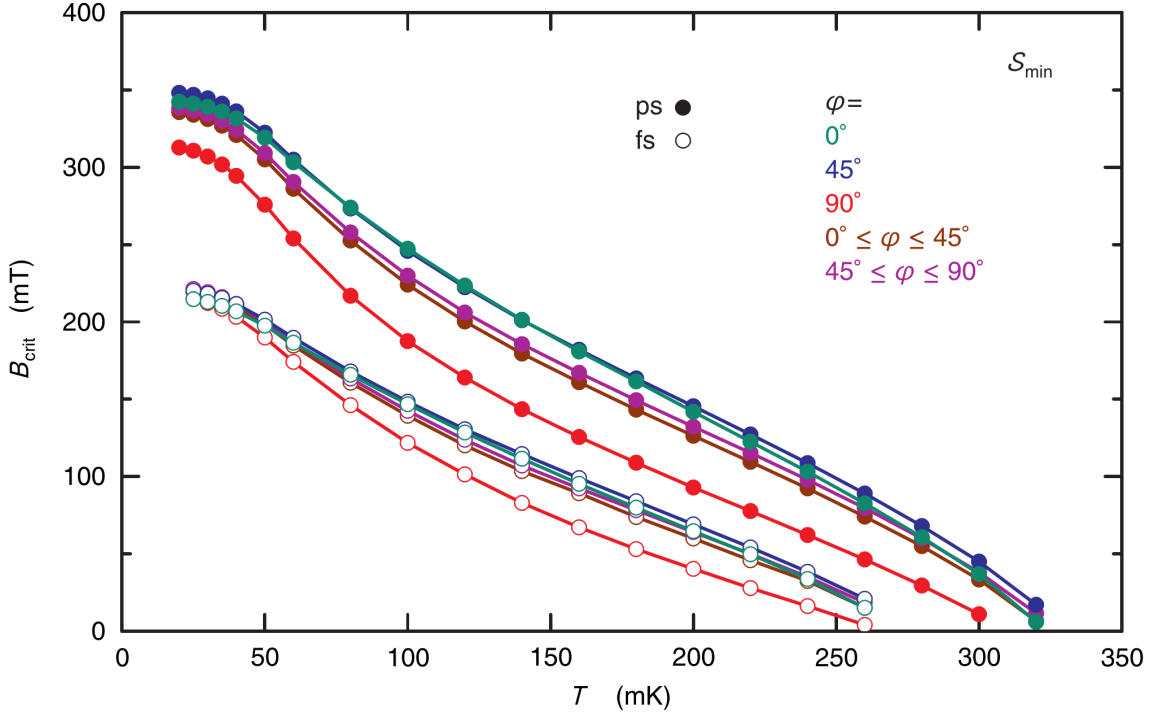
Figure 4.8: Critical field B_{crit} as function of temperature T before and after illumination. Green color represents $\varphi = 0°$, blue color indicates $\varphi = 45°$ and red color $\varphi = 90°$ respectively. Brown color indicates $0° \leq \varphi \leq 45°$ and magenta $45° \leq \varphi \leq 90°$ respectively. Closed circles indicate pristine state (before illumination), open circles represents data collected after illumination in the final state. Lines are guides to the eye.

In Ch. 2 it was discussed how B_{crit} relates to the superconducting coherence length ξ (see Eq. 2.6). Together with the saturation values suggested by Fig. 4.8 this yields values tabulated in Tab. 4.3.

Table 4.3: Superconducting coherence length extracted from B_{crit} saturation values at low temperature for S_{min} in its pristine state (before illumination) and in the final state after extended illumination.

φ	pristine state		final state	
	B_{crit} (mT)	ξ (nm)	B_{crit} (mT)	ξ (nm)
0°	345	31.1	212	39.2
45°	350	30.8	220	38.7
90°	310	32.4	212	39.2

4.2.1.3   Magneto-transport

Magneto-transport, *i. e.* $R_{xx}(B)$ and $R_{xy}(B)$, has been recorded at elevated $T \gg T_c$ as well, mainly to check for consistency with measurements performed earlier by K. Wolff as part of his PHD project (Wolff 2018; Wolff *et al.* 2020) on the identical samples. Between his measurements and the experiments described here, the samples were stored in vacuum at room temperature for several weeks and it was important to check for aging resistance. Indeed, results on $R_{xx}(B)$ and $R_{xy}(B)$ are well comparable. A comprehensive analysis of magneto-transport is already given in Wolff 2018; Wolff *et al.* 2020 and no further elaboration is of use here. As pointed out in Ch. 2 and Sec. 3.4 a detailed analysis of magneto transport is a formidable task, which even in semi-classical treatment requires a minute knowledge of the Fermi surface. In most cases one has to resort to simplifying models which make an analytical treatment feasible. This course has been pursued successfully in Wolff 2018; Wolff *et al.* 2020.

In this chapter only the Hall resistance $R_{xy}(B)$ is briefly discussed. R_{xy} is shown for the various segments of S_{min} in Fig. 4.9 in the pristine state before (solid lines) and after illumination (broken lines with brighter colors compared to pristine state representation). Obviously, before illumination $R_{xy}(B)$ follows a linear relation with a approximate Hall coefficient of $R_H = -27 \pm 2\,\Omega/T$. This corresponds to a charge carrier concentration of $n = 1/(eR_H) = (2.3 \pm 0.2) \cdot 10^{13}\,cm^{-2}$ on the basis of the most elementary treatment. In the final state a trend to a non-linear behavior of R_{xy} is visible. The Hall coefficient is slightly decreased.
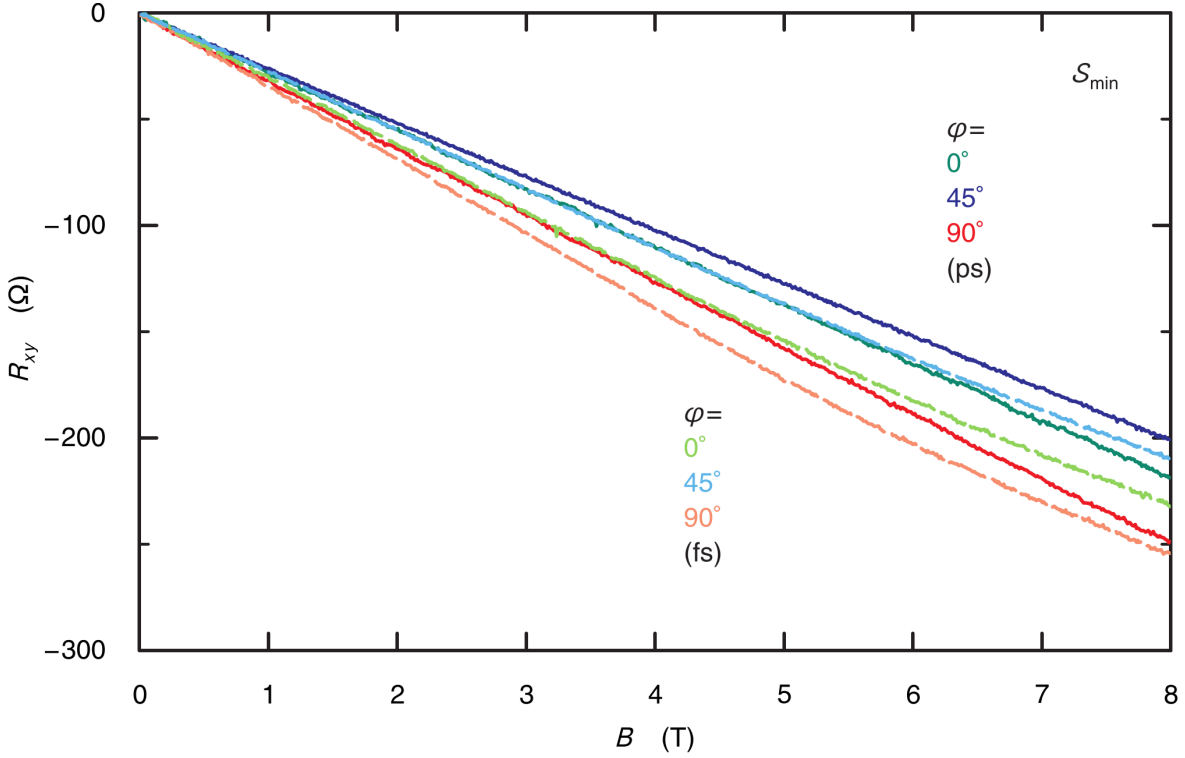
Figure 4.9: R_{xy} as function of magnetic field B at $1\,\mathrm{K}$ for different segments before and after illumination. Green color represents $\varphi = 0°$, blue color indicates $\varphi = 45°$ and red color $\varphi = 90°$ respectively. Pristine state (ps) before illumination represented by solid lines, final state (fs) after illumination indicated by broken lines with brighter coloring.

4.2.1.4 *I/U* characteristics

I/U characteristics as a function of temperature have been recorded. Characteristic curves at very low temperatures do not depend on temperature anymore. We find a hysteretical behavior with switching at a critical current I_c and a retrapping at a lower current I_r. Actually, both quantities are difficult to interpret without knowledge of the mechanism leading to a finite resistance upon rising current. The result on the LAO/STO sample presented in Ch. 3 suggests that the magnitude of I_c depends on some internal mesoscopic structure of yet unresolved nature which could be changed upon light induced resistance reduction. The whole structure is most likely a complicated network of weak-links. Having just seen that the present sample is constituted from components possessing at least two different transition temperatures (and accordingly different gap energies) makes it probable that I_c originates from a complicated internal weak-link structure for $\mathcal{S}_{\min}$, too.

The magnitude of I_r depends in addition on self heating effects. Dissipation in the resistive state leads to self heating and the effective temperature of the 2DES after switching is essentially unknown. The effective temperature drops of course upon lowering the cur-

rent. Retrapping is, on the basis of this simple reasoning, a result of decreasing temperature $T = T_{eff}(I)$ on the one hand, and an increasing critical current $I_c = I_c(T_{eff})$ on the other.
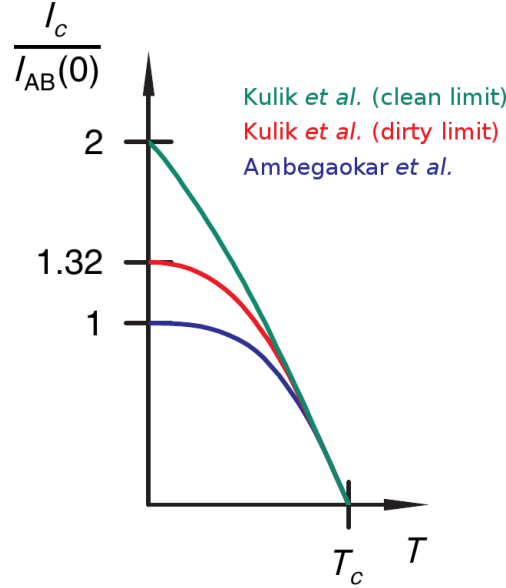
Figure 4.10: Sketch of the critical current as a function of temperature according to Ambegaokar *et al.* 1963 (blue), Kulik *et al.* 1975 (red, dirty limit), and Kulik *et al.* 1977 (green, clean limit). Figure adopted from Likharev 1979

As stated, it is reasonable to assume that I_c results from a mesoscopic network of weak-links in a yet unresolved fashion. A modeling of this situation is far beyond the scope of the present work. Still, one might guess that I_c depends strongly on the weakest link in the current path and that $I_c(T)$ resembles general properties of weak-link physics. In Fig. 4.10 the simple result of Ambegaokar *et al.* 1963

$$I_c R_n = \frac{\pi \Delta}{2e} \tanh \left(\frac{\Delta}{2 k_B T} \right) \tag{4.1}$$

as well as the more elaborated theory of Kulik *et al.* 1975; Kulik *et al.* 1977 is sketched and displays what to expect on the basis of this oversimplifying reasoning (R_n is the resistance of the non-superconducting state). Especially for $T \to 0$ Fig. 4.10 states that the so called $I_c R_n$ product of the dominating link is expected in the range $0.66 \pi \Delta / e \lesssim I_c R_n \lesssim \pi \Delta / e$.

In contrast to the observations in the LAO/STO sample which gave an optimistic picture that switching and retrapping behavior sheds some light on the internal structure of the underlying weak-link network, in the present case very little changes upon illumination are detected. In particular, I/U characteristics do not show the pronounced subgap features with an intermediate slope and no cascading switching (compare Sec. 3.3). The hysteretical behavior is in comparison rather simple; both I_c and I_r scale in a correlated manner with R_{res} upon illumination essentially as expected. A closer look at the retrapping behavior, however,

gives some hint that we are dealing with a kind of purification process when illumination changes the resistance in a persistent way. This is quite similar to the situation set out in the discussion of the LAO/STO characteristics.

First the results on the switching behavior will be summarized in this subsection. Later, I/U characteristics recorded in the vicinity of T_c will be reported, where BKT like features are prominent.

Characteristic curves at $100\,\text{mK}$ Figure 4.11 shows the I/U characteristics at $100\,\text{mK}$ for the three directions of φ before and after illumination. All segments are in a superconducting state for $I < 200\,\text{nA}$. Upon increasing the current switching at a critical magnitude I_c is observed. At higher currents the I/U characteristics follow a normal state branch. Upon lowering the current a hysteretical behavior is found with a retrapping at $I = I_r$. In the retrapping process several subgap states get apparent, which are revealed by a cascading series of small steps. In Tab. 4.4 data for I_c, I_r and for the Number N of jumps counted in the retrapping process are collected. Notably, switching occurs for all segments at the identical current, while the retrapping process allows for a slight scatter between different segments. In two out of the three segments the number of steps in the retrapping process is significantly reduced. The resistance $R_n^{\text{eff.}}$ of a hypothetical weak-link can be calculated from the above introduced $I_c R_n$ product using a BCS relation and the experimental values found in this section by the formula:

$$R_n^{\text{eff.}} = 1.764 a \frac{\pi k_B}{e} \cdot \frac{T_c}{I_c}, \tag{4.2}$$

where the factor a is in the range $0.66 < a < 1$ depending on details of the mean free path in the 2DES. Taking for the sake of definiteness the clean limit, Eq. 4.2 gives $R_n^{\text{eff.}} = 205 \pm 4\,\Omega$, which is actually a reasonable magnitude if compared to R_{res}. Notably, $R_n^{\text{eff.}}$ does not change within the experimental resolution upon illumination.
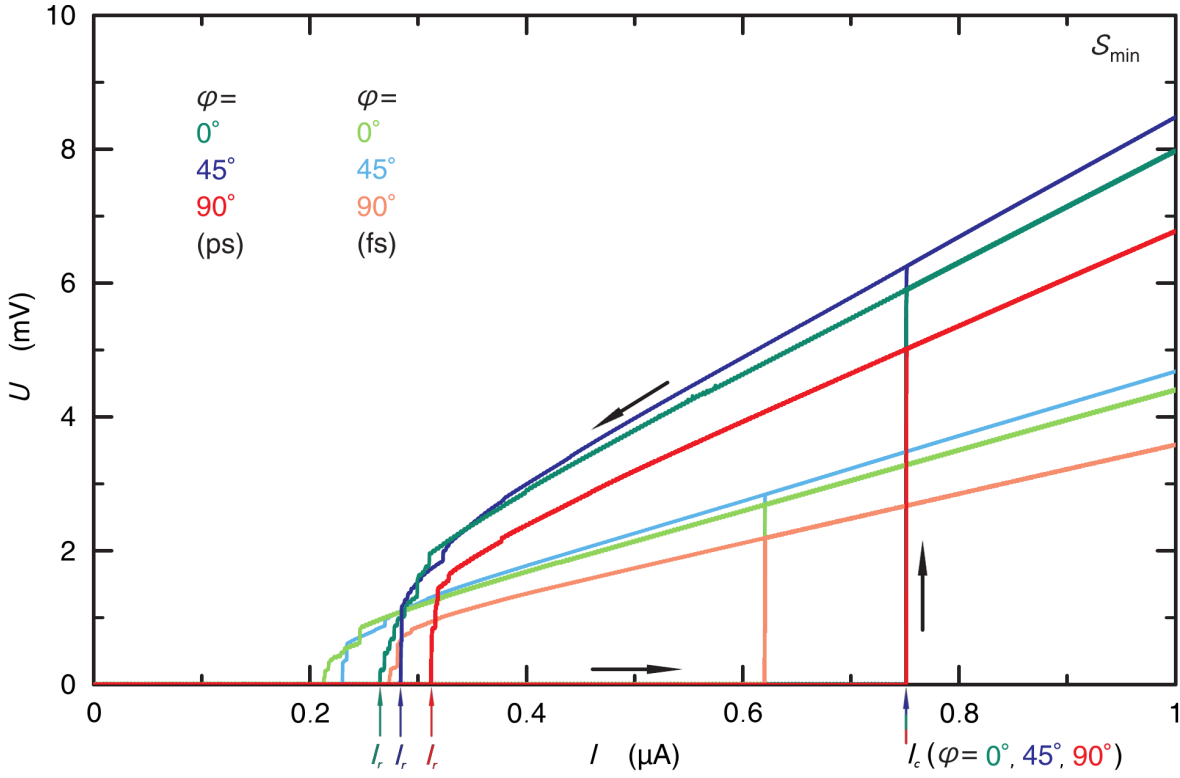
Figure 4.11: I/U characteristics at $100\,\mathrm{mK}$ before illumination in the pristine state (ps) and after influence of light in the final state (fs) without applied magnetic field. Green color represents $\varphi = 0°$, blue color indicates $\varphi = 45°$ and red color $\varphi = 90°$ respectively. Black arrows show the direction for dU/dt, while colored arrows indicate I_c and I_r for the respective direction of φ before illumination. Brighter coloring indicate final state (fs) after extended illumination.

Table 4.4: Current direction φ, Critical current I_c, retrapping current I_r and number of steps N before illumination (pristine state) and after illumination (final state) for S_{min}.

φ	pristine state			final state		
	I_c (nA)	I_r (nA)	N	I_c (nA)	I_r (nA)	N
0°	753.1	263.7	6	621.7	213.5	4
45°	751.9	282.4	3	621.5	229.5	3
90°	751.7	309.5	9	621.4	272.8	3

Characteristic curves as function of T Figure 4.12 shows I_c (left panel) and I_r (right panel) as a function of temperature at $B = 0$. Closed and open symbols belong to the pristine state of maximal R_{res} and the final state of minimal R_{res}, respectively. The behavior

of I_r will not be discussed further; as mentioned above it is expected to depend on details of self heating. It thus does not come as a surprise, that it varies as a function of the segment probed, and goes down together with R_{res}.

More interesting is the behavior of I_c In the temperature range $T < 200 \ldots 250\,\text{mK}$ it does not depend on the probed segment and can most likely be described by a model derived from Fig. 4.10. The collective switching of all segments at the same temperature further supports the hypothesis of a dominating weak-link. Wherever this link is located, if it is going normal conducting, self heating leads to a hot spot in its vicinity which rapidly spreads out and destroys superconductivity along the entire current path.
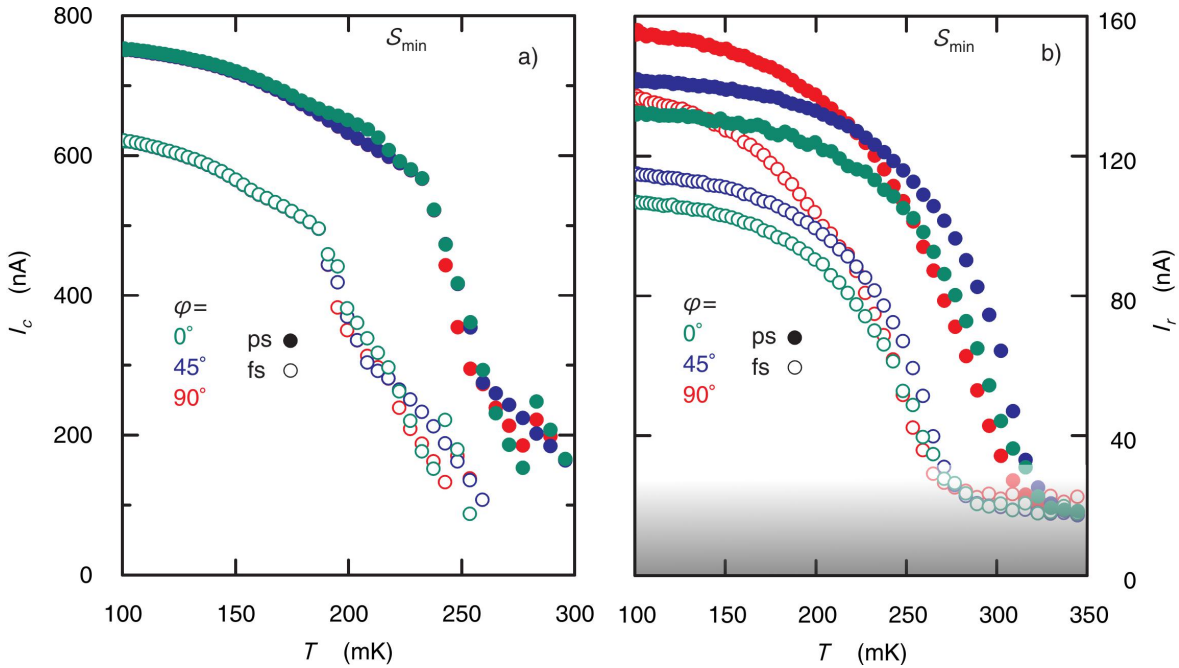
Figure 4.12: I_c (a) and I_r (b) as function of T for different φ before and after illumination without applied magnetic field. Green color represents $\varphi = 0°$, blue color indicates $\varphi = 45°$ and red color $\varphi = 90°$ respectively. Closed circles indicate pristine state (before illumination), open circles represents data collected after illumination in the final state. Due to switching between resistive and superconducting phase occur at same currents, the data points are superimposed at low temperatures and only green data points are visible. Noise floor indicated by shadow

At low temperatures $U(I)$ stays below the detection limit of finite voltage—set by the noise level of the preamplifiers—for all currents $|I| < I_c$ (see Fig. 4.12). This changes if the temperature is elevated to about 50 mK below the transition temperature as demonstrated in the left panel of Fig. 4.13 which displays I/U characteristic curves in the temperature range $215\,\text{mK} < T < 270\,\text{mK}$ for Segment $\varphi = 90°$. A cutout in the range of small currents and voltages is shown on a linear (left) and double logarithmic (right) scale. Up

to $T \leq 240\,\text{mK}$ a hysteretical behavior with switching and retrapping is obsereved together with a clearly dissipative transport even below the retrapping current. Above $T > 240\,\text{mK}$, no more switching is detected and an ohmic $U(I)$ dependence is quickly approached at higher T. The log-log plot on the right reveals that the voltage response at small currents is well approximated by a power law $U \propto I^\alpha$ with a temperature dependent exponent $\alpha = \alpha(T)$.
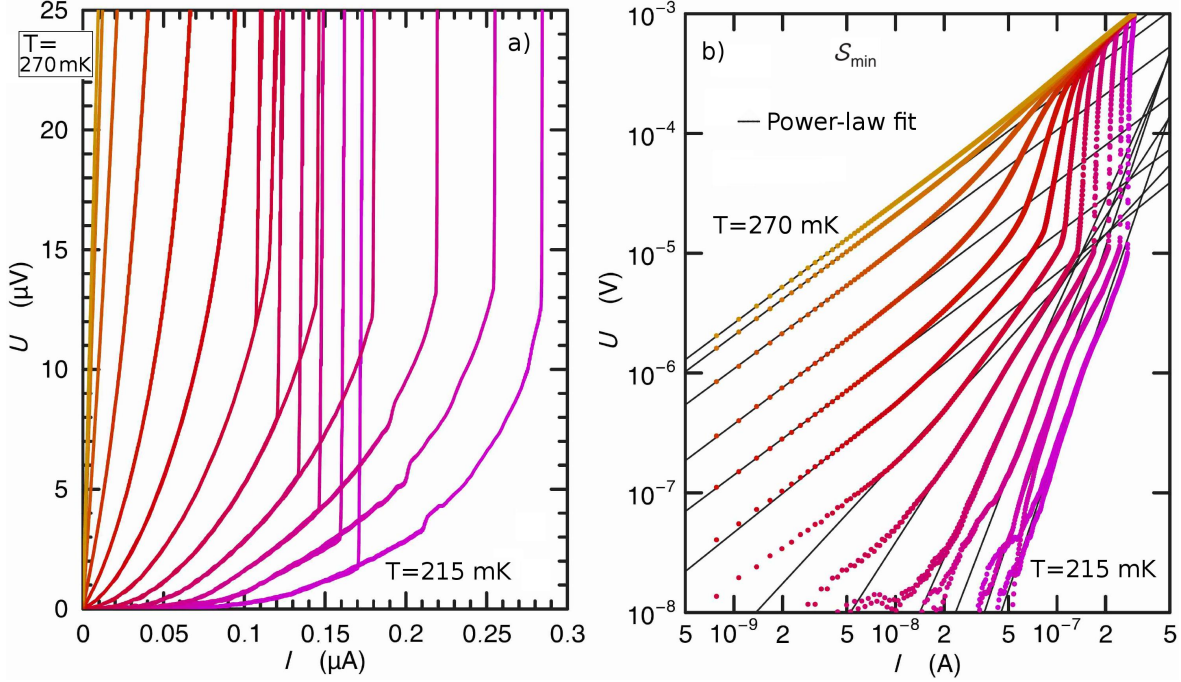

Figure 4.13: I/U characteristics close to the BKT transition. The left panel display the characteristic curves on a linear scale. The right panel presents the same data on a double logarithmic scale together with power-law fits $U \propto I^\alpha$. Different curves are recorded in the final state with minimal R_{res} at different temperatures. Shown are curves from $T = 215\,\text{mK}$ to $T = 270\,\text{mK}$ spaced 5 mK apart.

The behavior described here is the hall mark of a Berezinkiǐ-Kosterlitz-Thouless (BKT) transition (see Sec. 2.2.2). The transition temperature is defined by the relation $\alpha(T_{\text{BKT}}) = 3$. Fig. 4.14 (a) presents α as a function of temperature for the three segments of $\mathcal{S}_{\text{min}}$ in the final state of minimal R_{res}. All points have been extracted from least square fitting a power law to a I/U characteristic curve as exemplified in the right panel of Fig. 4.13. In the fitting procedure the range of validity of the power law was adjusted by hand. $T_{BKT} = 215 \pm 5\,\text{mK}$ for all segments of $\mathcal{S}_{\text{min}}$. Fig. 4.14 b) visualize the results for the pristine state, which possess qualitatively a similar behavior with a higher T_{BKT}, although it proved to be more difficult to analyze the characteristics.
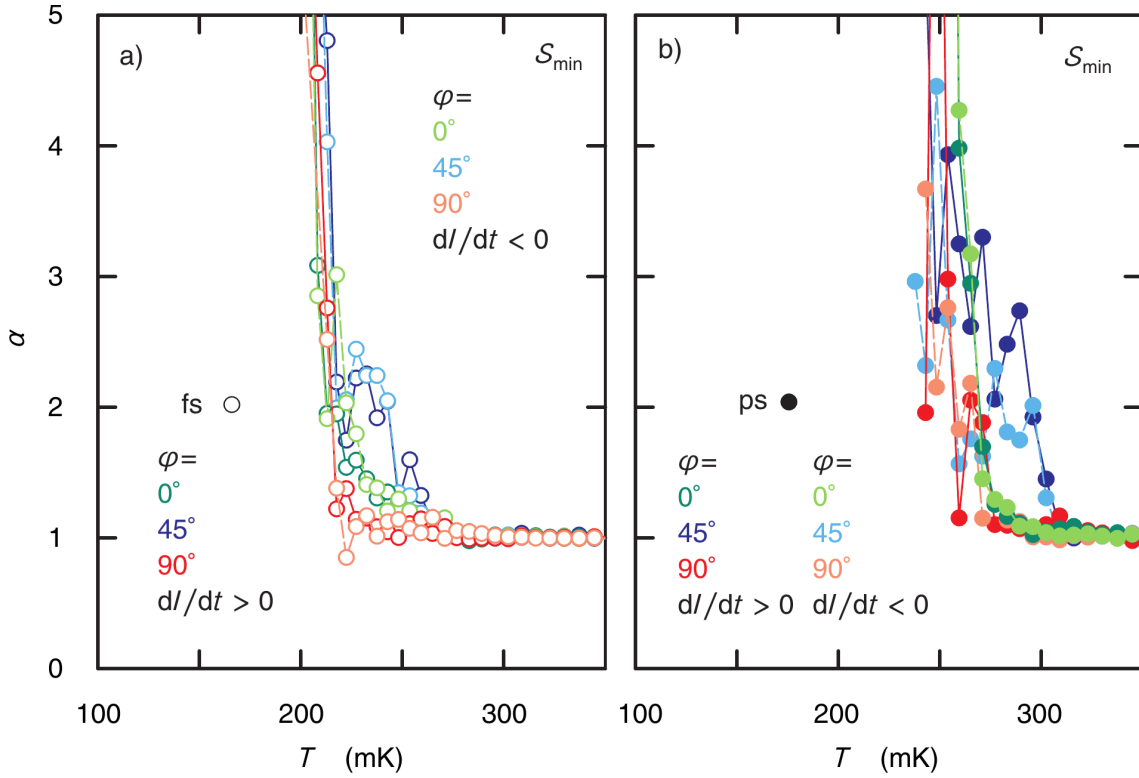
Figure 4.14: Exponent α in $U \propto I^{\alpha}$ as function of temperature determined by least square fitting to the I/U characteristics. a) Final state (fs) with minimal R_{res} and b) pristine state (ps) with maximal R_{res}. Colors as usual: Segment $\varphi = 0°$ (green), $\varphi = 45°$ (blue), and $\varphi = 90°$ (red).

4.2.2   Sample $\mathcal{S}_{2°}$: $\gamma = 2°$

The substrate of the second sample $\mathcal{S}_{2°}$ in this study has a nominal tilt of $\gamma = 2°$ with respect to an ideal (001) crystallographic orientation. A detailed analysis of an AFM micrograph (see discussion of Fig. 4.1 b) estimates the mean width of the terraces to be $w \approx 37$ nm. This is considerably larger than what one would expect by equating $w = \tan(2°)/a \approx 11$ nm, where a is the lattice constant of STO. The increase of w results from bunching of several STO layers at the step edges and indeed a mean step height of $h = 3.6a$ is found experimentally. This is actually a positive result; the purpose of the intentionally applied tilt was to strengthen the scattering of charge carriers at terrace edges and both, the reduction of w (by about 70 %) and the increment of h (by 360 %) is in favor of this.
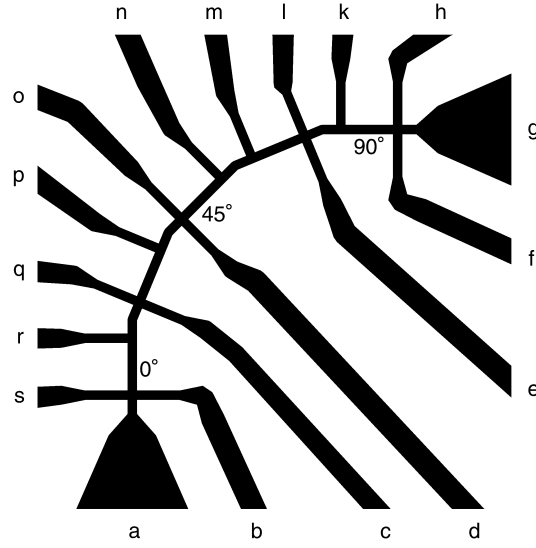
Figure 4.15: A schematic representation of $S_{2°}$. Measurements are performed on the segments la-
beled by values in degrees. Step edges are aligned perpendicular with respect to the
terraces of $S_{\min}$ (see Fig. 4.1 b).

All contacts needed for a proper connection for R_{xx} and R_{xy} measurements (*i. e.* $\{a, g\}$
for the current bias, $\{f, h, k\}$ for Segment $\varphi = 0°$, $\{d, n, o\}$ for Segment $\varphi = 45°$, and $\{b, r, s\}$
for Segment $\varphi = 90°$) did have appropriate contact resistances at low temperature.

4.2.2.1   Superconducting transition temperature

In Fig. 4.16 measurements of $R_\square(T)$ are presented for three Segments in the pristine
state of $S_{2°}$ prior to illumination. Values for $R_{\mathrm{res}} \equiv R_\square(T = 1000\,\mathrm{mK})$ and T_c are given in
Tab. 4.5. R_{res} varies more strongly with φ by 40 % (compared to 23 % in $S_{\min}$) and approach
a maximal and minimal magnitude for Segments $\varphi = 90°$ and $\varphi = 0°$, respectively. So,
as intended, the main axes of the resistance tensor are aligned with the terrace structure in
contrast to the findings in $S_{\min}$, where anisotropy was dominated by dislocation lines. R_{res}
is maximized when current is forced in a perpendicular direction to the step edges, which
obviously lead to an increased scattering rate of the charge carriers as intended.

The superconducting transition is located at temperatures around $T \approx 250\,\mathrm{mK}$ and thus
considerable lower than in $S_{\min}$. It also has, as revealed most clearly by the derivative of $R_\square$
with respect to T shown in the inset, slightly different properties. For all segments we find a
single prominent peak, and only Segment $\varphi = 0°$ possess a resistive tail stretching out about
$20\,\mathrm{mK}$ below the main transition. T_c irrespective on whether defined by the half-height or the
steepest-crescent rule appears to be different for all segments. Segment $\varphi = 90°$ displays a
significant lower T_c than the other two segments, though, and the finding for $S_{\min}$ is verified:
T_c is enhanced if the current is allowed to flow alongside of terraces.

Table 4.5: R_{res} and T_c for different φ before illumination for S_{2°.

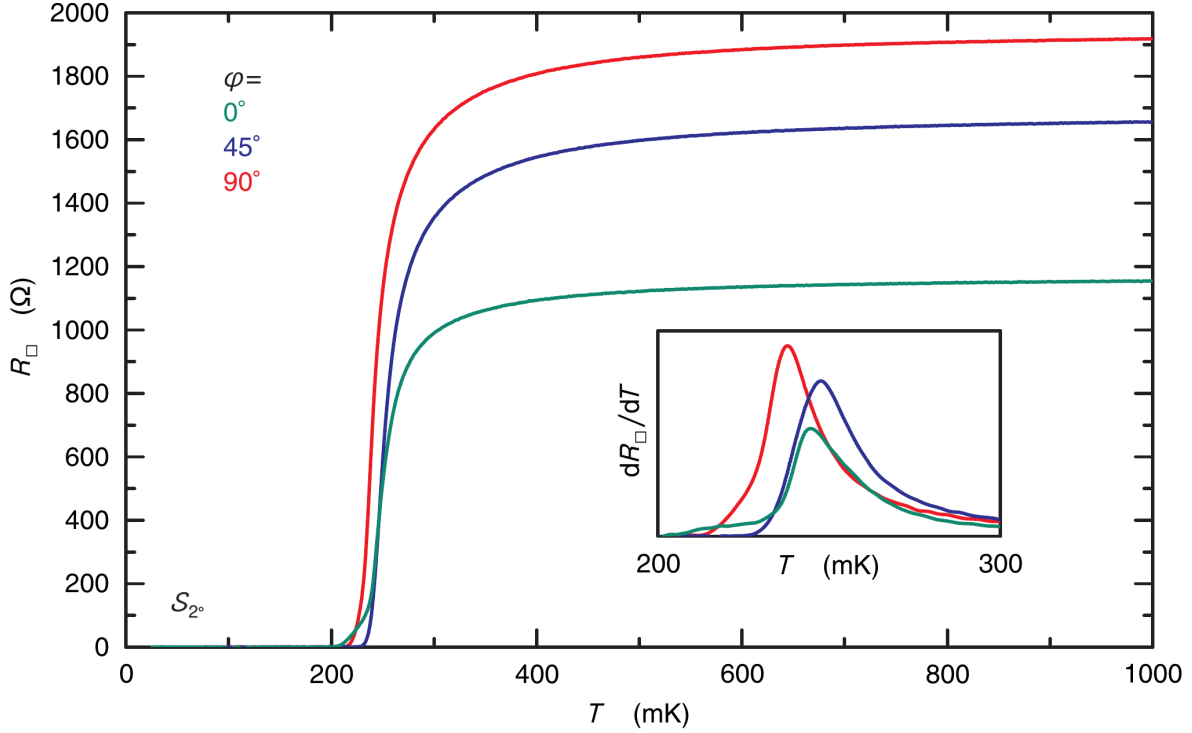| φ	R_{res} in Ω	T_c in mK from $R(T_c) \equiv R_{\text{res}}/2$	T_c in mK from max. in $dR_\square/dT$
0°	1154	252	245
45°	1656	256	248
90°	1918	245	238

Figure 4.16: Sheet resistance $R_\square$ as function of temperature T at $B = 0$ for different Segments ($\varphi = 0°$ (green), $\varphi = 45°$ (blue), and $\varphi = 90°$ (red)) in the pristine state before illumination. Measurements with $dT/dt > 0$ and $dT/dt < 0$ are shown on top of each other and are indistinguishable on the scale of the drawing. Inset shows $dR_\square/dT$ in the vicinity of the superconducting transition.

The resistance could again be lowered by illumination. Consistently with S_{min} a factor of two reduction could be achieved in the final state of a series of illumination cycles. The reduction of R_{res} is accompanied by the usual shift of the superconducting transition to lower temperatures. The result in the final state can be assessed in Fig. 4.17 and Tab. 4.6. The most remarkable feature of Fig. 4.17 is visible in $R_\square(T)$ of Segment $\varphi = 0°$. The transition is split in two halves appearing as two separate peaks in the derivative. A lower peak, which is at the same time broader is centered at about 230 mK. The higher peak is located exactly at position of the transition in Segment $\varphi = 90°$. Actually, Segment $\varphi = 0°$ of S_{2° reacts to illumination in a less predictable way than any other segment of the investigated samples.

This will get more apparent in Sec. 4.2.2.3.

Table 4.6: R_{res} and T_c for different φ after illumination for S_{2°.

φ in °	R_{res} in Ω	T_c in mK from $R(T_c) \equiv R_{\mathrm{res}}/2$	T_c in mK from max. in $dR_\square/dT$
0	567	216	197
45	918	206	202
90	1033	199	197
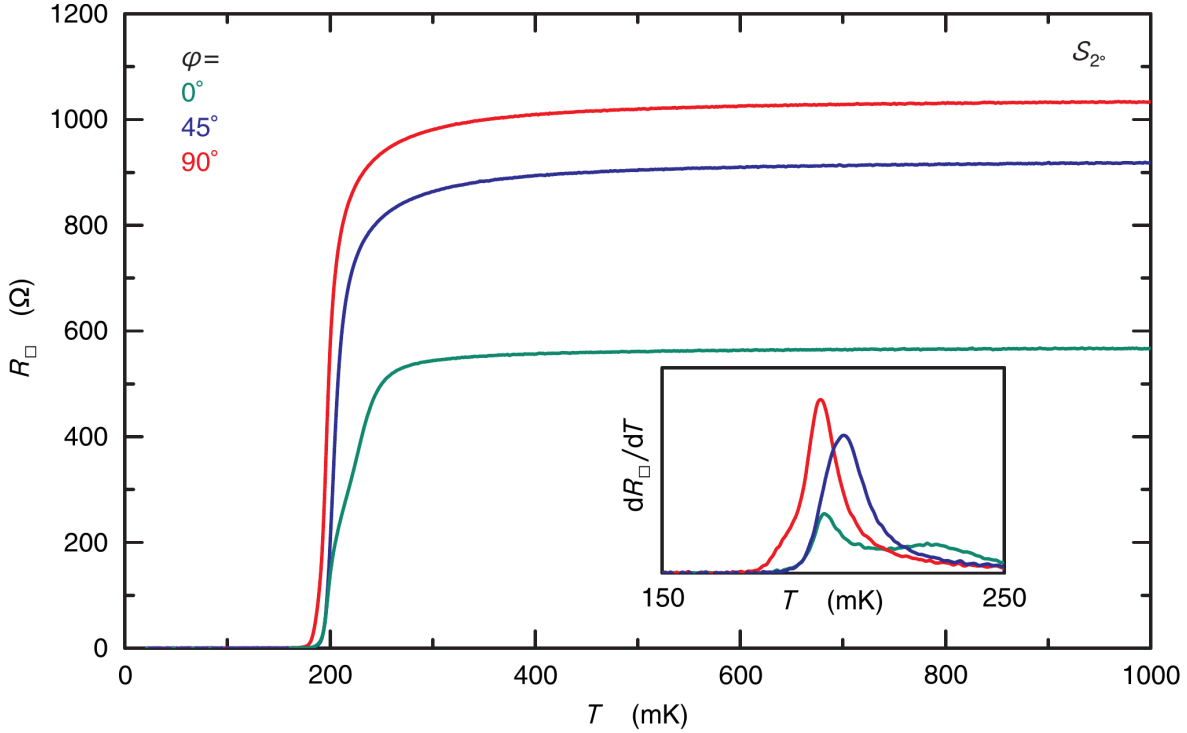
Figure 4.17: Sheet resistance $R_\square$ as function of temperature T at $B = 0$ for different Segments ($\varphi = 0°$ (green), $\varphi = 45°$ (blue), and $\varphi = 90°$ (red)) in the final state after long exposure. Measurements with $dT/dt > 0$ and $dT/dt < 0$ are shown on top of each other and are indistinguishable on the scale of the drawing. Inset shows $dR_\square/dT$ in the vicinity of the superconducting transition.

4.2.2.2 $B_{\mathrm{crit}}(T)$ measurements

Figure 4.18 shows the T dependence of B_{crit} as extracted from $R_\square(B, T = \mathrm{const.})$ measurements in the pristine and final state. A trend to a saturation of B_{crit} in the limit $T \to 0$ is visible below $T < 20\,\mathrm{mK}$. This saturation value and the coherence length derived by Eq. 2.6 is tabulated in Tab. 4.7.
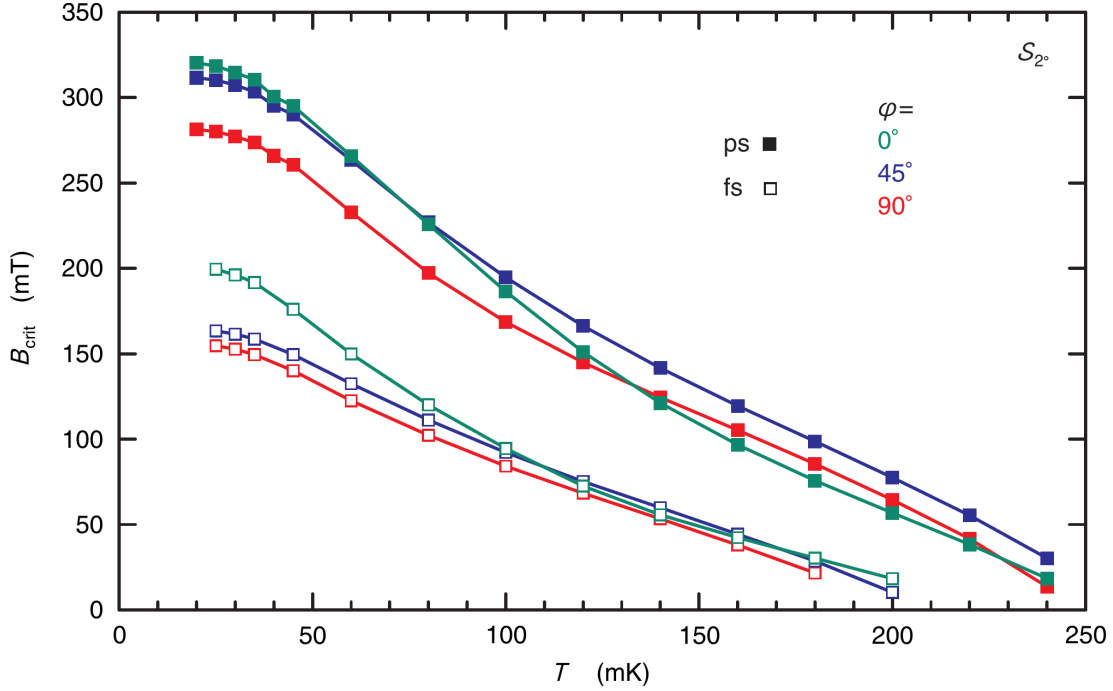
Figure 4.18: Critical field B_{crit} as function of temperature T before and after illumination. Green color represents $\varphi = 0°$, blue color indicates $\varphi = 45°$ and red color $\varphi = 90°$ respectively. Closed squares indicate pristine state (before illumination), open squares represents data collected after illumination in the final state. Lines are guides to the eye.

Table 4.7: Superconducting coherence length extracted from B_{crit} saturation values at low temperature for $S_{2°}$ in its pristine state and in the final state after extended illumination.

φ	pristine state		final state	
	B_{crit} (mT)	ξ (nm)	B_{crit} (mT)	ξ (nm)
0°	320	32.1	201	40.6
45°	312	32.5	155	44.9
90°	281	34.2	153	46.1

4.2.2.3 Magneto-transport

The Hall resistance R_{xy} at $T = 1\,K$ of $S_{2°}$ is visualized in Fig. 4.19 in the pristine and the final state as solid and broken lines, respectively. In the state of maximal R_{res} a linear behavior over the whole magnetic field range is observed for all Segments, *i.e.* with the definition $R_H \equiv dR_{xy}(B = 0)/dB$ the relation $R_{xy} = R_H B$ is fulfilled at least up to $|B| < 8\,T$. Obviously Segment $\varphi = 0°$ behaves different as compared to the other two segments. While $R_H \approx -22\,\Omega/T$ for the latter is well comparable to the Hall constants

Table 4.8: Hall constant $R_H = dR_{xy}(B = 0)/dB$ and corresponding charge carrier concentration $1/(eR_H)$ of $S_{2°}$ in the pristine and final state

	pristine state		final state	
φ	R_H (Ω/T)	$1/(eR_H)$ (10^{13}/cm^2)	R_H (Ω/T)	$1/(eR_H)$ (10^{13}/cm^2)
0°	-41.1	1.5	-47.4	1.3
45°	-21.7	2.9	-25.1	2.5
90°	-22.5	2.8	-27.6	2.3

observed in S_{min} and $S_{6°}$, $R_H \approx -41\Omega$/T has almost doubled in Segment $\varphi = 0°$ (see Tab. 4.8). If interpreted in the framework of a one-band Drude approximation, this would mean that the charge carrier concentration is dramatically lower in a single segment of $S_{2°}$.
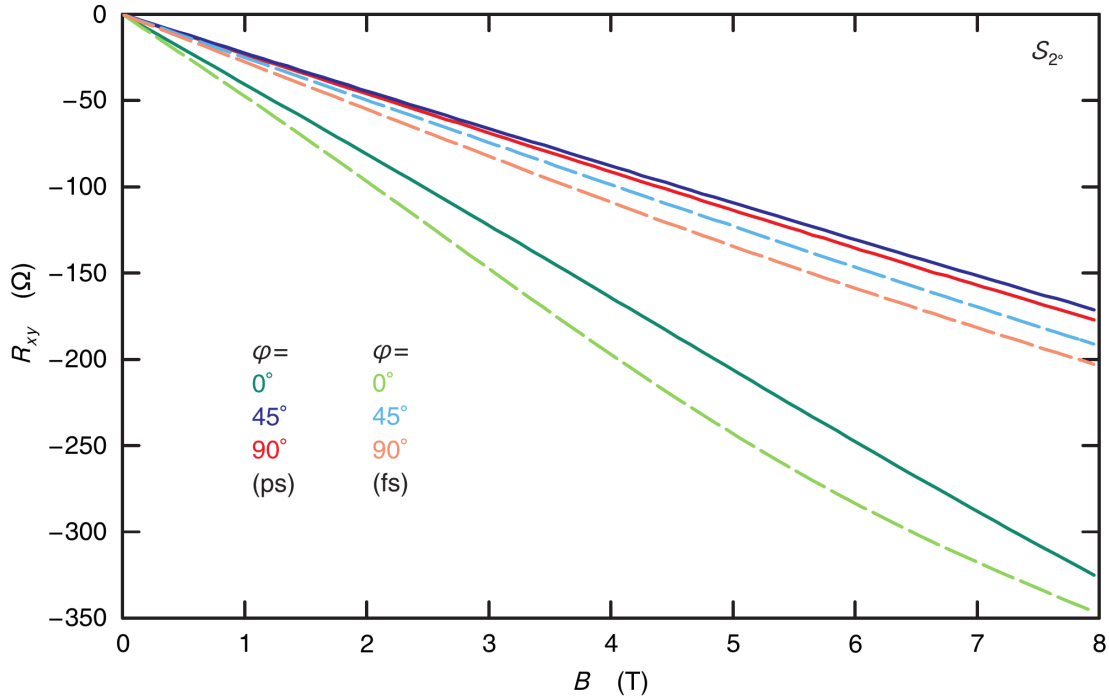
Figure 4.19: R_{xy} as function of magnetic field B at 1 K for different segments before and after illumination. Green color represents $\varphi = 0°$, blue color indicates $\varphi = 45°$ and red color $\varphi = 90°$ respectively. Pristine state (ps) before illumination represented by solid lines, final state (fs) after illumination indicated by broken lines with brighter coloring.

Upon illumination a slight increase of R_H is noted and the corresponding charge carrier concentration drops between 14 % and 18 %. Furthermore, the still much steeper Hall effect in Segment $\varphi = 0$ develops clearly a non-linear behavior at higher fields which unmistakably invalidate the quasi free electron approximation. This comes, as such, not as a surprise. A

non-linear contribution to R_{xy} has been shown already in the current thesis for the LAO/STO sample in Ch. 3.

4.2.2.4 I/U characteristics

Characteristic curves at $100\,\mathrm{mK}$ Figure 4.20 shows the I/U measurements at $T = 100\,\mathrm{mK}$ before and after illumination at $B = 0$. In the pristine state the segments of $S_{2°}$ have different I_c, in contrast to the findings in S_{min}. In the final state, though, I_c is identical for all segments. The lowest retrapping current is found in Segment $\varphi = 90°$, the highest in Segment $\varphi = 0°$. I_c, I_r, and N is tabulated in Tab. 4.9.
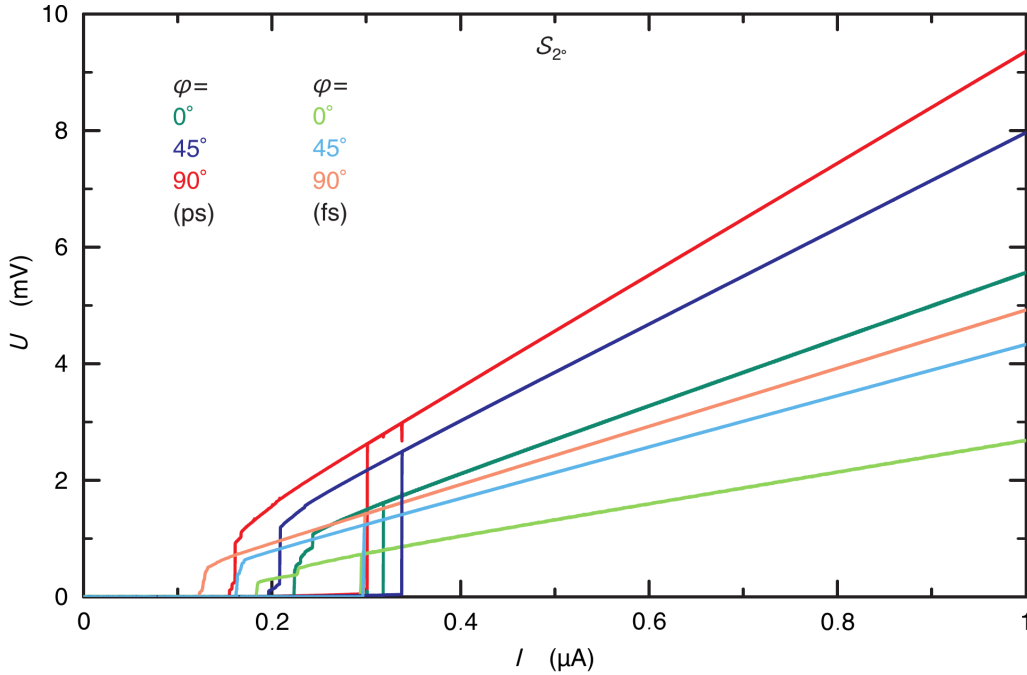
Figure 4.20: I/U characteristics at $100\,\mathrm{mK}$ before illumination in the pristine state (ps) and after influence of light in the final state (fs) without applied magnetic field. Green color represents $\varphi = 0°$, blue color indicates $\varphi = 45°$ and red color $\varphi = 90°$ respectively. Brighter coloring indicate final state after extended illumination.

Table 4.9: Current direction φ, Critical current I_c, retrapping current I_r and number of steps N in the pristine state before illumination of maximal R_{res} and in the final state of minimal R_{res} after illumination.

φ in °	I_c in nA (ps)	I_r in nA (ps)	N (fs)	I_c in nA (fs)	I_r in nA (fs)	N (fs)
0	319.4	221.8	4	294.5	184.0	3
45	339.3	195.7	3	297.2	162.5	3
90	301.6	154.2	2	297.7	124.7	3

Characteristic curves as function of T   During a measurement of I/U characteristics for $S_{2\circ}$ in its final state it was noticed that in this particular case I_c measured at base temperature is considerably larger than at $T = 100$ mK. The latter temperature is usually the lowest at which I/U characteristics have been studied since the apparent saturation of I_c in this temperature range suggested in the past, that recording at lower temperatures is superfluous. As mentioned before, the retrapping branch is anyhow determined by self-heating in the temperature range below $T < 100$ mK and does not depend on temperature anymore. I_c happens to be comparatively small for $S_{2\circ}$ at $T = 100$ mK (compare Fig. 4.21 to Figs. 4.12 and 4.29). In the final state at base temperate $T \lesssim 20$ mK, however, the typical magnitude of $I_c > 500$ nA is recovered. The temperature range of I/U characteristics was thus extended down to 50 mK for the final state of $S_{2\circ}$. Results for I_c are presented in Fig. 4.21. Indeed, the critical current I_c rises strongly below $T < 100$ mK. In this temperature range all segments of $S_{2\circ}$ share identical I_c. Different I_c (with respect to φ) occur at higher temperatures only. The overall behavior of I_c as a function of temperature in the final state display clearly at least three contributions which are strongly reminiscent of the generic behavior reported in the sketch of Fig. 4.10.
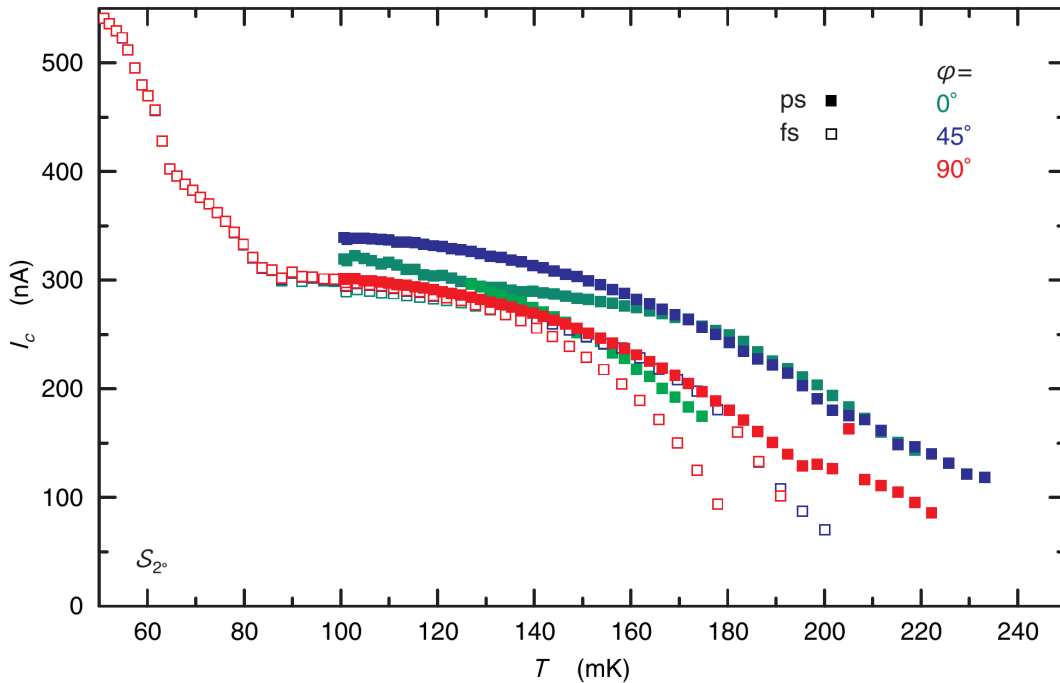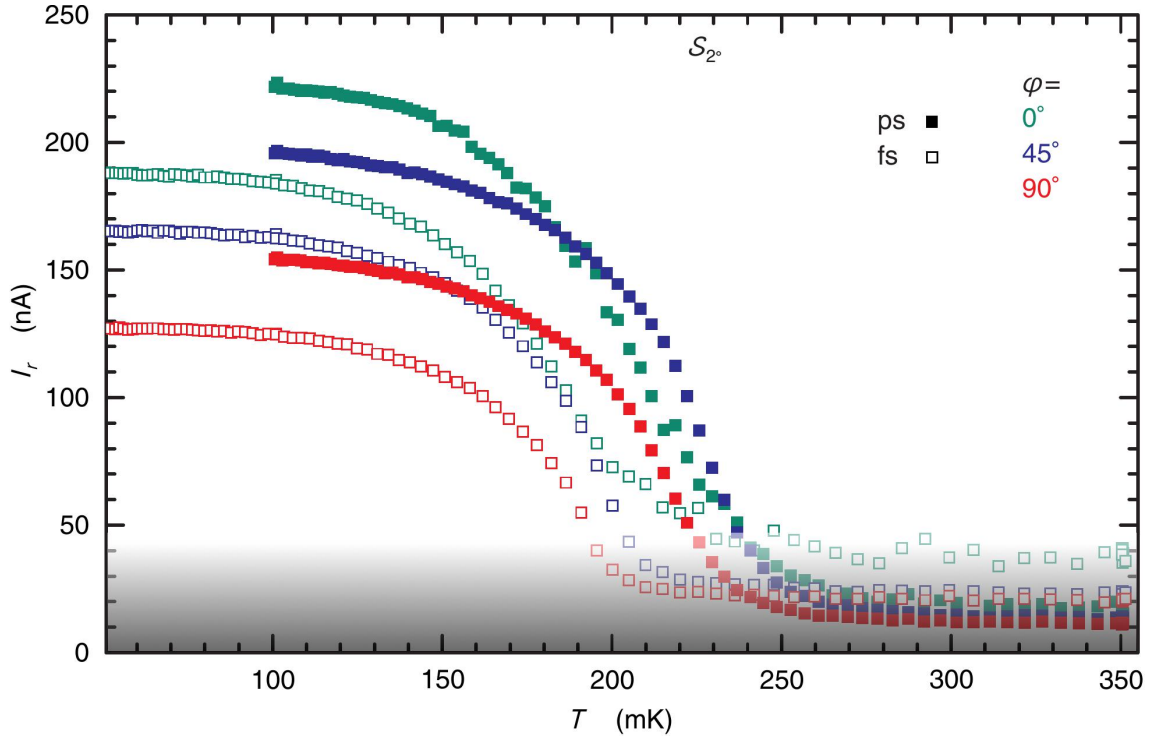

Figure 4.21: Critical current I_c in dependency of temperature T before and after illumination. Green color represents $\varphi = 0°$, blue color indicates $\varphi = 45°$ and red color $\varphi = 90°$ respectively. Closed squares indicate pristine state (ps) before illumination, open squares represents data collected after illumination in the final state (fs). Due to switching between resistive and superconducting phase occur at same currents, the data points at $T < 100$ mK are superimposed and only red data points are visible.

It is reasonable to conjecture the presence of several superconducting gaps acting concurrent. This is readily apparent in the final state of $S_{2°}$ as reported in Fig. 4.21. In the light of this evidence it is worthwhile to revisit Fig. 4.12 in which I_c vs. T is presented for $S_{\min}$. The kink around $T = 230\,\text{mK}$ and $T = 190\,\text{mK}$ in the pristine and final state, respectively, clearly discernible their can be tentatively attributed to the presence of two different gaps, too. Similar findings will be reported for $S_{6°}$. The conjecture of the presence of several gaps is consistence with the proposed model of a mesoscopic structure of varying physical properties. The variations are most likely caused by an inhomogeneous distributed dopant density.

In the pristine state of maximal R_{res}, the critical current I_c varies from segment to segment. Most notably, Segment $\varphi = 0°$, which showed unusual behavior in $R_{\square}(T)$ (see inset of Fig. 4.17) and Hall effect (see Fig. 4.19), too, is special for $140\,\text{mK} < T < 175\,\text{mK}$. Dissipation sets in at rising currents in form of two well separated switching points, I_{c1} and I_{c2} with an intermediate range of reduced resistance as compared to the normal state value. A similar behavior is reported in Ch. 2 for the LAO/STO sample. I_{c1} tend to align with the critical current of Segment $\varphi = 90°$, while I_{c2} approaches with rising temperature the critical current of Segment $\varphi = 45°$. This observation is further evidence of the underlying and hidden mesoscopic structure.

Figure 4.22: Retrapping current I_r in dependency of temperature T before and after illumination. Green color represents $\varphi = 0°$, blue color indicates $\varphi = 45°$ and red color $\varphi = 90°$ respectively. Closed squares indicate pristine state (ps) before illumination, open squares represents data collected after illumination in the final state (fs). Noise floor indicated by shadow.

To complete the presentation I_r as a function of T is presented in Fig. 4.22. The magnitude of I_r scales to first order as T_c upon illumination and from segment to segment inversely with R_{res}.

The I/U characteristics of $S_{2°}$ in the pristine state display significant dissipation at temperatures well below T_c, which can be well described by a power law dependence as introduced in the corresponding discussion on S_{min}, namely, $U(I) \propto I^{\alpha}$. Fig. 4.23 reports as result of the analysis the magnitude of α as function of T. For temperatures above T_c an ohmic behavior ($\alpha = 1$) is approached as expected. α rises below T_c slowly and approaches a magnitude of $\alpha = 3$ only at $T \approx 100\,\text{mK}$. While this rise of α is in accord with the BKT scenario, the temperature range over which the non-linearities approach the $U \propto I^3$ strength expected at T_{BKT} is unusually large. Again, Segment $\varphi = 0°$ behaves different when compared to Segment $\varphi = 45°$ and $\varphi = 90°$. $\alpha(T)$, for the latter two, agree with a remarkable precision.
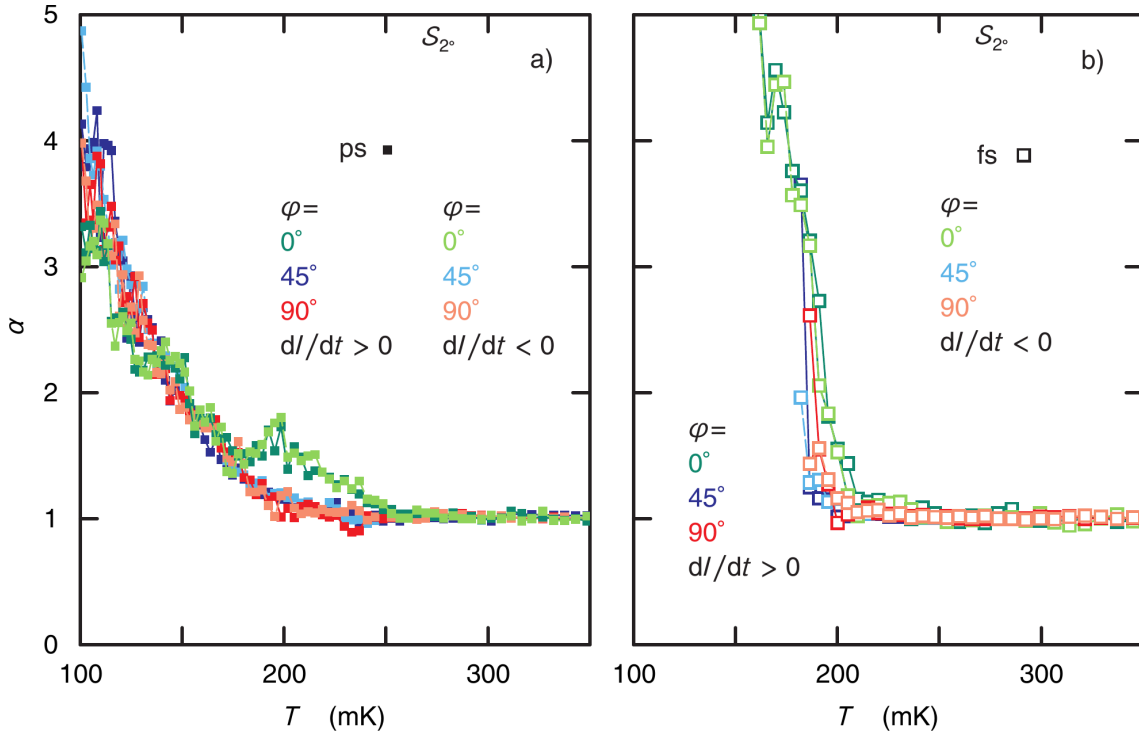
Figure 4.23: Slope of fits α as function of temperature T for different directions of φ. α from measurements before illumination in the pristine state (ps) presented in a), characterization done after illumination in the final state (fs) shown in b). Green color represents $\varphi = 0°$, blue color indicates $\varphi = 45°$ and red color $\varphi = 90°$ respectively. Dark colored squares indicate values extracted from a positive current ramp, brighter colored squares a negative. Lines are guides to the eye.

The analysis of the characteristics in the final state turn out to be more difficult. The temperature range over which the power law fit give reliable estimates for α is rather limited. $\alpha(T)$ rises rapidly for Segment $\varphi = 45°$ and $\varphi = 90°$. Segment $\varphi = 0°$ is special, again. Overall, though, the result presented in Fig. 4.23 for the final state is well in line with a BKT type of transition expected for a 2D superconducting film.

4.2.3   Sample $\mathcal{S}_{6°}$: $\gamma = 6°$

Finally sample $\mathcal{S}_{6°}$ with a nominal tilt of $\gamma = 6°$ with respect to the (001) surface of STO was investigated. Fig. 4.1 c) shows an AFM micrograph from which the mean width of the terraces can be estimated to $w \approx 18\,\text{nm}$, considerably larger than the calculation of $w = \tan(6°)/a \approx 4\,\text{nm}$ using the nominal tilt. Again, (see discussion on sample $\mathcal{S}_{2°}$ in 4.2.2) bunching of several STO layers at the step edges leads to an increase of w and a mean step height of $h = 4.3a$.
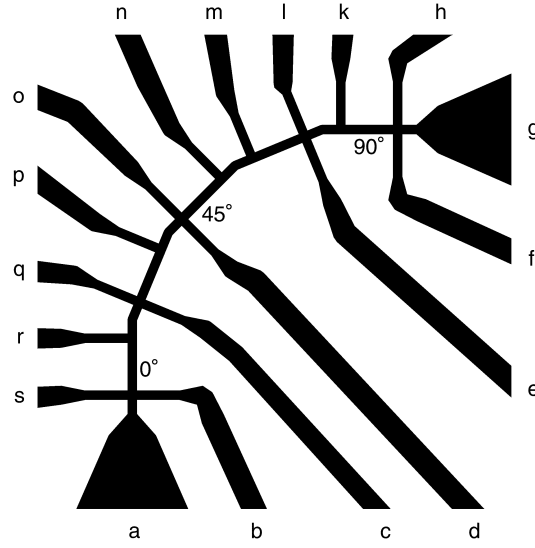
Figure 4.24: A schematic representation of the measurement layout for sample $S_{6°}$. Measurements are performed on the segments labeled by values in degrees. Step edges are aligned perpendicular with respect to the terraces of S_{min} and $S_{2°}$ (see Fig. 4.1 c).

For R_{xx} and R_{xy} characterization a current was biased through contacts $\{a, g\}$ and the potential differences between $\{b, r, s\}$ for Segment $\varphi = 0°$, $\{d, n, o\}$ for Segment $\varphi = 45°$, and $\{f, h, k\}$ for Segment $\varphi = 90°$ was measured (Fig. 4.24).

4.2.3.1   Superconducting transition temperature

$R_\square$ in dependency of the temperature T for the three different segments at $B = 0$ is shown in Figure 4.25. Without illumination at low temperatures all segments display a superconducting transition with $T_c \approx 280\,\text{mK}$ reduced in comparison to sample S_{min} in the pristine state. The magnitude of residual sheet resistance $R_{res} \equiv R_\square(T = 500\,\text{mK})$ and T_c is summarized in Table 4.10. Consistent with $S_{2°}$, R_{res} is ordered as expected: $R_{res}(\varphi = 90°) > R_{res}(\varphi = 45°) > R_{res}(\varphi = 0°)$ indicating a dominant scattering rate at the step edges. In Fig. 4.25, the red curve for Segment $\varphi = 90°$ does not overlap with the blue and the green one before all $R_\square(T)$ measurements collaps in the superconducting state at low temperatures; the lowest T_c was found for $\varphi = 90°$ similar to the characterization of sample $S_{2°}$. In contrast, $R_\square(T)$ coincide for the Segments $\varphi = 0°$ and $\varphi = 45°$ in the lower area of the superconducting transition. The inset in Figure 4.25 shows again a slight shift of the peak of $dR_\square(T)/dT$ for $\varphi = 90°$ to lower temperatures in comparison to the other directions.
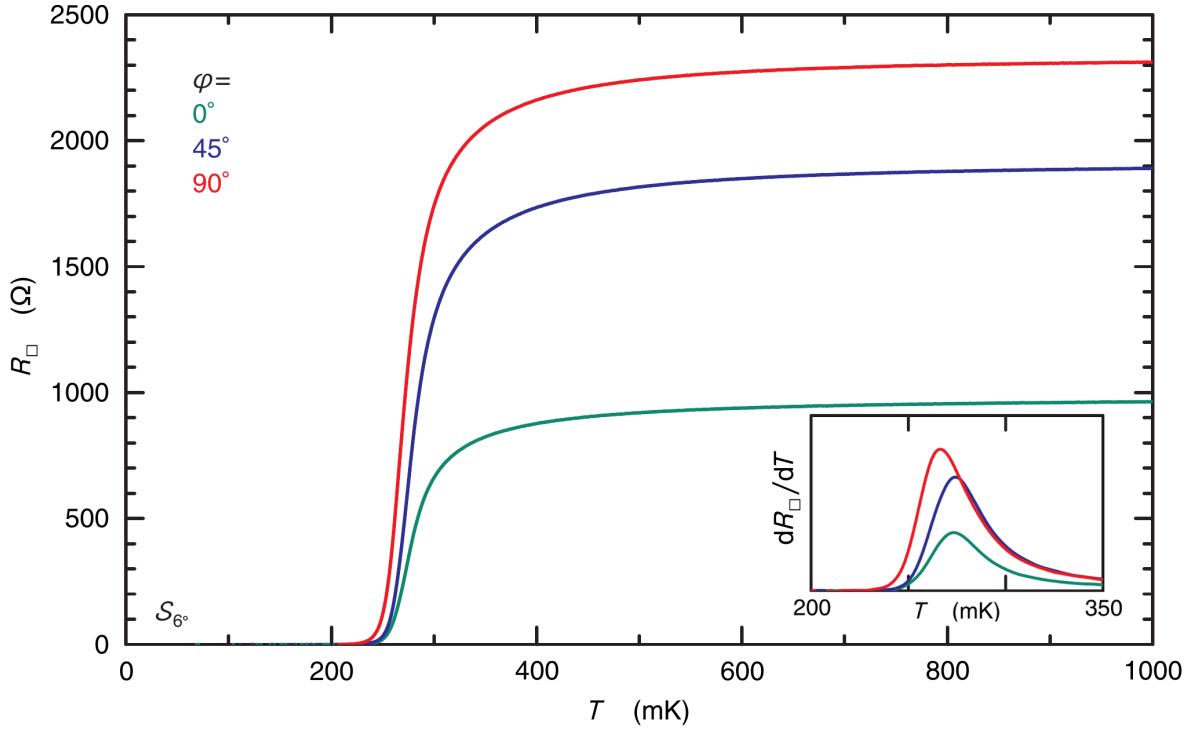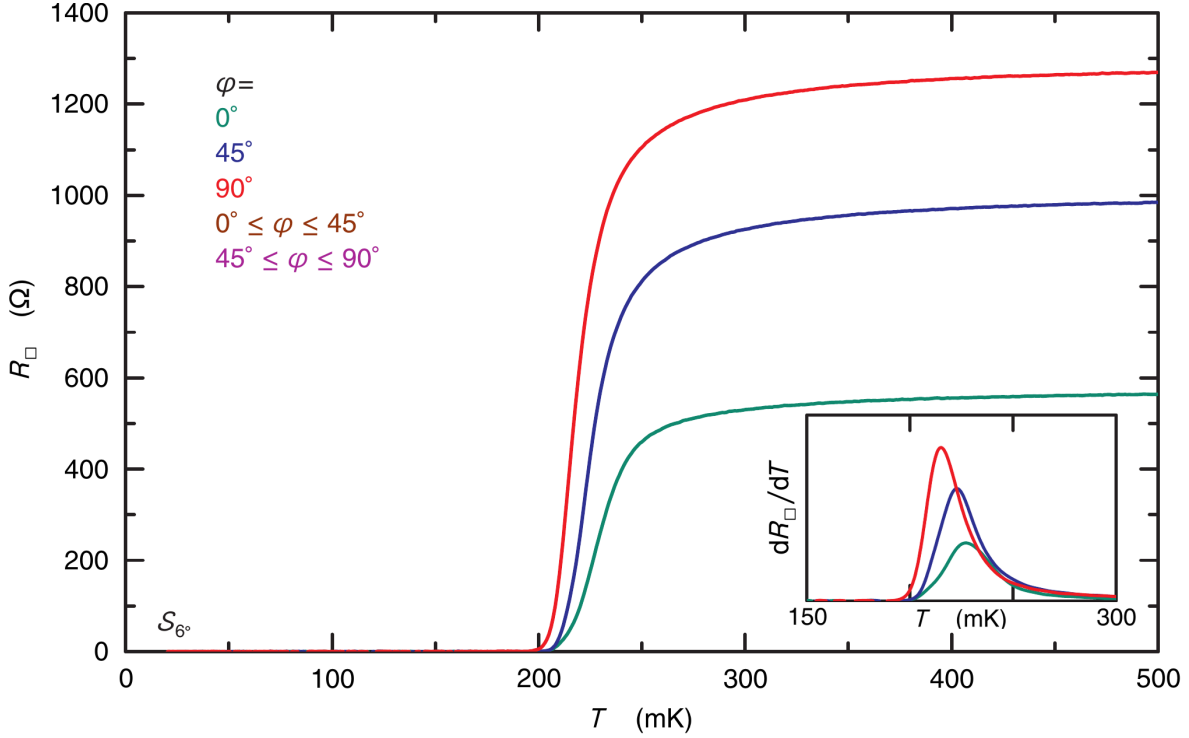
Figure 4.25: Sheet resistance $R_\square$ as function of temperature T at zero magnetic field applied for different current directions φ before illumination. Green color represents $\varphi = 0°$, blue color indicates $\varphi = 45°$ and red color $\varphi = 90°$ respectively. Temperature raised and lowered between $20\,\text{mK}$ and $1\,\text{K}$ during measurement. Inset shows $\mathrm{d}R_\square/\mathrm{d}T$ at the superconducting transition for temperatures between $200\,\text{mK}$ and $350\,\text{mK}$.

Table 4.10: R_{res} and T_c for different φ before illumination for $\mathcal{S}_{6°}$.

φ in °	R_{res} in Ω	T_c in mK from $R(T_c) \equiv R_{\text{res}}/2$	T_c in mK from max. in $\mathrm{d}R_\square/\mathrm{d}T$
0	920	282	273
45	1815	283	274
90	2240	275	266

With illumination the residual sheet resistance as well as the superconducting transition temperature decreases. $R_\square(T)$ in the final state is presented in Fig. 4.26. $R_{\text{res}} \equiv R_\square(500\,\text{mK})$ is reduced by roughly a factor of 2 for all segments and T_c is shifted downwards to $T_c \approx 230\,\text{mK}$. The measurement for Segment $\varphi = 90°$ is still shifted to lower temperatures as compared to the other segments. The derivate $\mathrm{d}R_\square/\mathrm{d}T$ shown in the inset of Figure 4.26 display different temperatures peaking for various φ. Values for T_c and R_{res} can be found in Tab. 4.11.

Figure 4.26: Sheet resistance $R_\square$ as function of temperature T at zero magnetic field applied for different current directions φ after illumination. Green color represents $\varphi = 0°$, blue color indicates $\varphi = 45°$ and red color $\varphi = 90°$ respectively. Temperature raised and lowered between 20 mK and 500 mK during measurement. Inset shows $dR_\square/dT$ at the superconducting transition for temperatures between 150 mK and 300 mK.

Table 4.11: R_{res} and T_c for different φ after illumination for $\mathcal{S}_{6°}$.

φ in °	R_{res} in Ω	T_c in mK from $R(T_c) \equiv R_{res}/2$	T_c in mK from max. in $dR_\square/dT$
0	565	231	228
45	986	227	223
90	1270	220	216

4.2.3.2 $B_{crit}(T)$ measurements

The critical magnetic field B_{crit} as function of temperature T in the pristine and the final state is presented in Figure 4.27. B_{crit} extracted from $R_\square(B, T = \text{const.})$ shows again a trend to saturate in the limit of low temperatures $T \rightarrow 0$ allowing the extraction of the superconducting coherence length ξ described by Eq. 2.6 (see Tab. 4.12). B_{crit} at temperatures below roughly $T \lesssim 200$ mK for the pristine state vary from segment to segment. For currents applied parallel to the step edges, B_{crit} exceeds is slightly larger than 500 mT at $T \rightarrow 0$, while B_{crit} of Segment $\varphi = 90°$ saturates around $B_{crit} = 350$ mK. Thus, compared to the previous

samples the variation of B_{crit} between segments is maximized. Interestingly, the splitting of the $B_{crit}(T)$ curves in the final state after illumination is significantly reduced (see open symbols in Fig. 4.27) from about 40 % in the pristine state to 20 % in the final. Tab. 4.12 gives values for Ginzburg-Landau coherence length ξ calculated from B_{crit}. ξ is of the order of the terrace width $w = 18$ nm. Dissipation associated with the motion of flux vortices at finite magnetic field is more pronounced for a current direction perpendicular to the terraces in which case the vortex motion is directed along the terraces. It is reasonable to expect enhanced pinning forces for vortex motion *perpendicular* to the terraces which in turn leads to enlarged B_{crit} for Segment $\varphi = 0°$ and $\varphi = 45°$. ξ is increased in the final state and thus the enhancement effect of B_{crit} is less pronounced.
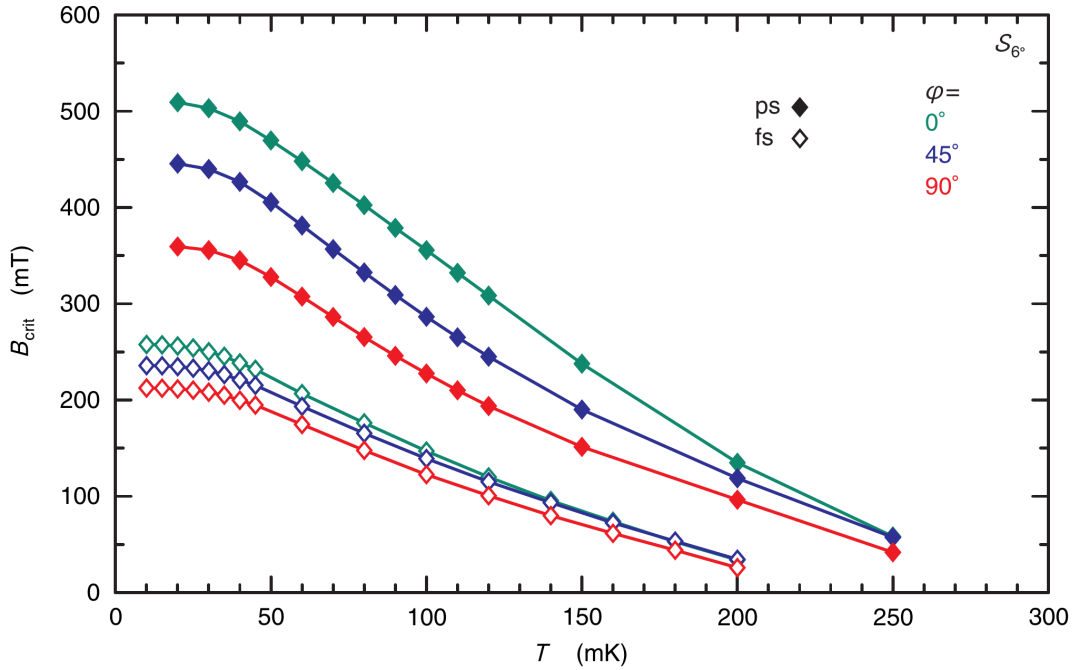
Figure 4.27: Critical field B_{crit} as function of temperature T before and after illumination. Green color represents $\varphi = 0°$, blue color indicates $\varphi = 45°$ and red color $\varphi = 90°$ respectively. Closed diamonds indicate pristine state (before illumination), open diamonds represents data collected after illumination in the final state. Lines are guides to the eye.

Table 4.12: Superconducting coherence length extracted from B_crit saturation values at low temperature for $S_{6°}$ in its pristine state and in the final state after extended illumination.

φ	pristine state		final state	
	B_crit (mT)	ξ (nm)	B_crit (mT)	ξ (nm)
0°	510	25.4	254	36.0
45°	445	27.2	233	37.6
90°	359	30.3	210	39.6

4.2.3.3 Magneto-Transport

Figure 4.28 shows R_{xy} as function of B measured in the pristine as well as in the final state after illumination at low temperatures $T \leq 1\,\text{K}$ (R_{xy} does not change as function of temperature below $T = 1\,\text{K}$). All segments possess a comparable slope with a nearly linear behavior over the whole magnetic field range with approximate Hall coefficient $R_H = -18 \pm 1\,\Omega/\text{T}$ for the pristine state, thus corresponding to a sheet carrier concentration of about $1/(eR_H) = n \approx 3.5 \pm 0.2 \cdot 10^{13}\,\text{cm}^{-2}$. In comparison to the previous samples an increase of n is apparent. In the final state the slope of R_{xy} is reduced by exposure, as already reported for samples S_min and $S_{2°}$. $R_H = -25 \pm 1\,\Omega/\text{T}$ corresponds to $n \approx 2.5 \pm 0.1 \cdot 10^{13}\,\text{cm}^{-2}$.
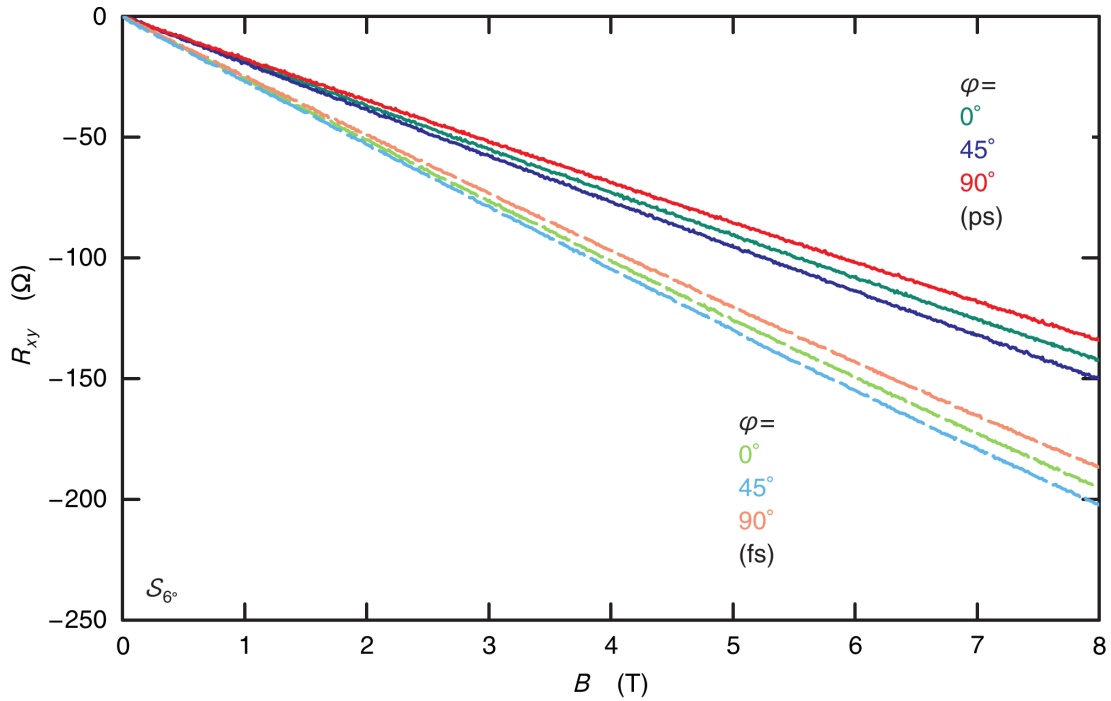
Figure 4.28: R_H as function of applied magnetic field B measured at $T \leq 1\,\mathrm{K}$ before and after illumination for different directions of φ. Green color represents $\varphi = 0°$, blue color indicates $\varphi = 45°$ and red color $\varphi = 90°$ respectively. Pristine state (ps) before illumination represented by solid lines, final state (fs) after illumination indicated by broken lines with brighter coloring.

4.2.3.4 *I/U* characteristics

Characteristic curves at $100\,\mathrm{mK}$ The I/U characteristics measured at $100\,\mathrm{mK}$ before and after illumination are presented in Figure 4.29. Again, the highest magnitude for I_r can be retrieved for a current applied along the step terraces, where $\varphi = 0°$. The variation of I_r for different segments is larger than for $S_{\min}$ and $S_{2°}$. This increase of anisotropy is most probably caused by an enhanced step edge density. Like in the measurements of previous samples, I_r is decreasing with the influence of illumination. I_c shows the opposite behavior and will be discussed in details when looking at the temperature dependence of $I_c(T)$ (see Fig. 4.30).
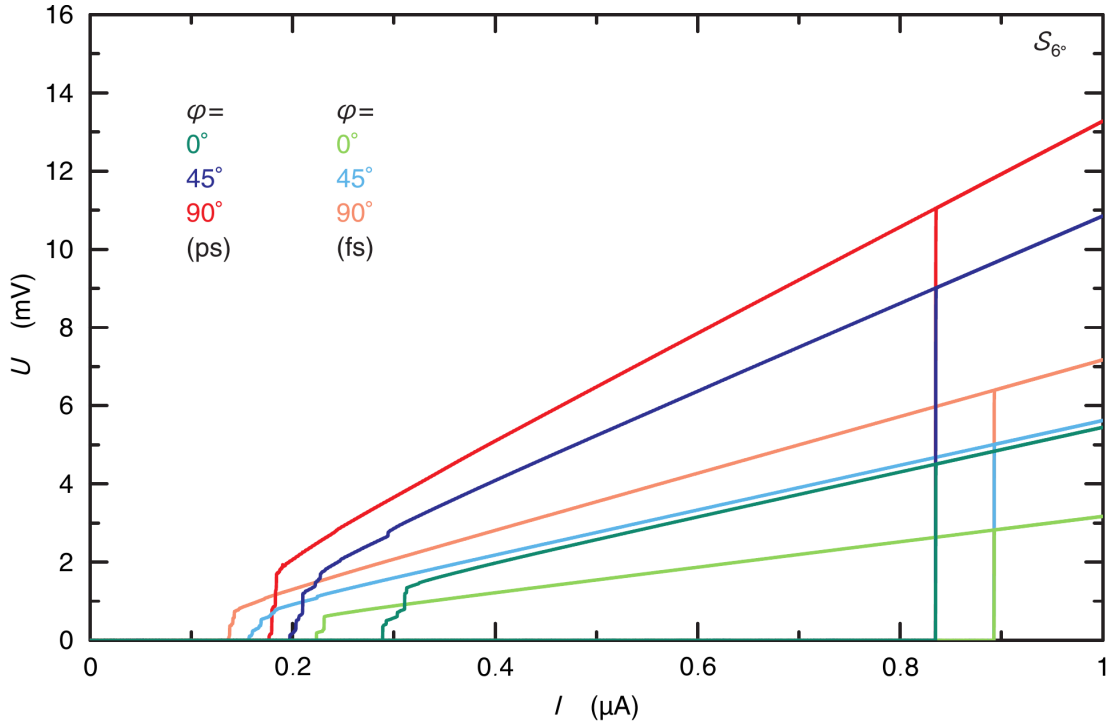
Figure 4.29: I/U characteristics at 100 mK before illumination in the pristine state (ps) and after influence of light in the final state (fs) without applied magnetic field. Green color represents $\varphi = 0°$, blue color indicates $\varphi = 45°$ and red color $\varphi = 90°$ respectively. Brighter coloring indicate final state after extended illumination.

Table 4.13: Current direction φ, Critical current I_c, retrapping current I_r and number of steps N before illumination in the pristine state (ps) and after illumination in the final state (fs) for $\mathcal{S}_{6°}$.

	pristine state			final state		
φ	I_c (nA)	I_r (nA)	N	I_c (nA)	I_r (nA)	N
0°	837.6	288.9	6	905.9	223.4	2
45°	837.5	197.1	7	905.8	157.0	3
90°	837.4	176.6	7	905.8	136.8	4

Characteristic curves as function of T   To get a more detailed picture of the behavior of I_c and I_r, an analysis of I/U characteristics for as function of temperature is presented. Fig. 4.30 a) and b) show I_c and I_r as function of T, respectively, for the pristine state (closed symbols), as well as for the final state (open symbols). $I_c(T)$ agrees for all segments except in the temperature range above $T \gtrsim 180$ mK in the final state. Again, similarities to the generic behavior sketched in Fig. 4.10 are evident with two different contribution at lower

and higher temperature. Both contributions shift to lower T upon exposure to light.

$I_r(T)$ represented in Figure 4.30 b) displays the by now familiar dependence. The highest magnitude of I_r is found for Segment $\varphi = 0°$, while the smallest value for Segment $\varphi = 90°$. I_r shifts to lower values and its onset to lower T.
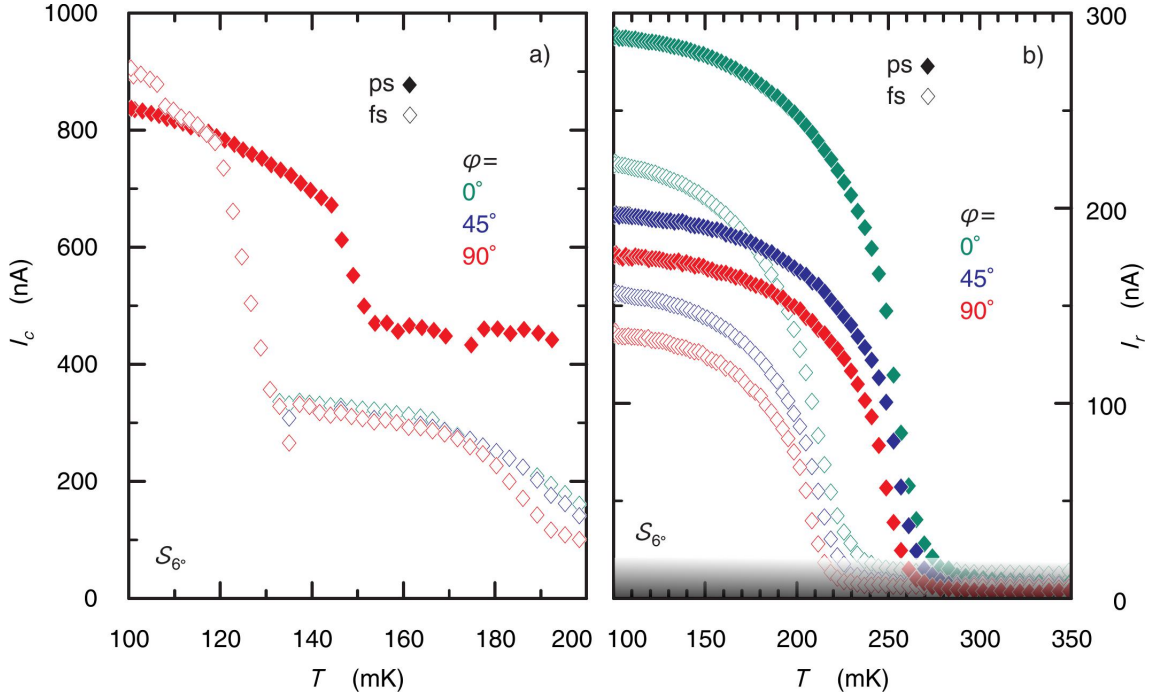
Figure 4.30: a) Critical current I_c in dependency of temperature T before and after illumination. b) Retrapping current I_r in dependency of temperature T before and after illumination. Green color represents $\varphi = 0°$, blue color indicates $\varphi = 45°$ and red color $\varphi = 90°$ respectively. Due to switching between resistive and superconducting phase occur at same currents, the data points are superimposed and only red data pints are visible. Noise floor indicated by shadow.

Finally the BKT temperature T_{BKT} is determined using the slope α extracted from logarithmic plotted I/U characteristics. Fig. 4.31 show how $\alpha(T)$ rises with reducing temperatures before illumination. A deviation from ohmic behavior with $\alpha = 1$ can be found for all segments below $T \lesssim 250$ mK, but a clear rise to $\alpha = 3$ indicative of a transition temperature T_{BKT} is difficult to identify quite similar to the discussion of α in S_{min}. The final state after illumination however is describable by a well defined T_{BKT}. An ohmic range can be found down to temperatures of about 210 mK. All segments show a steep rise of α between 200 mK $\lesssim T \lesssim 210$ mK, leading to $T_{BKT} = 202 \pm 2$ mK.
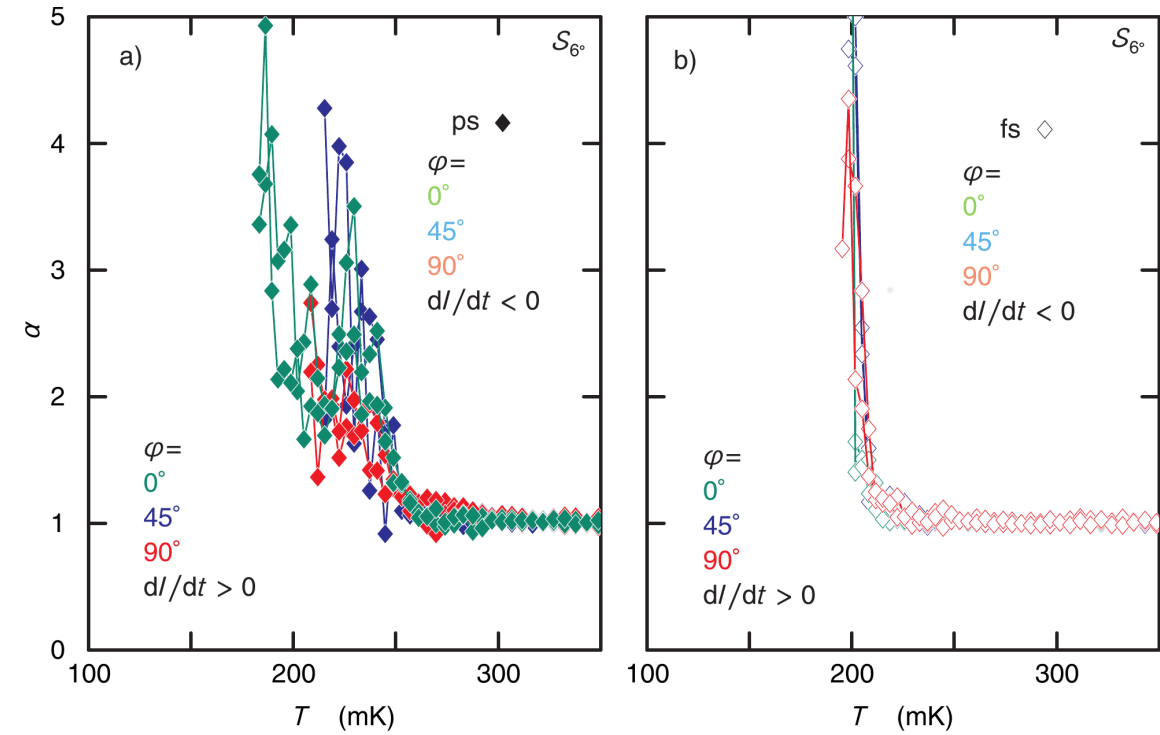
Figure 4.31: Slope of fits α as function of temperature T for different directions of φ. a) before illumination, b) after influence of light. Green color represents $\varphi = 0°$, blue color indicates $\varphi = 45°$ and red color $\varphi = 90°$ respectively. Open Diamonds indicate values extracted from a positive current ramp, closed a negative. Lines are guides to the eye.

4.3 Summary and discussion of results

In this chapter a careful characterization of three samples with different vicinal substrate tilts γ was presented. To compare the measurements and to evaluate the influence of γ on the electrical transport properties, the following section will discuss and summarize the parameters for transport at low temperatures extracted before. Therefore in the following Figures circles represent S_{min} ($\gamma \approx 0.19°$), squares and diamonds display Sample $S_{2°}$ ($\gamma = 2°$) and $S_{6°}$ ($\gamma = 6°$) respectively. Again the current along the step edges with $\varphi = 0°$ is indicated in green, $\varphi = 45°$ is marked with blue and $\varphi = 90°$ with red. The final state after illumination will be indicated with open symbols.
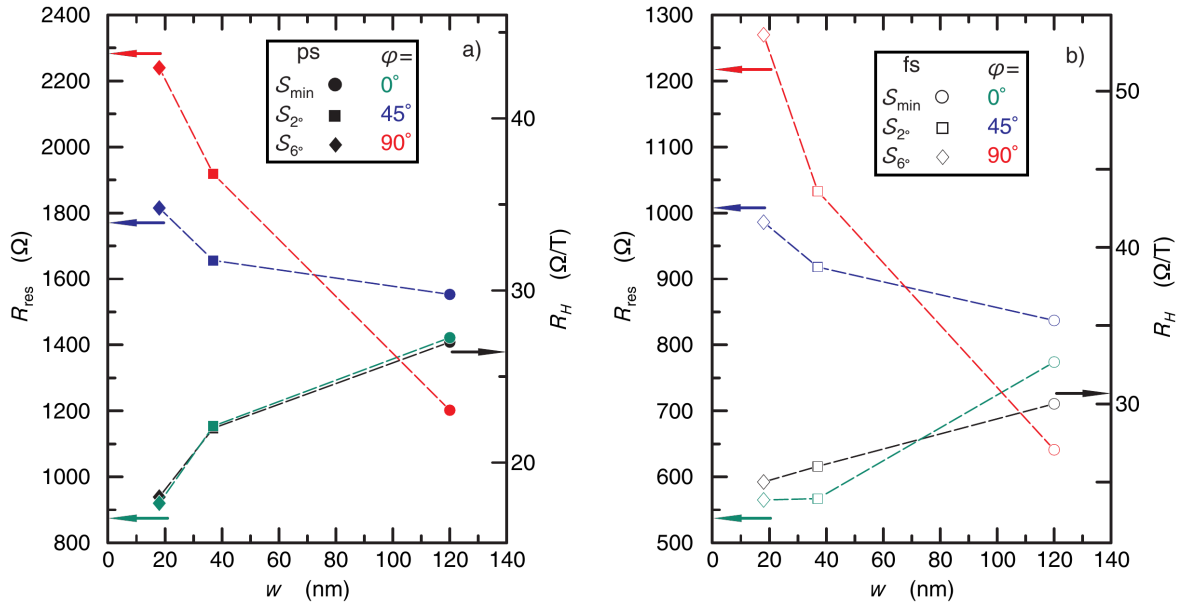
Figure 4.32: R_{res} (left scale) and R_H (right scale) in dependency of w for all measured AO/STO samples before illumination in the pristine state (ps, closed symbols in a) and in the final state after illumination (fs, open symbols in b). Sample S_{min} is represented with circles, squares indicate characterizations on the $S_{2°}$ and diamonds on $S_{6°}$ respectively. The different segments can be distinguished by color: $\varphi = 0°$ (green), $\varphi = 45°$ (blue) and $\varphi = 90°$ (red). Lines are guides to the eye.

To control the charge carrier density n of the 2DES in sample preparation is a formidable task. The mechanism of charge carrier generation is still under debate. In the case of the AO/STO interface it most likely depends on the amount of oxygen vacancies produced by the contact between slightly oxygen deficient Al_2O_3 and the $SrTiO_3$ substrate. Slight variation in the outcome are unavoidable. In the samples S_{min}, $S_{2°}$, and $S_{6°}$ charge carrier concentration is measured by means of the Hall coefficient R_H after cool-down. Figure 4.32 shows R_H in dependence of the experimentally determined terraces width w, as well as the residual sheet resistance R_{res}. Obviously the Hall data scale almost perfectly with the R_{res} magnitude of

Segment $\varphi = 0°$. Using the most elementary treatment in the framework of Drude theory, the ratio of R_{res} and R_H defines the charge carrier mobility μ

$$\mu = \frac{R_H}{R_{res}},$$

which is estimated as $\mu \approx 192\,\text{cm}^2/\text{Vs}$ from the values in Fig. 4.32 a) independent of the specific sample. For Segment $\varphi = 0°$ the current is applied along the terraces and is not influenced by step edges. The relaxation time associated with R_{res} is in this case solely determined by defect properties of the substrate which obviously do not change. In the contrary for Segment $\varphi = 45°$ and $\varphi = 90°$ R_{res} depends strongly on the tilt of the vicinal substrate γ. This is strong evidence of the intended influence of step edges on the transport properties. The characterization of R_{res} and R_H in the final state after illumination (see Fig. 4.32 b)) further supports this picture, although the agreement between R_H and R_{res} is not so perfect anymore. In the final state $R_{xy}(B)$ has the tendency to develop non-linear behavior which signals deviation from the crude assumption of the Drude picture underlying the proportionality of R_H and R_{res}. The experimental findings reported here are not in line with the picture proposed by Joshua *et al.* 2012. In the framework of a two-band approximation Segment $\varphi = 0°$ of Sample $\mathcal{S}_{2°}$ possess for unknown reasons a by a factor of two lower carrier concentration than the rest of the sample. This has little effect on T_c in contrast to findings by electric field-effect induced tuning. Exposure to light reduces the apparent charge carrier density (as signaled by a larger $|R_H|$) and at the same time lead to non-linearities in $R_{xy}(B)$ in clear opposition to the view promoted by Joshua *et al.* 2012.

A more likely scenario is proposed here. Physical properties of STO-based 2DES are in many cases governed by inhomogeneities in charge carrier concentration caused by, *e. g.*, clustering of oxygen vacancies at domain boundaries of the tetragonal twinning structure (Yazdi-Rizi *et al.* 2016), terrace step edges or crystal defects. Transport measurements on macroscopic samples probe a mesoscopic network by an inhomogeneous current density and represent a only vaguely controlled averaging procedure. Segment $\varphi = 0°$ of sample $\mathcal{S}_{2°}$ happens to have by chance a Hall voltage of unusual size, due to a specific arrangement of the internal structure of $\mathcal{S}_{2°}$.
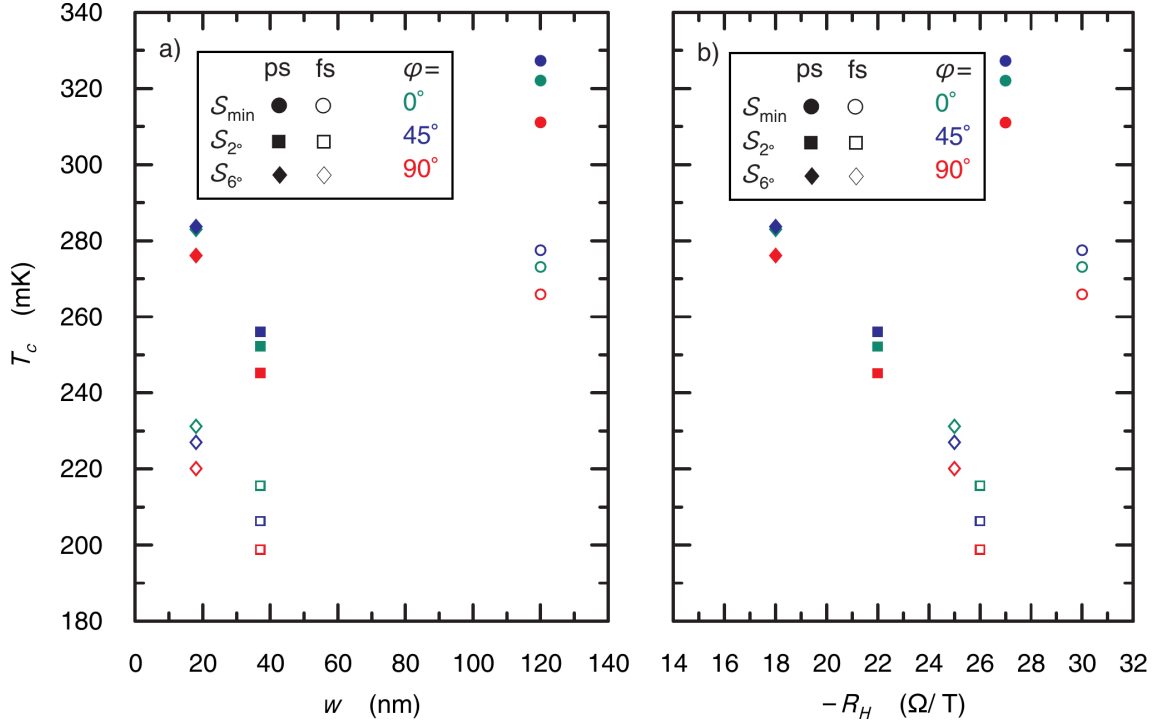
Figure 4.33: Comparison of T_c as function of w (a) and R_H (b) before (pristine state, closed symbols) and after illumination (final state, open symbols) for all AO/STO samples. Sample $S_{\min}$ is represented with circles, squares indicate characterizations on the $S_{2°}$ and diamonds on $S_{6°}$ respectively. The different segments can be distinguished by color: $\varphi = 0°$ (green), $\varphi = 45°$ (blue) and $\varphi = 90°$ (red).

In this PhD project it was shown, that exposure by light at low temperatures shifts T_c downwards (see Ch. 3). In this chapter we tested the hypothesis that γ tunes T_c as well. Results are presented in Fig. 4.33 a). T_c is shown as function of w for the pristine and final state of the three investigated samples. No clear trend is visible. Clearly T_c behaves anisotropic with respect to φ and is always smallest for currents applied perpendicular to the terraces, *i. e.* for Segments $\varphi = 90°$. Thus terraces do have an influence on T_c. However, the anisotropic splitting between different segments is significantly lower than the overall variations. For a more accurate statement, sufficient sample statistics would have to be obtained to probe this variation.

It is well known that the superconducting transition temperature T_c depends on the gate voltage V_g as shown by a large number of publications tuning n by the electric field effect (Joshua *et al.* 2012; Herranz *et al.* 2015; Gariglio *et al.* 2016 and references therein). The appearance of a maximum in T_c at critical gate voltage V_c separates naturally an under-doped from an over-doped regime. This is possible since V_g correlates with n as well as the conductance $1/R_{\text{res}}$.

In Fig. 4.33 b) T_c is plotted as function of R_H and on a first glance no clear trend is seen

either. However, the anti-correlated response of R_H and T_c to illumination is a surprising observation. With decreasing $n = 1/eR_H$ the superconducting T_c shifts to higher temperatures. The natural correlation of V_g, n and $1/R_{res}$ seen in gating experiments is in contrast to the current observation where the illumination dose D is used instead of V_g to stimulate a response of $1/R_{res}$ which is here surprisingly anti-correlated to n extracted from Hall measurements. The dependency of T_c on n is clear evidence for the under-doped regime. Since the presentation here is limited to transport measurements, one has to be careful when interpreting the Hall data. For instance Herranz *et al.* 2015 compared Hall measurements to capacitance measurements of the charge carrier density and found a deviation in the over-doped regime, where a multi-band transport is supposed. A transfer to the measurements presented here is hardly possible without knowing the way of analysis of the Hall data by Herranz *et al.* 2015, which is unfortunately not shown. In contrast, here, a reduction of n is seen in the Hall data but in the limited field range accessible only one possible band can be identified.
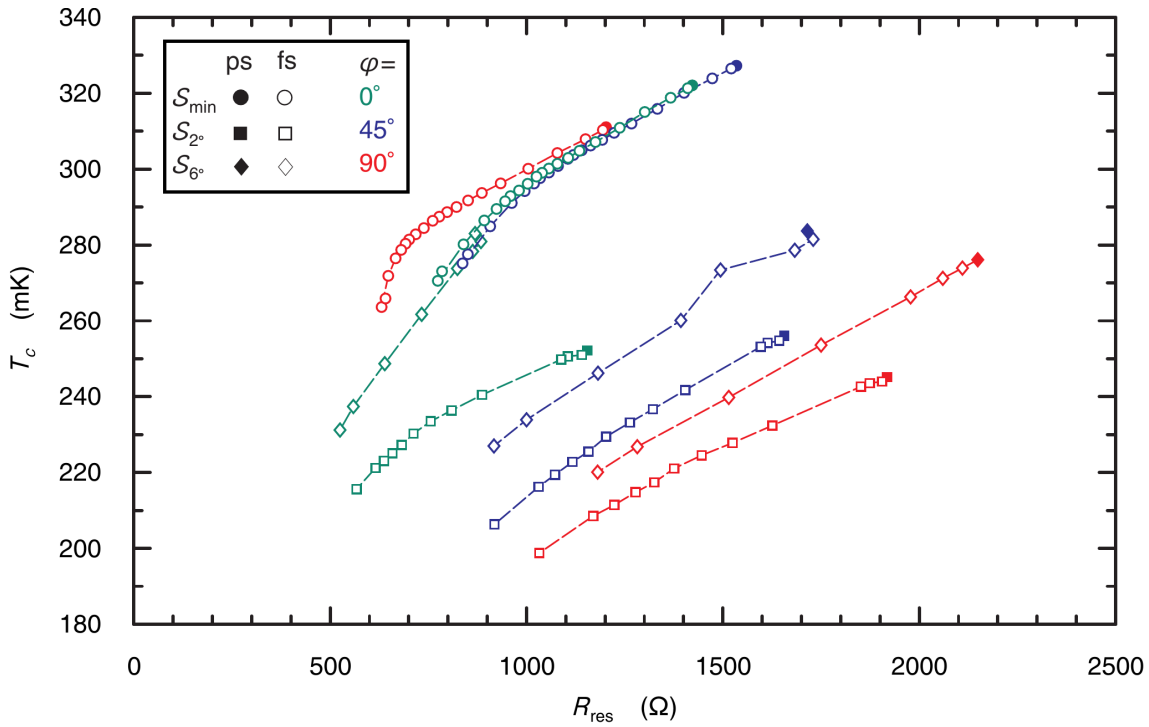
Figure 4.34: T_c in dependency of R_{res} for all measured AO/STO samples for various illumination steps. Sample $\mathcal{S}_{min}$ is represented with circles, squares indicate characterizations on the $\mathcal{S}_{2°}$ and diamonds on $\mathcal{S}_{6°}$ respectively. Pristine state (ps) before illumination is indicated by closed symbols, the final state (fs) after illumination is represented by open symbols. The different segments can be distinguished by color: $\varphi = 0°$ (green), $\varphi = 45°$ (blue) and $\varphi = 90°$ (red). Lines are guides to the eye.

A summary of all resistive states approached by successive illumination is shown for the three samples in Fig. 4.34. A linear behavior of T_c vs. R_{res} is observed in most cases with a similar dT_c/dR_{res}. For $\mathcal{S}_{min}$ all segments show quite similar behavior at $R_{res} > 1 \, k\Omega$. Segment $\varphi = 90°$ separates in a peculiar manner with a strong downturn before reaching the final state. The trend set by Segment $\varphi = 0°$ and $\varphi = 45°$ is continued by Segment $\varphi = 0°$ of $\mathcal{S}_{6°}$. As discussed in connection with Fig. 4.32 terraces do not influence the transport in $\varphi = 0°$ segments. This is reflected by the T_c dependency of Segment $\varphi = 0°$ of $\mathcal{S}_{min}$ and $\mathcal{S}_{6°}$. Segment $\varphi = 0°$ of $\mathcal{S}_{2°}$ is special in this sense. As pointed out numerous times during this chapter, this segment displays unique features in almost all investigated properties. In Fig. 4.34 the diversification of $T_c(R_{res})$ caused by φ is clearly discernible and the reduction of T_c is strongest for $\varphi = 90°$.

It is beneficial to plot the data of Fig. 4.34 in a scaled fashion (see Fig. 4.35). Two sets of curves can be distinguished. While essentially all segments on two high-tilt substrates ($\mathcal{S}_{2°}$ and $\mathcal{S}_{6°}$) follow a linear trend over the whole range of resistive states, $\mathcal{S}_{min}$ starts off with a lower slope and show a characteristic downturn before reaching the final state. Once more, Segment $\varphi = 0°$ of $\mathcal{S}_{2°}$ does not fit the general picture.
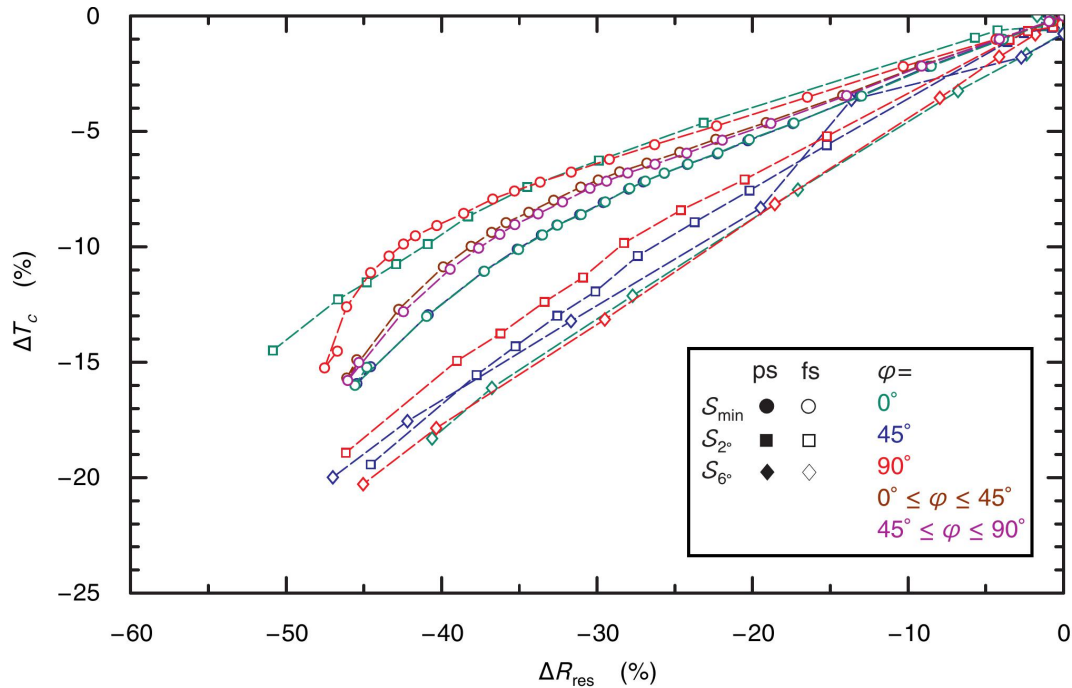
Figure 4.35: Change of T_c and R_{res} for different illumination steps for all AO/STO samples. Sample $\mathcal{S}_{min}$ is represented with circles, squares indicate characterizations on the $\mathcal{S}_{2°}$ and diamonds on $\mathcal{S}_{6°}$ respectively. Pristine state (ps) before illumination is indicated by closed symbols, the final state (fs) after illumination is represented by open symbols. The different segments can be distinguished by color: $\varphi = 0°$ (green), $\varphi = 45°$ (blue) and $\varphi = 90°$ (red). Lines are guides to the eye.

Compared to the investigation of the LAO/STO sample presented in the previous Ch. 3, where R_{res} can be reduced by a factor of five and T_c by 30 % with light, here, for the AO/STO samples, a lowering by factor of 2 for R_{res} and simultaneously a shift of T_c down by $15 - 20$ % is presented in Fig. 4.34. As discussed by Yazdi-Rizi *et al.* 2016, the origin of the confinement of charge carriers is different and stronger for the AO/STO interface compared to LAO/STO. A smaller thickness of the conducting layer could be the reason for a reduced sensitivity of the light tuning for AO/STO.

Finally, results on the critical magnetic field B_{crit} are collected in Fig. 4.36. All Segments $\varphi = 90°$ show a reduced B_{crit} in comparison to the other directions. The mean magnitude of B_{crit} seen in S_{min} corresponds – within the framework of elementary treatments (see Eq. 2.6) – to the Ginzburg-Landau coherence length $\xi \approx 35$ nm and are comparable to characterizations reported in the literature (Herranz *et al.* 2015). ξ does not change much upon lowering the terrace width to about 37 nm in $S_{2°}$ as expected. A significant change however is seen as soon as w is smaller than $\xi(S_{min})$. At the same time the anisotropy is apparently strongly enhanced and gives an indication of the correct estimation of ξ. Data extracted from the final state after illumination show a reduced anisotropic behavior with respect to φ for all measured samples.
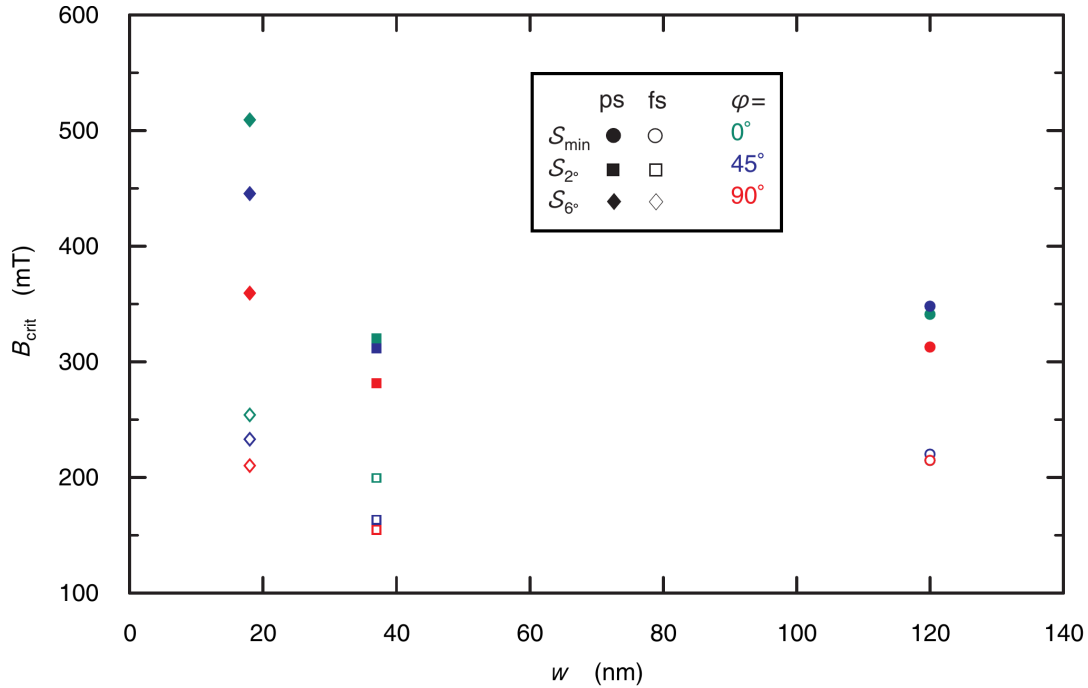
Figure 4.36: B_{crit} as function of w. Sample S_{min} is represented with circles, squares indicate characterizations on the $S_{2°}$ and diamonds on $S_{6°}$ respectively. The different segments can be distinguished by color: $\varphi = 0°$ (green), $\varphi = 45°$ (blue) and $\varphi = 90°$ (red). Closed symbols indicate pristine states (ps) before illumination, open symbols represent final states (fs) after influence of light.

One possibility to understand this findings is that the conducting layer extends deeper in the STO substrate after illumination. Then, scattering at step terraces is less important, resulting in a lower residual sheet resistance and a reduced apparent anisotropy. However, this contradicts findings of Yazdi-Rizi *et al.* 2017, which showed that the thickness of the conducting layer is constant within the measurement resolution after the influence of light. As already suggested in Ch. 3, measurements of the critical magnetic field parallel to the interface – to estimate the thickness of the superconducting layer for different illumination states – would be helpful to make a clear statement. An first statement can be made based on previously presented analysis of the BKT-transition. The presence of such transition is discussed as a hallmark for 2D superconductivity. Therefore even if there is a change in the thickness of the conducting layer, it is bound by the coherence length ξ. Otherwise superconductivity would crossover to a 3D behavior.

In most experiments (see *e. g.* Herranz *et al.* 2015; Monteiro *et al.* 2017) the expected linear behavior of B_{crit} in the vicinity of T_c is used to calculated B_{crit} in limes of $T \rightarrow 0$. In temperature range of measurements presented in this Chapter B_{crit} strongly deviates from textbook dependency of ordinary one-band superconductors. For instance the slope of B_{crit} vs. T closed to vanishing B_{crit} at T_c does not extrapolate to anything close to the saturation values found at low temperatures. This might be a further hint towards the presence of multiple bands contributing to superconductivity (Edge *et al.* 2015).

Chapter 5

Summary

$SrTiO_3$-based heterostructures display a huge variety of different physical effects. With various external stimuli the system can be manipulated to investigate a multitude of phenomena. In this thesis two tuning parameters for the electronic transport at low temperatures at STO-based heterostructures were introduced: illumination by light at low temperatures and the vicinal substrate tilt γ. The influence of those parameters were presented by transport measurements on the $Al_2O_3/SrTiO_3$ (AO/STO) interface, as well as the widely studied $LaAlO_3/SrTiO_3$ (LAO/STO) heterostructure.

To illuminate a sample at low temperatures a light emitting diode (LED) working at dilution fridge temperatures was introduced in Ch. 3. An extensively characterization of the radiation behavior of the given LED with an home-build setup was made to gain knowledge about the illumination dose D absorbed by the sample even at low currents biased through the LED. The influence of light at low temperatures on the superconducting properties were studied with measurements performed in the dilution refrigerator. It is possible to reduce the residual sheet resistance R_{res} at $500\,mK$ with Ω precision using light. R_{res} was decreased down by a factor of 5 in a step wise manner, while at different resistive states a careful characterization of altered transport characteristics was performed. As long as the temperature of the sample was kept below $T < 1\,K$ all transport characteristics are stable over time. By increasing the illumination dose D the superconducting transition temperature T_c shifts to lower temperatures. The persistent change of transport characteristics due to illumination can be reverted by elevating the temperature to moderate $12\,K$, while reports by others published during the time of this PhD project suggests a recovery of the pristine state requires temperatures well above $100\,K$. A careful analysis of I/U characteristics reveals a reduction of inhomogeneities under the influence of illumination. This can be seen also in magneto-transport measurements, where a similar $R_{xx}(B = 0)$ can be approached with different routes using light and thermal relaxation. $R_{xy}(B)$ is identical for both routes. However, the longitudinal resistance $R_{xx}(B)$ differs, which clearly violates Kohler's rule. Either one has to accept that the Fermi surface is different for identical R_{res} and depend on the route by which a state is approached or illumination changes the internal arrangement of inhomogeneities.

In view of the unchanged R_{xy} the latter argument is much more likely. R_{xx} shows a pronounced linear behavior at higher magnetic fields $B > 2\,\mathrm{T}$ with increased D, which strongly deviates from generic magneto-resistance characteristics. This further supports the picture proposed here. A weak anti-localization dip in R_{xx} was detectable at all illumination steps giving evidence of strong spin-orbit coupling. The Hall resistance R_{xy} show an increase of non-linearities with rising D.

After various improvements of the measurement setup (description in Sec. 2.4.3), a characterization of longitudinal as well as transversal resistance could be performed simultaneously in Ch. 4. A special sample layout makes it possible to bias the current along various crystallographic directions. Three samples of AO/STO heterostructures with varying vicinal substrate tilt γ were investigated. With γ, the width of the resulting terraces w as well as the height of the step edges were altered. For R_{res} determined with a current biased along terraces $\varphi = 0°$, no influence of γ was detectable on the charge carrier mobility μ, as expected. However, a distinct reduction of scattering times was detected for measurements across step edges. Most prominent, an increase of R_{res} was found for a current applied perpendicular to the step edges ($\varphi = 90°$). The superconducting transition temperature T_c differs with respect to different current directions and is always smallest for $\varphi = 90°$. Nevertheless, a clear dependency of T_c on γ was not found. Anisotropy of the upper critical field B_{crit} with respect to φ was also observed and increases with γ. However, the *mean* magnitude of B_{crit} does not show a clear trend, like any other accessible parameter studied in Ch. 4, *i. e.* I_c, I_r and T_{BKT}. A reduction of T_c as well as R_{res} with increasing illumination dose D was detected for all samples. $\mathrm{d}T_c/\mathrm{d}R_{\mathrm{res}}$ as function of D distinguish the high tilt samples $\mathcal{S}_{2°}$ and $\mathcal{S}_{6°}$ from the specimen with minimal γ, $\mathcal{S}_{\mathrm{min}}$.

Surprisingly R_{res} does not scale with R_H as expected upon illumination. Obviously, the illumination does *not* generate new charge carriers which are signaled by a decreasing R_H. On the contrary, after illumination a certain amount of charge carriers do not contribute to electrical transport anymore and this loss is overcompensated by an increase in μ leading to an overall increase of conductance. So the dominating effect of illumination lies in reduction of scattering, which can be interpreted as a *purification* process. An important implication concerns the classification of our results as charge carrier density tuning in the so-called over-doped regime. Despite our decreasing resistance on illumination the charge carrier concentration is apparently reduced. Hence the decrease of T_c is associated with a reduction of charge carrier concentration which places our experiments in the under-doped regime. In contrast to gating experiments coming to the same conclusion (Gariglio *et al.* 2016), the non-volatile tuning presented here makes investigation of transport possible in the vicinity of the interface without applying a permanent stimulus to the sample.

List of Figures

Bibliography

Ambegaokar, V. and A. Baratoff (1963). "Tunneling Between Superconductors." In: *Phys. Rev. Lett.* 10 (11). DOI: 10.1103/PhysRevLett.10.486. Corrected in "Tunneling Between Superconductors." In: *Phys. Rev. Lett.* 11 (2). DOI: 10.1103/PhysRevLett.11.104.

Arnold, D. *et al.* (2018). "Influence of persistent photoconductivity on superconductivity in the $SrTiO_3$/$LaAlO_3$-interface." In: Poster presented at 12th International Conference on Materials and Mechanisms of Superconductivity and High Temperature Superconductors.

Arnold, D. *et al.* (2019). "Tuning the superconducting transition of $SrTiO_3$-based 2DEGs with light." In: *Applied Physics Letters* 115.12. DOI: 10.1063/1.5119417.

Bardeen, J., L. N. Cooper, and J. R. Schrieffer (1957). "Microscopic Theory of Superconductivity." In: *Phys. Rev.* 106 (1). DOI: 10.1103/PhysRev.106.162.

Barone, A. and G. Paternó (1982). *Physics and Applications of the Josephson Effect*. John Wiley & Sons, Ltd. DOI: https://doi.org/10.1002/352760278X.

Bednorz, J.G. and H.J. Scheel (1977). "Flame-fusion growth of $SrTiO_3$." In: *Journal of Crystal Growth* 41.1. DOI: https://doi.org/10.1016/0022-0248(77)90088-4.

Ben Shalom, M. *et al.* (2010). "Tuning Spin-Orbit Coupling and Superconductivity at the $SrTiO_3$/$LaAlO_3$ Interface: A Magnetotransport Study." In: *Phys. Rev. Lett.* 104 (12). DOI: 10.1103/PhysRevLett.104.126802.

Benfatto, L., C. Castellani, and T. Giamarchi (2009). "Broadening of the Berezinskii-Kosterlitz-Thouless superconducting transition by inhomogeneity and finite-size effects." In: *Phys. Rev. B* 80 (21). DOI: 10.1103/PhysRevB.80.214506.

Berezinskiĭ, V. L. (1970). "Detruction of Long-Range Order in One-Dimensional and Two-Dimensional Systems Having a Continuous Symmetry Group I. Classical Systems." In: *Soc. Phys. JETP* 32.1. [Zh. Eksp. Teor. Fiz **59**, 907-920 (September, 1970)].

— (1972). "Detruction of Long-Range Order in One-Dimensional and Two-Dimensional Systems Having a Continuous Symmetry Group II. Quantum Systems." In: *Soc. Phys. JETP* 34.3. [Zh. Eksp. Teor. Fiz **61**, 1144–1156 (September, 1971)].

Bergmann, G. (1984). "Weak localization in thin films: a time-of-flight experiment with conduction electrons." In: *Physics Reports* 107.1. DOI: https://doi.org/10.1016/0370-1573(84)90103-0.

Biscaras, J. *et al.* (2010). "Two-dimensional superconductivity at a Mott insulator/band insulator interface LaTiO$_3$/SrTiO$_3$." In: *Nature Communications* 1.1. DOI: 10.1038/ncomms1084.

Caviglia, A. D. *et al.* (2008). "Electric field control of the LaAlO$_3$/SrTiO$_3$ interface ground state." In: *Nature* 456.7222. DOI: 10.1038/nature07576.

Caviglia, A. D. *et al.* (2010). "Tunable Rashba Spin-Orbit Interaction at Oxide Interfaces." In: *Phys. Rev. Lett.* 104 (12). DOI: 10.1103/PhysRevLett.104.126803.

Chen, Y. Z. *et al.* (2013). "A high-mobility two-dimensional electron gas at the spinel/perovskite interface of γ-Al$_2$O$_3$/SrTiO$_3$." In: *Nature Communications* 4.1. DOI: 10.1038/ncomms2394.

Cheng, L. *et al.* (2017). "Optical Manipulation of Rashba Spin–Orbit Coupling at SrTiO$_3$-Based Oxide Interfaces." In: *Nano Letters* 17.11. DOI: 10.1021/acs.nanolett.7b02128.

Christensen, D. V. *et al.* (2019). "Stimulating Oxide Heterostructures: A Review on Controlling SrTiO$_3$-Based Heterointerfaces with External Stimuli." In: *Advanced Materials Interfaces* 6.21. DOI: 10.1002/admi.201900772.

Collignon, C. *et al.* (2019). "Metallicity and Superconductivity in Doped Strontium Titanate." In: *Annual Review of Condensed Matter Physics* 10.1. DOI: 10.1146/annurev-conmatphys-031218-013144.

Cui, W. (2010). "Charge Transport in Single Cooper-pair Transistors." PhD thesis. Karlsruher Institut für Technologie (KIT): Karlsruhe Institut of Technology, Institute of Solid State Physics.

Edge, J. M. and A. V. Balatsky (2015). "Upper Critical Field as a Probe for Multiband Superconductivity in Bulk and Interfacial STO." In: *Journal of Superconductivity and Novel Magnetism* 28.8. DOI: 10.1007/s10948-015-3052-3.

Fuchs, D. (2020). personal communication.

Fuchs, D. *et al.* (2014). "Two-dimensional superconductivity between SrTiO$_3$ and amorphous Al$_2$O$_3$." In: *Applied Physics Letters* 105.9. DOI: 10.1063/1.4895120.

Fuchs, D. *et al.* (2017). "Patterning of two-dimensional electron systems in SrTiO$_3$ based heterostructures using a CeO2 template." In: *AIP Advances* 7.5. DOI: 10.1063/1.4973696.

Gariglio, S., M. Gabay, and J.-M. Triscone (2016). "Research Update: Conductivity and beyond at the LaAlO$_3$/SrTiO$_3$ interface." In: *APL Materials* 4.6. DOI: 10.1063/1.4953822.

Gariglio, S. *et al.* (2018). "A spin–orbit playground: surfaces and interfaces of transition metal oxides." In: *Reports on Progress in Physics* 82.1. DOI: 10.1088/1361-6633/aad6ab.

Gastiasoro, M. N., J. Ruhman, and R. M. Fernandes (2020). "Superconductivity in dilute SrTiO$_3$: A review." In: *Annals of Physics* 417. Eliashberg theory at 60: Strong-coupling superconductivity and beyond. DOI: https://doi.org/10.1016/j.aop.2020.168107.

Geller, S. and V. B. Bala (1956). "Crystallographic studies of perovskite-like compounds. II. Rare earth alluminates." In: *Acta Crystallographica* 9.12. DOI: 10.1107/S0365110X56002965.

Goble, N. J. *et al.* (2017). "Anisotropic electrical resistance in mesoscopic LaAlO$_3$/SrTiO$_3$ devices with individual domain walls." In: *Scientific Reports* 7.1. DOI: 10.1038/srep44361.

Golden DRAGON Plus (2015). LW W5AM. Osram Opto Semiconductors GmbH.

Gross, R. and A. Marx (2014). *Festkörperphysik*. Berlin, Boston: De Gruyter Oldenbourg. DOI: https://doi.org/10.1524/9783110358704.

Guduru, V. K. *et al.* (2013). "Optically excited multi-band conduction in LaAlO$_3$/SrTiO$_3$ heterostructures." In: *Applied Physics Letters* 102.5. DOI: 10.1063/1.4790844.

Guguschev, C. *et al.* (2014). "Top-seeded solution growth of SrTiO$_3$ crystals and phase diagram studies in the SrO–TiO$_2$ system." In: *CrystEngComm* 16 (9). DOI: 10.1039/C3CE42037J.

Hayward, S. A. and E. K. H. Salje (1999). "Cubic-tetragonal phase transition in SrTiO$_3$ revisited: Landau theory and transition mechanism." In: *Phase Transitions* 68.3. DOI: 10.1080/01411599908224530.

Herranz, G. *et al.* (2012). "High mobility conduction at (110) and (111) LaAlO$_3$/SrTiO$_3$ interfaces." In: *Scientific Reports* 2.1. DOI: 10.1038/srep00758.

Herranz, G. *et al.* (2015). "Engineering two-dimensional superconductivity and Rashba spin–orbit coupling in LaAlO$_3$/SrTiO$_3$ quantum wells by selective orbital occupancy." In: *Nature Communications* 6.1. DOI: 10.1038/ncomms7028.

Joshua, A. *et al.* (2012). "A universal critical density underlying the physics of electrons at the LaAlO$_3$/SrTiO$_3$ interface." In: *Nature Communications* 3. DOI: 10.1038/ncomms2116.

Kahn, A. H. and A. J. Leyendecker (1964). "Electronic Energy Bands in Strontium Titanate." In: *Phys. Rev.* 135 (5A). DOI: 10.1103/PhysRev.135.A1321.

Kalabukhov, A. *et al.* (2007). "Effect of oxygen vacancies in the SrTiO$_3$ substrate on the electrical properties of the LaAlO$_3$/SrTiO$_3$ interface." In: *Phys. Rev. B* 75 (12). DOI: 10.1103/PhysRevB.75.121404.

Kohler, M. (1938). "Zur magnetischen Widerstandsänderung reiner Metalle." In: *Annalen der Physik* 424.1-2. DOI: https://doi.org/10.1002/andp.19384240124.

Koster, G. *et al.* (1998). "Quasi-ideal strontium titanate crystal surfaces through formation of strontium hydroxide." In: *Applied Physics Letters* 73.20. DOI: 10.1063/1.122630.

Kosterlitz, J. M. and D. J. Thouless (1973). "Ordering, metastability and phase transitions in two-dimensional systems." In: *Journal of Physics C: Solid State Physics* 6.7. DOI: 10.1088/0022-3719/6/7/010.

Kozuka, Y. *et al.* (2009). "Two-dimensional normal-state quantum oscillations in a superconducting heterostructure." In: *Nature* 462.7272. DOI: 10.1038/nature08566.

Kulik, I. O. and A. N. Omel'yanchuk (1975). "Contribution to the microscopic theory of the Josephson effect in superconducting bridges." In: *ZhETF Pis. Red* 21.4. "Contribution to the microscopic theory of the Josephson effect in superconducting bridges." In: *JETP Lett.* 21.4.

Kulik, I. O. and A. N. Omel'yanchuk (1977). "Properties of superconducting microbridges in the pure limit." In: *Fiz. Nizk. Temp.* 3. "Properties of superconducting microbridges in the pure limit." In: *Sov. J. Low Temp. Phys.* 3.7.

Likharev, K. K. (1979). "Superconducting weak links." In: *Review of Modern Physics* 51.1. DOI: 10.1103/RevModPhys.51.101.

Lim, S. G. *et al.* (2002). "Dielectric functions and optical bandgaps of high-K dielectrics for metal-oxide-semiconductor field-effect transistors by far ultraviolet spectroscopic ellipsometry." In: *Journal of Applied Physics* 91.7. DOI: 10.1063/1.1456246.

Lin, X. *et al.* (2013). "Fermi Surface of the Most Dilute Superconductor." In: *Phys. Rev. X* 3 (2). DOI: 10.1103/PhysRevX.3.021002.

Loebich, O. (1972). "The optical properties of gold." In: *Gold Bulletin* 5.1. DOI: 10.1007/BF03215148.

Menzel, S. *et al.* (2011). "Origin of the Ultra-nonlinear Switching Kinetics in Oxide-Based Resistive Switches." In: *Advanced Functional Materials* 21.23. DOI: 10.1002/adfm.201101117.

Monteiro, A. M. R. V. L. *et al.* (2017). "Two-dimensional superconductivity at the (111) LaAlO$_3$/SrTiO$_3$ interface." In: *Phys. Rev. B* 96 (2). DOI: 10.1103/PhysRevB.96.020504.

Müller, K. A. and H. Burkard (1979). "SrTiO$_3$: An intrinsic quantum paraelectric below 4 K." In: *Phys. Rev. B* 19 (7). DOI: 10.1103/PhysRevB.19.3593.

Ohtomo, A. and H. Y. Hwang (2004). "A high-mobility electron gas at the LaAlO$_3$/SrTiO$_3$ heterointerface." In: *Nature* 427.6973. DOI: 10.1038/nature02308.

Parish, M. M. and P. B. Littlewood (2003). "Non-saturating magnetoresistance in heavily disordered semiconductors." In: *Nature* 426.6963. DOI: 10.1038/nature02073.

Piskunov, S. *et al.* (2004). "Bulk properties and electronic structure of SrTiO$_3$, BaTiO$_3$, PbTiO$_3$ perovskites: an ab initio HF/DFT study." In: *Computational Materials Science* 29.2. DOI: https://doi.org/10.1016/j.commatsci.2003.08.036.

Qiao, L. *et al.* (2011). "Cation mixing, band offsets and electric fields at LaAlO$_3$/SrTiO$_3$ (001) heterojunctions with variable La:Al atom ratio." In: *Surface Science* 605.15. DOI: https://doi.org/10.1016/j.susc.2011.04.035.

Reinle-Schmitt, M. L. *et al.* (2012). "Tunable conductivity threshold at polar oxide interfaces." In: *Nature Communications* 3.1. DOI: 10.1038/ncomms1936.

Reyren, N. *et al.* (2007). "Superconducting Interfaces Between Insulating Oxides." In: *Science* 317.5842. DOI: 10.1126/science.1146006.

Reyren, N. *et al.* (2009). "Anisotropy of the superconducting transport properties of the LaAlO$_3$/SrTiO$_3$ interface." In: *Applied Physics Letters* 94.11. DOI: 10.1063/1.3100777.

Salluzzo, M. (2015). *Electronic Reconstruction at the Interface Between Band Insulating Oxides: The LaAlO$_3$/SrTiO$_3$ System.* Ed. by P. Mele *et al.* Cham: Springer International Publishing. Chap. 10. DOI: 10.1007/978-3-319-14478-8_10.

Schäfer, R. (1993). "Quantendiffusionskorrekturen zum Leitwert einer ballistischen Verengung in einer mesoskopischen Goldstruktur." PhD thesis. Universität Köln.

Schooley, J. F., W. R. Hosler, and M. L. Cohen (1964). "Superconductivity in Semiconducting SrTiO$_3$." In: *Phys. Rev. Lett.* 12 (17). DOI: 10.1103/PhysRevLett.12.474.

Seo, S. S. A. *et al.* (2007). "Optical Study of the Free-Carrier Response of LaTiO$_3$/SrTiO$_3$ Superlattices." In: *Phys. Rev. Lett.* 99 (26). DOI: 10.1103/PhysRevLett.99.266801.

Stengel, M. (2011). "First-Principles Modeling of Electrostatically Doped Perovskite Systems." In: *Phys. Rev. Lett.* 106 (13). DOI: 10.1103/PhysRevLett.106.136803.

Strocov, V. N. *et al.* (2019). "Electronic phase separation at LaAlO$_3$/SrTiO$_3$ interfaces tunable by oxygen deficiency." In: *Phys. Rev. Materials* 3 (10). DOI: 10.1103/PhysRevMaterials.3.106001.

Sulpizio, J. A. *et al.* (2014). "Nanoscale Phenomena in Oxide Heterostructures." In: *Annual Review of Materials Research* 44.1. DOI: 10.1146/annurev-matsci-070813-113437.

Szot, K. *et al.* (2002). "Localized Metallic Conductivity and Self-Healing during Thermal Reduction of SrTiO$_3$." In: *Phys. Rev. Lett.* 88 (7). DOI: 10.1103/PhysRevLett.88.075508.

Tarun, M. C., F. A. Selim, and M. D. McCluskey (2013). "Persistent Photoconductivity in Strontium Titanate." In: *Phys. Rev. Lett.* 111 (18). DOI: 10.1103/PhysRevLett.111.187403.

The News Staff (2007). "The Runners-Up." In: *Science* 318.5858. DOI: 10.1126/science.318.5858.1844a.

Tinkham, M. (2004). *Introduction to Superconductivity: Second Edition.* Dover Books on Physics. Dover Publications.

Trier, F. *et al.* (2017). "Universality of electron mobility in LaAlO$_3$/SrTiO$_3$ and bulk SrTiO$_3$." In: *Applied Physics Letters* 111.9. DOI: 10.1063/1.5001316.

Walker, S. M. *et al.* (2015). "Carrier-Density Control of the SrTiO$_3$ (001) Surface 2D Electron Gas studied by ARPES." In: *Advanced Materials* 27.26. DOI: 10.1002/adma.201501556.

Wang, Q.-Y. *et al.* (2012). "Interface-Induced High-Temperature Superconductivity in Single Unit-Cell FeSe Films on SrTiO$_3$." In: *Chinese Physics Letters* 29.3. DOI: 10.1088/0256-307x/29/3/037402.

Weakliem, H.A., W. J. Burke, and V. Korsun (1975). "Optical Properties of SrTiO$_3$ and LiNbO$_3$." In: *R.C.A. Review* 36.

Wolff, K. (2018). "Anisotropic electronic transport of the two-dimensional electron system in Al$_2$O$_3$/SrTiO$_3$ heterostructures." PhD thesis. Karlsruher Institut für Technologie (KIT): Karlsruhe Institut of Technology, Institute of Solid State Physics.

Wolff, K. *et al.* (2020). "Influence of the vicinal substrate miscut on the anisotropic two-dimensional electronic transport in Al$_2$O$_3$–SrTiO$_3$ heterostructures." In: *Journal of Applied Physics* 128.8. DOI: 10.1063/5.0010328.

Woltmann, C. *et al.* (2015). "Field-Effect Transistors with Submicrometer Gate Lengths Fabricated from LaAlO$_3$−SrTiO$_3$-Based Heterostructures." In: *Phys. Rev. Applied* 4 (6). DOI: `10.1103/PhysRevApplied.4.064003`.

Yazdi-Rizi, M. *et al.* (2016). "Infrared ellipsometry study of the confined electrons in a high-mobility γ-Al$_2$O$_3$/SrTiO$_3$ heterostructure." In: *EPL (Europhysics Letters)* 113.4. DOI: `10.1209/0295-5075/113/47005`.

Yazdi-Rizi, M. *et al.* (2017). "Infrared ellipsometry study of photogenerated charge carriers at the (001) and (110) surfaces of SrTiO$_3$ crystals and at the interface of the corresponding LaAlO$_3$/SrTiO$_3$ heterostructures." In: *Phys. Rev. B* 95 (19). DOI: `10.1103/PhysRevB.95.195107`.

Zhong, Z., A. Tóth, and K. Held (2013). "Theory of spin-orbit coupling at LaAlO$_3$/SrTiO$_3$ interfaces and SrTiO$_3$ surfaces." In: *Phys. Rev. B* 87 (16). DOI: `10.1103/PhysRevB.87.161102`.

Ziman, J. M. (1972). *Principles of the Theory of Solids*. 2nd ed. Cambridge University Press. DOI: `10.1017/CBO9781139644075`.

Zubko, P. *et al.* (2011). "Interface Physics in Complex Oxide Heterostructures." In: *Annual Review of Condensed Matter Physics* 2.1. DOI: `10.1146/annurev-conmatphys-062910-140445`.